Towards Rational Design of Ionic Liquid/Metal-Organic Framework Composites: Effects of Interionic Interactions in Ionic Liquids

by

Vahid Nozari

A Thesis Submitted to the

Graduate School of Engineering

in Partial Fulfillment of the Requirements

for the Degree of

Master of Science

In

Chemical and Biological Engineering

Koç University

June 2018

Koç University

Graduate School of Sciences and Engineering

This is to certify that I have examined this copy of a master's thesis by

Vahid Nozari

and have found that it is complete and satisfactory in all respects,

and that any and all revisions required by the final

examining committee have been made.

Committee Members:

Assoc. Prof. Alper Uzun (Advisor, Koç University)

Assoc. Prof. Seda Keskin Avcı (Advisor, Koç University)

Prof. Can Erkey (Koç University)

Assist. Prof. Sarp Kaya (Koç University)

Prof. Ramazan Yıldırım (Boğaziçi University)

Date: 13.06.2018

ABSTRACT

Metal-organic frameworks (MOFs) are nanoporous materials, consist of organic linkers and inorganic metal constituents. Because of their structural functionalities, they have been investigated for a variety of applications such as gas storage and separation, catalysis, and sensing. To introduce further functionality into MOF structure and modify the framework for a target application, ionic liquids (ILs) have been used as a simple post-synthetic modification agent. Since the ILs are composed of ion pairs, by changing either the structures of cations or anions, one can synthesize an almost infinite number of varieties with different physicochemical properties. The challenging part in the modification of MOFs with IL incorporation is the proper choice of an IL. In this thesis study, the effects of interionic interaction energy in ILs on gas storage and separation performance and the thermal stability limits of the composites were investigated by introducing two different systematic changes on the IL structure: changing the anion structure and methylation of the proton on the C2 position of the imidazolium ring.

In the first part, three different preparation techniques were examined to synthesize an IL/MOF composite. Influence of different preparation routes on the adsorption performance of the composite as well as its structural properties was investigated. Wet impregnation technique was selected as a proper way of preparing IL/MOF composites compared to ship-in-a-bottle and incipient wetness methods. Since this technique is not time and energy consuming, it can be employed to synthesize any combination of IL/MOF composite materials. In the second part, a family of imidazolium-based ILs with the same cation, 1-butyl-3-methylimidazolium [BMIM], and seven different anions was selected and incorporated into a well-known MOF, CuBTC (HKUST-1). Effects of interionic interactions in ILs on the extent of interactions between IL and MOF were investigated. The results showed that ILs mostly interact with the open metal sites of CuBTC, and extent of these interactions depends strongly on the IL structure. Consequences of these interactions on the thermal stability limits and adsorption performance of the IL/MOF composites were examined. Results exhibited that interionic interaction in ILs which can be probed spectroscopically with C2–H vibration frequency is the dominant factor in determining the extent of interactions between IL/MOF. In the last part of the thesis, the influence of methylation on the C2 position of

an imidazolium type IL ([BMIM][PF_6]) was investigated. Results showed that methylation in ILs affects the interactions between IL and MOF and results in improvements in gas separation performance. Results provided in this thesis study can help to systematically design IL/MOF pairs by selecting a proper IL depending on the desired application.

ÖZET

Metal organik kafesli yapılar (MOF) organik bağlayıcı ve inorganik metal bileşenlerden oluşan nanogözenekli yapılardır. Bu malzemeler yapısal işlevsellikleri sebebiyle gaz depolama ve ayırma, kataliz, ve sensör uygulamaları gibi çeşitli uygulamalar için araştırılmaktadır. MOF yapısına daha fazla işlevsellik katmak ve kafesli yapıyı hedef bir uygulama için düzenlemek amacıyla MOF yapısına iyonik sıvı katılması sentez-sonrası uygulanabilecek basit modifikasyon yöntemlerinden biridir. İyonik sıvılar farklı iyon çiftlerinden oluşurlar ve bu yüzden katyon ve anyonları değiştirilerek sonsuz sayıda ve fizikokimyasal özellikte iyonik sıvı elde edilebilir. MOF yapısına iyonik sıvı katılması ile ilgili olarak en zorlayıcı kısım kullanılacak iyonik sıvının doğru belirlenmesidir. Bu tez çalışmasında iyonik sıvılardaki iyonlar arası etkileşim enerjisinin kompozit malzemenin gaz depolama ve gaz ayırma performansına ve sıcaklığa karşı dayanıklılık limitine etkisi iyonik sıvı yapısına şu iki farklı sistematik değişim uygulanarak incelenmiştir: anyon yapısının değiştirilmesi ve imidazolyum halkasının C2 pozisyonundaki protonun metillenmesi.

Bu tezin ilk bölümünde, iyonik sıvı/MOF kompozitlerinin sentezlenmesinde kullanılacak yöntemin belirlenmesi için üç farklı hazırlama yöntemi denenmiştir. Farklı hazırlama yöntemlerinin kompozit malzemenin gaz tutma ve yapısal özelliklerine etkisi incelenmiş ve "ıslak emdirme" (wet impregnation) tekniğinin "şişede gemi" (ship in a bottle) ve "insipient ıslatma" (incipient wetness) tekniklerine kıyasla daha uygun bir yöntem olduğuna karar verilmiştir. Bu teknik, zaman ve enerji tüketimi açısından daha verimli bir teknik olduğundan dolayı herhangi bir iyonik sıvı/MOF kompozit malzemesinin hazırlanması için uygulanabilir. İkinci bölümde, imidazolyumlu iyonik sıvıları içeren, aynı katyon ve 7 farklı anyondan oluşan bir iyonik sıvı grubu seçilmiş ve bu iyonik sıvılar ayrı ayrı CuBTC (HKUST-1) MOF'una yüklenmiştir. Bu sayede iyonik sıvılardaki iyonlar arası etkileşimin iyonik sıvı ile MOF arasındaki etkileşime nasıl katkı sağladığı incelenmiştir. Elde edilen sonuçlar CuBTC içine yüklenen iyonik sıvının çoğunlukla CuBTC'deki açık metal merkezleriyle etkileşim içinde olduğunu ve bu etkileşimlerin büyüklüğünün kuvvetli olarak iyonik sıvı yapısına bağlı olduğunu göstermiştir. Bu etkileşimin iyonik sıvı/MOF kompozitinin sıcaklığa karşı dayanıklılık limitine ve gaz tutma performansına etkisi incelenmiştir. İyonlar arası etkileşim

spektroskopik yöntemlerle C2-H titreşim frekansındaki değişimden yararlanılarak incelenmiştir ve bu C2-H titreşim frekansının iyonik sıvı/MOF etkileşiminde dominant bir rol oynadığı görülmüştür. Bu tezin son bölümünde, imidazolyum tipi bir iyonik sıvı olan [BMIM][PF_6]'nın C2 pozisyonundaki metillenmenin etkisi incelenmiştir. Sonuçlar iyonik sıvıdaki metillenmenin iyonik sıvı ve MOF arasındaki etkileşimi değiştirerek iyonik sıvı/MOF kompozitinin gaz tutma performansını etkilediğini göstermiştir. Bu tez ile sağlanan sonuçlar iyonik sıvı/MOF çiftlerinin sistematik olarak tasarlanmasına ve istenen uygulama alanına göre uygun bir iyonik sıvı seçilmesine katkı sağlayacaktır.

ACKNOWLEDGEMENTS

Foremost, I would like to greatly thank my advisors Prof. Alper Uzun and Prof. Seda Keskin-Avcı for giving me the chance to work with them, their endless support and precious time they spent during my master study. I have gained valuable information and experience from them and I would like to appreciate their help to solve every problem I faced during my master program. Special thanks to Prof. Can Erkey, Prof. Sarp Kaya and Prof. Ramazan Yıldırım for being my thesis committee members.

Many thanks to Koç University for providing me a scholarship and financial support throughout my master study and Scientific and Technological Research Council of Turkey (Tubitak) 1001 Program (project number: 114R093) for providing the funding.

I appreciate Koç University Surface Science and Technology Center (KUYTAM) especially Dr. Bariş Yağcı, Dr. Amir Motallebzadeh, Dr. Ceren Yılmaz Akkaya, and Dr. Gulsu Şimşek for their assistance in characterization measurements.

Being as a member of NEMO group and Uzun Lab was a great chance for me. I am so happy that I could make very nice friendships. I would like to thank Çiğdem Altıntaş, Muhammed Zeeshan, Ahsan Jalal, Melike Babucci, Ozge Akarçay, Pelin Kınık, Zeynep Sumer, Burak Koyuturk, and Ilknur Erucar for their kind help and creating a nice environment in the office and in the lab.

I must express my profound gratitude to my parents (Ana janim and Ata janim) for their guidance and help in every step of my life. Without their motivation, I was not able to withstand the difficulties of living abroad. I would like to deeply thank my very nice and cool brother Hadi (paşam). I owe him a lot. He is my best brother and at the same time my best friend. He is a person who I can always count on him in every situation. He taught me how to be strong and withstand in case of any problems. Special thanks to Darya (darya bakal), who always cares and spends time with me. I am really happy to have such a nice and colorful sister.

Finally, I would like to thank my excellent wife Ayda (aydam). I am very blessed to have such a respectful, very kind and cool wife who always sacrifices her for me. I appreciate her positive energy and a great sense of support. She has been always trying to encourage and motivate me to progress and move forward. She has done a lot for me and I wish her life to be full of happiness, success and lovely moments.

TABLE OF CONTENTS

ABSTRACT iii
ÖZET v
ACKNOWLEDGEMENTS vii
LIST OF TABLES x
LIST OF FIGURES x
NOMENCLATURE xiv
Chapter 1 Introduction 1
Chapter 2 Literature Review 4
2.1. Application of IL/MOF Composites in Adsorption-Based Gas Separation 4
2.2. Different Applications of IL/MOF Composites 6
Chapter 3: Methods 10
3.1. Materials and Sample Preparation 10
3.1.1. Materials 10
3.1.2. Synthesis of [BMIM][Br] 10
3.1.3. Wet impregnation synthesis (WIM) 11
3.1.4. Incipient wetness synthesis (INW) 11
3.1.5. Ship-in-bottle synthesis (SIB) 11
3.2. Characterization 12
3.2.1. X-ray Diffraction (XRD) 12
3.2.2. Fourier Transform Infrared (FTIR) Spectroscopy 12
3.2.3. X-ray Fluorescence (XRF) 12
3.2.4. Brunauer-Emmet-Teller (BET) 13
3.2.5. Scanning Electron Microscopy (SEM) 13
3.2.6. Thermogravimetric Analysis (TGA) 13
3.2.7. Gas adsorption Measurements 14
Chapter 4: Influence of Different Synthesis Techniques on Structure, Thermal Stability, and Gas Separation Performance of IL/MOF Composites 16
4.1. Preparation of [BMIM][Br]/CuBTC Composites 16
4.2. Characterization of Composite Samples 16
4.2.1. Powder X-Ray Diffraction 16
4.2.2. Scanning Electron Microscopy (SEM) of CuBTC and Composites 18

4.2.3. FTIR Spectroscopy Results of CuBTC and Composite samples 19
4.2.4. BET Surface Area and Pore Volume Analysis of CuBTC and Composite Samples 22
4.2.5. Thermogravimetric Analysis of CuBTC and Composite Samples 23
4.3. Gas Adsorption and Gas Separation Performance of CuBTC and Composite samples 26
Chapter 5: Toward Rational Design of Ionic Liquid/Metal-Organic Framework Composites: Effects of Interionic Interaction Energy 28
5.1. Preparation of Imidazolium-Based IL/MOF Composites 29
5.2. Characterization of Imidazolium-Based IL/MOF Composites 29
5.2.1. Brunauer-Emmett-Teller (BET) Surface Area and Pore Volume Analysis 30
5.2.2. Powder X-Ray Diffraction (XRD) and Scanning Electron Microscopy Results of Imidazolium-Based IL/MOF Composites 30
5.2.3. Fourier Transform Infrared Spectroscopy (FTIR) Analysis 30
5.3. Results and Discussion 31
Chapter 6: Towards Rational Design of Ionic Liquid/Metal Organic Framework Composites: Effect of Methylation in Ionic Liquid 38
6.1. Preparation of [BMIM][PF_6]/CuBTC and [BMMIM][PF_6]/CuBTC Composites 38
6.2. Characterization of Composite Samples 38
6.2.1. X-ray Fluorescence (XRF) of composite samples 38
6.2.2. BET Surface Area and Pore Volume Analysis of CuBTC and Composite Samples 39
6.2.3. X-ray Diffraction (XRD) patterns of CuBTC and composite samples 39
6.2.4. Scanning Electron Microscopy (SEM) of CuBTC and IL/CuBTC Composites 41
6.2.5. Confirmation of Internally Incorporated IL Molecules 42
6.2.5. FTIR Spectroscopy Results of CuBTC, Bulk ILs and Composite samples 42
6.2.6. Thermogravimetric Analysis of CuBTC and Composite Samples 44
6.3. Gas Adsorption and Gas Separation Performance of [BMIM][PF_6]/CuBTC and [BMMIM][PF_6]/CuBTC samples 46
Chapter 7: Conclusions and Outlook 53
BIBLIOGRAPHY 55
APPENDIX A: Supporting Information on Characterization of Chapter 5 62
APPENDIX B: Full Names of Ionic Liquids 77
APPENDIX C: Cosmo-RS solubility results for [BMIM][PF_6] and [BMMIM][PF_6] 78

LIST OF TABLES

Table 4.1. Band shifts in [BMIM][Br] features compared to composite samples. 21
Table 4.2. BET surface area and Pore volumes of CuBTC and [BMIM][Br]/CuBTC samples. 222
Table 4.3. Onset, T_{onset}, and derivative onset, T'_{onset} of CuBTC, [BMIM][Br] and [BMIM][Br]/CuBTC samples. 25
Table 6.1. BET surface area and pore volumes of CuBTC, [BMIM][PF_6]/CuBTC and [BMMIM][PF_6]/CuBTC samples. 39
Table 6.2. *T'onset* values of CuBTC, bulk ILs and IL incorporated CuBTC samples. ..46
Table A.1. BET surface areas, pore volumes, and corresponding IL loading in each sample (calculated from XRF measurements). 75
Table A.2. C2–H vibration frequency of bulk ILs and corresponding (Cu–O) red shifts for each IL/MOF sample. (shift values are obtained from Fityk software).[59] 76
Table B.1. Abbreviations and full names of ionic liquids referred in this thesis. 77

LIST OF FIGURES

Figure 4.1. X-ray diffraction patterns of CuBTC, [BMIM][Br]/CuBTC samples 17
Figure 4.2. SEM images of (a) CuBTC; (b) [BMIM][Br]/CuBTC-SIB; (c) [BMIM][Br]/CuBTC-INW; (d) [BMIM][Br]/CuBTC-WIM. 18
Figure 4.3. FTIR spectra of bulk [BMIM][Br], CuBTC and [BMIM][Br]/CuBTC samples; (a) 1800 and 400 and (b) 3300 and 2800 cm^{-1}. 20
Figure 4.4. Thermal stability of CuBTC, [BMIM][Br], and [BMIM][Br]/CuBTC samples: (a) TG curves and (b) DTG curves. 24
Figure 4.5. Adsorption isotherms for CuBTC, [BMIM][Br]/CuBTC-WIM, [BMIM][Br]/CuBTC-SIB, and [BMIM][Br]/CuBTC-INW; (a) CO_2 isotherms; (b) CH_4 isotherms, and (c) CO_2/CH_4 ideal selectivity at 298 K. 26
Figure 5.1. Correlation between ν(C2H) of bulk ILs and Cu–O red shifts in IL/MOF samples. 33

Figure 5.2. Correlation between T'_{onset} of IL/MOF composites (left y-axis) and ν(C2H) of bulk ILs. The vertical axis on the right shows the correlation between the corresponding red shift in ν(Cu–O) and ν(C2H) of bulk ILs. 34
Figure 5.3. Correlation between CH_4 and CO_2 uptakes versus ν(C2H) of bulk ILs: (a) CO_2 uptake at 1 bar; (b) CH_4 uptake at 1 bar; (c) Correlation coefficients for CO_2 uptake and CH_4 uptake at different pressures (a line was added between the points to guide the eye); (d) Slope for correlations between ν(C2H) and gas uptakes. 36
Figure 6.1. XRD patterns of CuBTC, [BMIM][PF_6]/CuBTC and [BMMIM][PF_6]/CuBTC samples. 40
Figure 6.2. SEM images of (a) CuBTC; (b) [BMIM][PF_6]/CuBTC and (c) [BMMIM][PF_6]/CuBTC. 41
Figure 6.3. FTIR spectra of bulk [BMIM][PF_6], CuBTC, [BMIM][PF_6]/CuBTC and [BMIM][PF_6]/CuBTC samples; (a) 1800 and 400 ;(b) 3300 and 2800 cm^{-1}. 43
Figure 6.4. TGA results of CuBTC, [BMIM][PF_6], [BMMIM][PF_6], [BMIM][PF_6]/CuBTC and [BMMIM][PF_6]/CuBTC samples: (a) TG curves and (b) derivative TG curves. 45
Figure 6.5. Isotherms for CuBTC, [BMIM][PF_6]/CuBTC and [BMMIM][PF_6]/CuBTC samples at 298 K; (a) CO_2, (b) CH_4 and (c) N_2. 47
Figure 6.6. Ideal adsorption selectivities of CuBTC, [BMIM][PF_6]/CuBTC and [BMMIM][PF_6]/CuBTC at room temperature up to 1 bar; (a) CO_2/N_2 and (b) CH_4/N_2. 49
Figure 6.7. IAST mixture selectivity of CuBTC, [BMIM][PF_6]/CuBTC and [BMMIM][PF_6]/CuBTC samples for (a) CO_2/N_2 (15:85 mixture) and (b) CH_4/N_2 (50:50 mixture). 51
Figure A.1. XRD patterns of CuBTC and IL/CuBTC samples. 63
Figure A.2. SEM images: (a) CuBTC (b) [BMIM][$MeSO_3$]/CuBTC; (c) [BMIM][$MeSO_4$]/CuBTC; (d) [BMIM][CF_3SO_3]/CuBTC; (e) [BMIM][NTf_2]/CuBTC; (f) [BMIM][$OcSO_4$]/CuBTC; (g) [BMIM][SbF_6]/CuBTC; (h) [BMIM][SCN]/CuBTC. 63
Figure A.3. FTIR spectra of [BMIM][SCN], CuBTC and [BMIM][SCN]/CuBTC in the region of (a) 400-1800 cm^{-1} and (b) 2800-3300 cm^{-1}. 64

Figure A.4. FTIR spectra of [BMIM][SbF_6], CuBTC and [BMIM][SbF_6]/CuBTC in the region of (a) 400-1800 cm^{-1} and (b) 2800-3300 cm^{-1}. 65
Figure A.5. FTIR spectra of [BMIM][$OcSO_4$], CuBTC and [BMIM][$OcSO_4$]/CuBTC in the region of (a) 400-1800 cm^{-1} and (b) 2800-3300 cm^{-1} 66
Figure A.6. FTIR spectra of [BMIM][NTf_2], CuBTC and [BMIM][NTf_2]/CuBTC in the region of (a) 400-1800 cm^{-1} and (b) 2800-3300 cm^{-1}. 67
Figure A.7. FTIR spectra of [BMIM][$MeSO_4$], CuBTC and [BMIM][$MeSO_4$]/CuBTC in the region of (a) 400-1800 cm^{-1} and (b) 2800-3300 cm^{-1}. 68
Figure A.8. FTIR spectra of [BMIM][$MeSO_3$], CuBTC and [BMIM][$MeSO_3$]/CuBTC in the region of (a) 400-1800 cm^{-1} and (b) 2800-3300 cm^{-1}. 69
Figure A.9. FTIR spectra of [BMIM][CF_3SO_3], CuBTC and [BMIM][CF_3SO_3]/CuBTC in the region of (a) 400-1800 cm^{-1} and (b) 2800-3300 cm^{-1}. 70
Figure A.10. TGA results of CuBTC and [BMIM][SCN]/CuBTC. Black curve: CuBTC and red curve: [BMIM][SCN]/CuBTC. 71
Figure A.11. TGA results of CuBTC and [BMIM][SbF_6]/CuBTC. Black curve: CuBTC and red curve: [BMIM][SbF_6]/CuBTC. 71
Figure A.12. TGA results of CuBTC and [BMIM][$OcSO_4$]/CuBTC. Black curve: CuBTC and red curve: [BMIM][$OcSO_4$]/CuBTC 72
Figure A.13. TGA results of CuBTC and [BMIM][NTf_2]/CuBTC. Black curve: CuBTC and red curve: [BMIM][NTf_2]/CuBTC. 72
Figure A.14. TGA results of CuBTC and [BMIM][$MeSO_4$]/CuBTC. Black curve: CuBTC and red curve: [BMIM][$MeSO_4$]/CuBTC. 73
Figure A.15. TGA results of CuBTC and [BMIM][$MeSO_3$]/CuBTC. Black curve: CuBTC and red curve: [BMIM][$MeSO_3$]/CuBTC. 73
Figure A.16. TGA results of CuBTC and [BMIM][CF_3SO_3]/CuBTC. Black curve: CuBTC and red curve: [BMIM][CF_3SO_3]/CuBTC.,..... 74
Figure C.1 Cosmo-RS solubility results for [BMIM][PF_6] and [BMMIM][PF_6] at 298 K; (a) N_2, (b) CO_2 and (c) CH_4. 78
Figure C.2. Solubility selectivities for [BMIM][PF_6] and [BMMIM][PF_6] at 298 K; (a) CO_2/N_2 and (b) CH_4/N_2..... 79
Figure C.3. FTIR spectra of CuBTC, bulk [BMIM][PF_6], and [BMIM][PF_6]/CuBTC prior and after washing with toluene in two different regions, 400-1600 cm^{-1} and 1800-3200

cm^{-1}; (a) and (b) Powder samples before and after washing with toluene; (c) and (d) The filtrate (liquid samples)……...….80
Figure C.4. FTIR spectra of CuBTC, bulk [BMIM][PF_6], and [BMIM][PF_6]/CuBTC prior and after washing with toluene in two different regions, 400-1600 cm^{-1} and 1800-3200 cm^{-1}; (a) and (b) Powder samples before and after washing with toluene; (c) and (d) The filtrate (liquid samples)……... 81

NOMENCLATURE

BET: Brunauer–Emmett–Teller

IL: Ionic liquid

MOF: Metal-organic framework

N_i: Adsorbed amount for component i

Q_{st}: Isosteric heat of adsorption (kJ/mol)

SEM: Scanning electron microscope

STP: Standard temperature and pressure

TGA: Thermal gravimetric analysis

XRF: X-Ray Fluorescence

DFT: Density Functional Theory

S_{BET}: BET surface area

CNT: Carbon nanotube

T_{onset}: Onset temperature (°C)

T'_{onset}: Derivative onset temperature (°C)

V_p : Pore volume (cm^3/g)

XRD: X-Ray Diffraction

ZIF: Zeolitic imidazolate framework

Chapter 1 Introduction

Natural gas, mostly composed of methane (87-96 mol.%) is one of the cleaner energy resources compared to the fossil fuels.[1] It has a certain level of impurities such as CO_2 (0.1-1.0 mol.%) and N_2 (0.7-5.6 mol.%) which decrease energy density and also causes corrosion in the pipelines. Besides, CO_2 is a greenhouse gas and plays a major role in global warming and it is believed to be one of the threats for human health.[2] Therefore, it must be separated and stored in an efficient and reasonable way.

Compared to other methods such as membrane-based gas separation and cryogenic distillation, adsorption-based gas separation is one of the possible and feasible ways of capturing and separating CO_2. In adsorption-based gas separation, the most important parameter is the adsorbent material which is mostly a porous media in which gas molecules are being stored and separated from other molecules.[3] Various types of adsorbents such as activated carbons, zeolites, carbon nanotubes, silica gels, and metal-organic frameworks (MOFs) have been studied extensively for the storage and separation of CO_2.[4–7] Among these adsorbents, MOFs have been recently considered as promising materials because of their tunable properties.[8,9]

MOFs are porous materials composed of metal complexes connected by organic linkers. Variability in metal nodes (inorganic constituent) and the organic linkers provides topological diversity. These crystalline materials have very large surface areas (up to 6000 m^2/g) and high porosities (up to 90% void space) which make them as interesting candidates for storage and separation applications.[10] Combination of different organic linkers with various metal nodes results in materials having different pore sizes and shapes. Besides their application in gas storage and gas separation, they have been investigated in wide variety of applications such as catalysis,[11] drug storage and delivery,[12] conductivity,[13] and sensing.[14]

Structure of MOFs can be modified by introducing some functional reagents during or post-synthesis. As a post-synthetic modification route, it is possible to introduce extra adsorption sites or incorporated some chemical reagents which can be bind to ligands and increase the affinity of structure towards a specific gas in adsorption-based gas separation.[15–17] One of the recent techniques to modify the MOF structure and improve the gas adsorption and separation performance of MOFs is incorporating ionic liquids (ILs).[18–20]

ILs are composed of cations and anions, which are mostly in liquid phase at room temperature. They are thermally stable, non-volatile, and non-flammable making them promising solvents compared to conventional ones. Similar to MOFs, their structure can be tuned by changing the cations or anions. There are almost 10^{18} potential possible combination of ions which provide wide range of physicochemical properties and functionalities.[21–23] ILs have been used in wide range of applications such as liquid-liquid extraction,[24] solvents,[22] catalysis,[25] and gas absorption.[26]

In this thesis, interactions between ILs and MOFs have been elucidated and consequences of these interactions on the thermal stability and adsorption performance (CO_2 and CH_4) of IL/MOF composites were investigated. CuBTC (HKUST-1) was selected as a MOF, since it has been studied widely in the literature and it has open metal sites that are favorable sites for guest molecules.[27–29] the ILs considered were selected from a family of ILs with the same cation, 1-*n*-butyl-3-methylimidazolium, $[BMIM]^+$ with different anions: bis(trifluoromethylsulfonyl)imide, $[NTf_2]^-$, methylsulfate, $[MeSO_4]^-$, hexafluoroantimonate, $[SbF_6]^-$, thiocyanate, $[SCN]^-$, trifluoromethanesulphonate, $[CF_3SO_3]^-$, methanesulfonate, $[MeSO_3]^-$, and octylsulfate, $[OcSO_4]^-$.[30] When the anion of an IL changes, the interactions between ions (interionic interaction) will be modified. Accordingly, effects of interionic interaction strength in ILs on IL-MOF interactions were probed using spectroscopy. Moreover, effect of methylation in ILs which disturbs the directional hydrogen bonding in ILs and modifies the interactions between ions on the interactions between IL and CuBTC was examined. 1-*n*-butyl-2,3-dimetylimidazolium hexafluorophosphate, [BMMIM][PF_6], which is the

methylated form of 1-*n*-butyl-3-metylimidazolium hexafluorophosphate, [BMIM][PF_6] were selected to study the methylation effect.

In Chapter 2, a brief literature review on the utilization of IL/MOF composites in gas storage, gas separation, and different fields are provided. In Chapter 3, sample preparation techniques, characterization details, and gas adsorption performance measurement procedures are summarized. In Chapter 4, the influence of IL/MOF composite preparation routes (wet impregnation, incipient wetness, and ship in a bottle) on the structure and gas adsorption performance of IL/MOF samples were evaluated. Chapter 5 illustrates the effect of interionic interactions in ILs on the thermal stability and adsorption performance of IL/MOF composites. In Chapter 6, the influence of methylation in imidazolium ring of an IL is investigated and the interactions between methylated IL with MOF are presented. At the end this thesis (Chapter 7), outcomes obtained from this thesis study are summarized and opportunities for future directions in this field are discussed.

Chapter 2 Literature Review

In this chapter, application of IL/MOF composites in adsorption-based gas separation is reviewed. Moreover, IL/MOF composites used in different research areas such as membrane-based gas separation, catalysis, and other fields are also discussed.

2.1. Application of IL/MOF Composites in Adsorption-Based Gas Separation

MOFs have been investigated extensively in literature for different gas adsorption and gas separation applications. However, to improve the adsorption and separation performance of a parent MOF, several methods have been applied such as introducing different functional metals or ligands,[31,32] metal substitution[33], and ligand exchange.[34] Another simple technique is the post-synthesis modification of a MOF. One of the post-synthesis modification routes is incorporating ILs into MOF structures.[35] The tunability of both the ILs and MOFs provides a very broad potential for improvements in IL/MOF gas storage and separation performances in composite materials compared to pristine MOFs.[36–38]

da Silva et al.[39] impregnated [BMIM][PF_6] (1-*n*-butyl-3-methylimidazolium hexafluorophosphate) and [BMIM][NTf_2] (1-*n*-butyl-3-methylimidazolium bis(trifluoromethylsulphonyl)imide) into CuBTC (($Cu_3(BTC_2)$, BTC: benzene 1,3,5 tricarboxylate)) with three different loading of 1, 5, and 10 wt% of IL using incipient wetness technique. CO_2 adsorption capacity was investigated using both the experimental and theoretical methods. Monte Carlo simulations showed that the maximum loading of IL was 30 wt%. They obtained enhanced CO_2 uptakes in each concentration up to 2 bar with 30 wt% loaded sample compared to pristine CuBTC.

Ban et al.[40] used [BMIM][Tf_2N] to tune the molecular sieving property of ZIF-8 MOF. They reported enhanced CO_2 uptake in the composite material in the literature.

However, uptake amounts of N_2 and CH_4 in [BMIM][Tf_2N]/ZIF-8 composite was lower compared to pristine ZIF-8. CO_2/N_2 and CO_2/CH_4 selectivities were improved by almost five-times compared to ZIF-8. Higher selectivities were attributed to the good solubility of CO_2 in the IL.

Our research group impregnated [BMIM][BF_4] with different loadings 5, 20, and 30 wt% into CuBTC cavities. CO_2, CH_4, N_2, and H_2 adsorption capacities of [BMIM][BF_4]/CuBTC were all decreased in comparison with CuBTC. Since the pore space available for the gas molecules were occupied by IL molecules. CO_2/CH_4, CO_2/N_2, CO_2/H_2, CH_4/N_2, CH_4/H_2, and N_2/H_2 ideal adsorption selectivities were obtained from the ratio of the adsorbed amount of single gases. Highest improvement was obtained for CH_4/H_2 selectivity at low pressures at 30 wt% IL loading. For instance, at 0.2 bar CO_2/H_2 selectivity increased from 26 to 56 upon IL incorporation with 30 wt%.[18]

Ma et al.[41] impregnated a task-specific ionic liquid (TSIL) ([C_3NH_2BIM][Tf_2N]) in NH_2-MIL-101(Cr). Similar to previous studies, as a result of the reduced pore volume, CO_2 and N_2 uptakes in TSIL/NH_2-MIL-101(Cr) composite were decreased. Presence of $[Tf_2N]^-$ anion and amine groups in [C_3NH_2BIM][Tf_2N] contributed to excellent affinity toward CO_2. On the other hand, N_2 uptake was decreased significantly at lower pressures. As a result, the CO_2/N_2 selectivity of TSIL/MOF composite was enhanced by almost two-times more than that of pristine MOF. They applied this composite material in Mixed-Matrix-Membrane (MMM) as a filler particle.

Recently, our group impregnated [BMIM][BF_4] into ZIF-8 with various IL loadings (4, 20, and 28 wt%). Both experimental and computational single-component gas adsorption isotherms for CH_4, CO_2, and N_2 were measured for all the IL/MOF composites. The results for the composite with 20 wt% IL loading showed enhancement in CO_2 uptake more than 9% compared to pure ZIF-8 at 0.1 bar. Sample with 28 wt% IL loading showed an increase in CO_2/CH_4, CO_2/N_2, and CH_4/N_2 selectivities from 2.2, 6.5, and 3 to 4, 13.3, and 3.4, respectively. The difference in the isosteric heat of adsorption ΔQ_{st} value in low-pressure region was higher for IL-incorporated samples compared to pristine ZIF-8. This was attributed to the stronger interaction of gas molecules with the

composite samples which resulted in enhanced CO_2 selectivities. However, in high-pressure region, the dominant factor became the available pore volume.

Similarly, in a different study, our group incorporated [BMIM][PF_6] into ZIF-8 and results showed a significant level of increase in gas separation performance of the material. Experiments and molecular simulations illustrated that CO_2/CH_4 and CO_2/N_2 selectivities increased from 2.2 and 6.5 to 8.9 and 24, respectively, after IL incorporation in ZIF-8. Detailed characterization of the structures combined with density functional theory (DFT) calculations showed that there are strong interactions sites between the IL molecules and the MOF.[19]

Mohamedali et al.[42] investigated the CO_2 capture by incorporation of an acetate-based ionic liquid ([BMIM][Ac]) using incipient wetness route with three different loading of 10, 20, and 30 wt% into ZIF-8. They reported seven-times higher CO_2 uptake and CO_2/N_2 selectivity at 0.2 bar and 303 K compared to pristine ZIF-8. Using Q_{st} values, they confirmed that improvements in CO_2 storage and selectivity are originating from the chemisorption interaction between CO_2 molecules and the carbonyl group on the IL.

[BMIM][OAc] (1-*n*-butyl-3-methylimidazolium acetate) was supported on a MIL-101 (Cr) MOF to investigate acetylene separation from ethylene. Adsorption isotherms showed that acetylene/ethylene selectivity was increased from 3 to 30 after IL incorporation. To evaluate the industrial application, breakthrough and regeneration experiments were performed. They showed that the material was stable under regeneration experiments and it can be used in real industrial applications.[43]

2.2. Different Applications of IL/MOF Composites

ILs have tunable structures which make these materials very promising in introducing functionalities. Combination of MOFs with ILs provides an infinite number of structures which can be applied in different applications.[35,44,45] Here some studies about different application of IL/MOF hybrid materials are summarized.

Fujie et al.[46] incorporated EMI-TFSA (1-ethyl-3-methylimidazolium bis(trifluoromethylsulfonyl)amide) in ZIF-8 and investigated low-temperature ionic conductor behavior. At low temperatures, the ionic conductivity of bulk EMI-TFSA significantly decreased because of the freezing effect. However, EMI-TFSA@ZIF-8 showed no decrease in the ionic conductivity because of no phase transition. The ionic conductivity of EMI-TFSA@ZIF-8 was higher than that of bulk EMI-TFSA below 250 K.

Recently, the proton conductivity of a MOF was improved by six-order of magnitude by binary IL incorporation. Impregnation of binary ionic liquid, EIMS-HTFSA (EIMS=1-(1-ethyl-3-imidazolium)propane-3-sulfate; HTFSA=N,N-bis(trifluoromethanesulfonyl)amide) into MIL-101 resulted in producing a safe electrolyte for proton conduction above 100 °C. Furthermore, the composite had a better thermal stability among other proton-conducting materials.[47]

Removal of toxic compounds from the liquid phase is one of the challenges which was investigated using IL/MOF composites. Khan et al. investigated the removal of benzothiophene from liquid fuel using [BMIM][Br]@MIL-101 composite as an adsorbent. [BMIM][Br] was incorporated in MIL-101 cages using the ship-in-bottle technique. The composite showed 71% increase in benzothiophene adsorption compared to pristine MOF because of increased acid-base interactions between the IL and benzothiophene. They tested the stability of the composite under several cycles and they reported no loss of stability.[48]

Incorporation of ILs in the pores of MOFs offers a broad potential for the catalysis field. IL incorporation either introduces active sites to the framework or adjusts the electronic environment in the framework for specific reactions to occur.

Tharun et al.[49] synthesized a new catalyst for cycloaddition of propylene oxide and CO_2. They grafted an IL (aminopyridinum iodide) on ZIF-90 and used as a catalyst for solvent-less cycloaddition of CO_2 under mild reaction conditions. Catalytic activity improved dramatically due to distinctive CO_2 capture capacity of ZIF-90 in addition to

the presence of IL. Results confirmed that catalytic activity remained constant after five runs.

Luo et al.[50] immobilized an amino-functionalized basic IL (ABIL-OH) on a microporous MOF (HKUST-1) and obtained a molecular size and shape selective catalyst for Knoevenagel condensation. Characterization of the catalyst revealed that IL molecules were confined in nanocavities of HKUST-1 via Cu-NH_2 coordination bond. The enhanced catalytic activity of the catalyst was the same under repeated cycles showing that the catalyst was stable without any loss in the activity.

1-methyimidazolium-3-propylsulfonate hydrosulfate, [PSMIM][HSO_4] was immobilized on UiO-66 and applied in oxidative desulfurization of fuel oils. The [PSMIM][HSO_4]/UiO-66 showed higher desulfurization compared to UiO-66. The increase in IL loading resulted in an increase in desulfurization performance. This catalyst was reported to be a good candidate for the removal of SO_x in petroleum refining.[51]

In a similar study, Abednatanzi et al.[52] synthesized a DAIL/MOF composite for oxidation of benzyl alcohol. Since the MOF (MIL-100 (Fe)) had open metal sites, amino groups of the IL coordinately bonded to the open metal sites of the MOF. The catalytic activity increased from 38% for pristine MIL-100 (Fe) to 92% upon incorporation of the IL. Moreover, the catalyst was tested up to four times and the stability just decreased slightly from 92 to 86%.

Han et al.[53] confined an acidic IL (DAILs, 1,4-bis[3-(propyl-3-sulfonate) imidazolium] butane hydrogen sulfate) in MIL-100 (Fe) cages. MIL-100(Fe)/DAILs catalyst was used for esterification of oleic acid with methanol. Improved catalytic activity was attributed to the impregnation-reaction-encapsulation mechanism of the IL/MOF composite.

Gupta et al.[54] investigated CO_2 capture in IL membranes supported on MOFs. The was [BMIM][SCN] while they used two hydrophobic and hydrophilic ZIF-71 and Na-*rho*-ZMOF MOFs as supports. In both membranes, they observed that the $[SCN]^-$ anion interacts more strongly than the $[BMIM]^+$ with the MOFs. CO_2 diffusion in the membrane

was slower than N_2 especially in [BMIM][SCN]/ ZMOF since Na^+ sites in Na-*rho*-ZMOF are favorable sites for CO_2 molecules.

Chapter 3: Methods

This chapter describes the sample preparation, synthesis techniques, experimental methodologies and gas adsorption measurements used for materials characterization.

3.1. Materials and Sample Preparation

In this part, three different synthesis methods are explained for preparation of IL/MOF composites which are: wet impregnation, incipient wetness, and ship in bottle techniques.

3.1.1. Materials

CuBTC (Basolite C300), N-methylimidazole, 1-bromobutane, ILs, acetone and ethyl acetate were purchased from Sigma-Aldrich and stored in an argon-filled Labconco glovebox. CH_4 (99.95 vol %), CO_2 (99.9 vol %), and N_2 (99.998 vol%) for gas adsorption measurements were purchased from Linde gas company used in this study. ILs and CuBTC were stored in an Ar-filled glovebox (Labconco).

3.1.2. Synthesis of [BMIM][Br]

1.0269 g of 1-bromobutane and 0.8246 g of N-methylimidazolium were loaded into a round bottom flask connected with a reflux system. The mixture was stirred for 48 h at 70 °C until the formation of two phases. Unreacted top phase was decanted. To further remove the unreacted reagents, 10 mL of ethyl acetate was added to the resulting sample, mixed thoroughly and decanted (this was done three-times). Finally, the sample was

heated to 70 °C under vacuum to evaporate the solvent. Obtained pale yellow [BMIM][Br] was placed in glove-box after synthesis.[55,56]

3.1.3. Wet impregnation synthesis (WIM)

IL/CuBTC-WIM sample was prepared after drying the CuBTC overnight at 105 °C under vacuum. 0.3 g IL was dissolved in 20 mL acetone and stirred for 1 h at room temperature. Afterward, 0.7 g CuBTC was added to the solution and the mixture was mixed for 6 h at 35 °C until whole acetone evaporated. The resulting sample was dried in an oven at 105 °C overnight.[18–20,30]

3.1.4. Incipient wetness synthesis (INW)

0.3 g IL was dissolved in 3 mL methanol at room temperature. The resulting solution was added dropwise to 0.7 g of dried CuBTC. After adding a certain amount of solution to CuBTC, the mixture was mixed thoroughly to evaporate the ethanol. The adding of solution and mixing were repeated till whole the solution was added to the CuBTC. The resulting material was dried at 70 °C overnight to evaporate the remaining methanol from the composite.[39,42]

3.1.5. Ship-in-bottle synthesis (SIB)

We prepared [BMIM][Br]/CuBTC-SIB sample by dissolving 0.11 g N-methylimidazole in 20 mL methanol at 80 °C for 3 h. Subsequently, 0.7 g CuBTC was added and stirred for 24 h. Finally, 1-bromobutane was added to the mixture and mixed for 24 h. The resulting composite was separated from methanol using filtration. The recovered solid was washed with ethyl acetate three-times and was dried in an oven at 105 °C overnight.[38,57,58]

3.2. Characterization

In this section, characterization techniques and methods used for analyzing the structure of the synthesized samples are described.

3.2.1. X-ray Diffraction (XRD)

A Bruker D8 Phaser instrument with an X-ray generator performance of 30 kV of voltage and 10 mA of current was utilized to obtain the diffraction pattern of CuBTC and IL/CuBTC composites. A Cu Kα1 was used as radiation source with a wavelength of 1.5418 Å and a Lynxeye detector was used with a slit size of 1 mm. Data were collected for each sample for 2Θ values between 5 and 49°, with a step size of 0.0204°.[30]

3.2.2. Fourier Transform Infrared (FTIR) Spectroscopy

To collect the IR spectra of bulk ILs, CuBTC and IL/CuBTC samples, a Thermo Scientific Nicolet iS50 model FTIR spectrometer with an attenuated total reflection cell were used. 64 and 512 scans were collected and averaged for background and samples with 2 cm^{-1} resolution at room temperature. Fityk software was used for peak deconvolution.[30,59]

3.2.3. X-ray Fluorescence (XRF)

A Bruker S8 Tiger XRF spectrometer was used for XRF analysis under helium atmosphere. X-rays were generated by using a 4 kW Rh anode X-ray tube. Elemental compositions were determined as weight percentages by using an 18 mm mask. Firstly, approximately 0.25 g of sample was placed in XRF sample container (Chemplex Industries Inc.). Afterward, a 4 μm Prolene film support (Chemplex Industries Inc.) was placed on top of the container. Then, a ring was used to immobilize the film. The common

ppm level impurities in the measurements were Os, La, Rh, and Ca. Data interpretation was made by using the SpectraPlus Eval2 V2.2.454 software.[30]

3.2.4. Brunauer-Emmet-Teller (BET)

BET analysis was performed for CuBTC and composite samples using a Micromeritics ASAP 2020 physisorption analyzer. Approximately 150 mg of samples were used for the measurements. Prior to measurement, samples were activated at 125 °C under vacuum. Free space measurement was performed using He after the sample was cooled down to liquid nitrogen temperature. N_2 gas adsorption was performed in the pressure range of 10^{-6} and 1 bar. Pressure steps between 0.08 and 0.25 bar were used to fit the BET equation to estimate the surface area of the samples. The pore volume of the samples was obtained from the N_2 adsorption isotherm at 77 K using the t-plot method.[19,20,30]

3.2.5. Scanning Electron Microscopy (SEM)

Morphology and crystal shapes of CuBTC and IL/CuBTC composites were obtained using a Zeiss Evo LS 15 scanning electron microscope. A voltage of 3 kV was applied under vacuum condition. Working distance was approximately 6 mm for all the samples. About 5 mg of each sample was placed on the carbon tape pasted on a cell.[30]

3.2.6. Thermogravimetric Analysis (TGA)

To obtain the decomposition temperatures of bulk ILs, CuBTC and composites samples, a TA Instruments Q500 model analyzer was used. After taring the empty platinum pan, about 15 mg of samples were placed in the pan. A temperature ramp rate of 5 °C/min was employed up to 120 °C. Afterward, an isotherm at 120 °C for 8 h was used to evaporate the moisture from the samples. Then, the temperature ramp of 2 °C/min

up to 700 °C was employed under N_2 flow rates of 40 and 60 mL/min for balance and purge gases, respectively. The onset (T_{onset}) and derivative onset (T'_{onset}) temperatures were determined by extrapolation from thermogravimetry (TG) and derivative TG curves. Since T_{onset} generally overestimates the decomposition temperature compared to T_{onset}, we considered T'_{onset} values in this work.[19,20,30]

3.2.7. Gas adsorption Measurements

A micromeritics (Particulate Systems) High-Pressure Volumetric Analyzer HPVA II-200 was used for measuring the gas adsorption performance of the pure CuBTC and prepared samples.[60] Prior to adsorption measurements, approximately 0.4 g of samples were degassed at 125 °C under vacuum till the pressure reached 10^{-6} bar. After the samples were degassed, the sample holder was connected to analysis port and the temperature was cooled down to 25 °C and was kept constant during the analysis. Before the measurements, all the lines were purged with He three-times to clean and remove the residuals from previous measurements. The adsorption measurements were performed for the pressure range of 0.1-10 bar. All the isotherms were fitted to Langmuir-Freundlich model using the IAST^{++} software.[61] CO_2/CH_4 ideal selectivities were obtained by dividing the CO_2 uptake values to CH_4 uptake values at the same pressure.

After measurements were completed, the adsorption isotherms were obtained using the Excel macro provided with HPVA II. To determine adsorbed gas amounts, Dual site Langmuir and Freundlich models were fitted to single-component gas adsorption isotherms at exact pressure points. The Dual site Langmuir and Freundlich models used for fitting are given below, respectively:

$$N_{ads} = \frac{A \times P}{B + P} + \frac{C \times P}{D + P} \tag{3.1}$$

$$N_{ads} = \frac{E \times P^G}{F + P^G} \tag{3.2}$$

where N_{ads} is the adsorbed gas amount in cm^3/g STP, P is pressure in bar and A, B, C, D, E, F, and G are fitting parameters.

Ideal gas selectivities of the samples were calculated by dividing the volume amount of the more adsorbed component to the less adsorbed one at the same pressures.

Chapter 4: Influence of Different Synthesis Techniques on Structure, Thermal Stability, and Gas Separation Performance of IL/MOF Composites

In this chapter results in IL/MOF samples synthesized by different techniques are presented. The preparation methods used are wet impregnation (WIM), incipient wetness (INW), and ship-in-bottle (SIB). All prepared samples were characterized in detail using different techniques (X-ray diffraction (XRD), scanning electron microscope (SEM), Fourier transform infrared (FTIR), Brunauer-Emmett-Teller surface area (BET) and thermogravimetric analysis (TGA)) and their gas storage and separation performances were compared with each other. We selected CuBTC, HKUST-1 ($Cu_3(BTC)_2$; BTC= benzene-1,3,5-tricarboxylate) as MOF. It is a commercially available MOF and it has been studied widely in the literature. We used 1-*n*-butyl-3-methylimidazolium bromide, [BMIM][Br], as the IL in this study, as its precursors are commercially available, and we could able to prepare the composite via SIB route.

4.1. Preparation of [BMIM][Br]/CuBTC Composites

The samples prepared via wet impregnation (WIM), incipient wetness (INW) and ship in a bottle (SIB) were denoted as [BMIM][Br]/CuBTC-WIM, [BMIM][Br]/CuBTC-INW and [BMIM][Br]/CuBTC-SIB, respectively. The synthesis procedures were presented in detail in Chapter 3.

4.2. Characterization of Composite Samples

4.2.1. Powder X-Ray Diffraction

To examine the crystal structure of IL/MOF composites, XRD analysis was performed. Figure 1 shows the XRD patterns of CuBTC and composite samples.

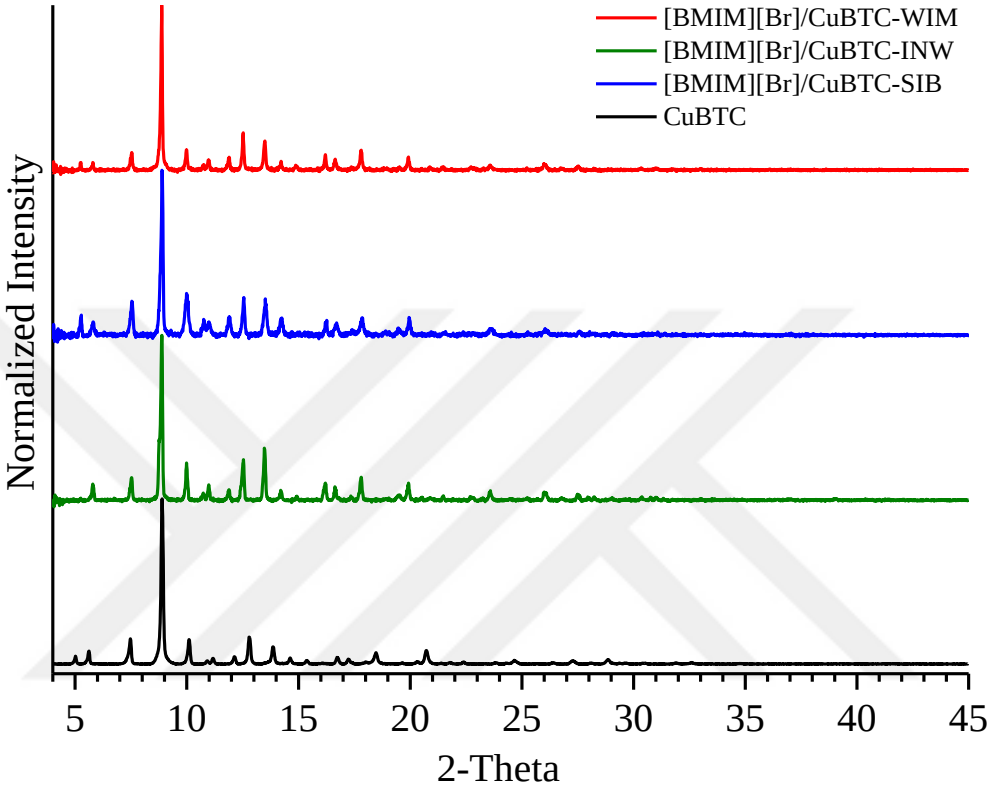

Figure 4.1. X-ray diffraction patterns of CuBTC, [BMIM][Br]/CuBTC samples.

Figure 4.1 shows that XRD features of CuBTC are preserved in composite samples. We infer that crystal structure of CuBTC was not changed in three of the synthesis routes considered and [BMIM][Br] incorporation into CuBTC did not affect the crystallinity of parent CuBTC.[19,30] There are slight changes in intensities of some features in IL/MOF samples compared to CuBTC. These changes are originated from the changes in the electronic environment of CuBTC upon IL incorporation.[40]

4.2.2. Scanning Electron Microscopy (SEM) of CuBTC and Composites

To confirm the stability of framework and crystal structure of samples, SEM analysis was performed for CuBTC and prepared samples. Figure 4.2 illustrates the SEM images of CuBTC and [BMIM][Br]/CuBTC samples.

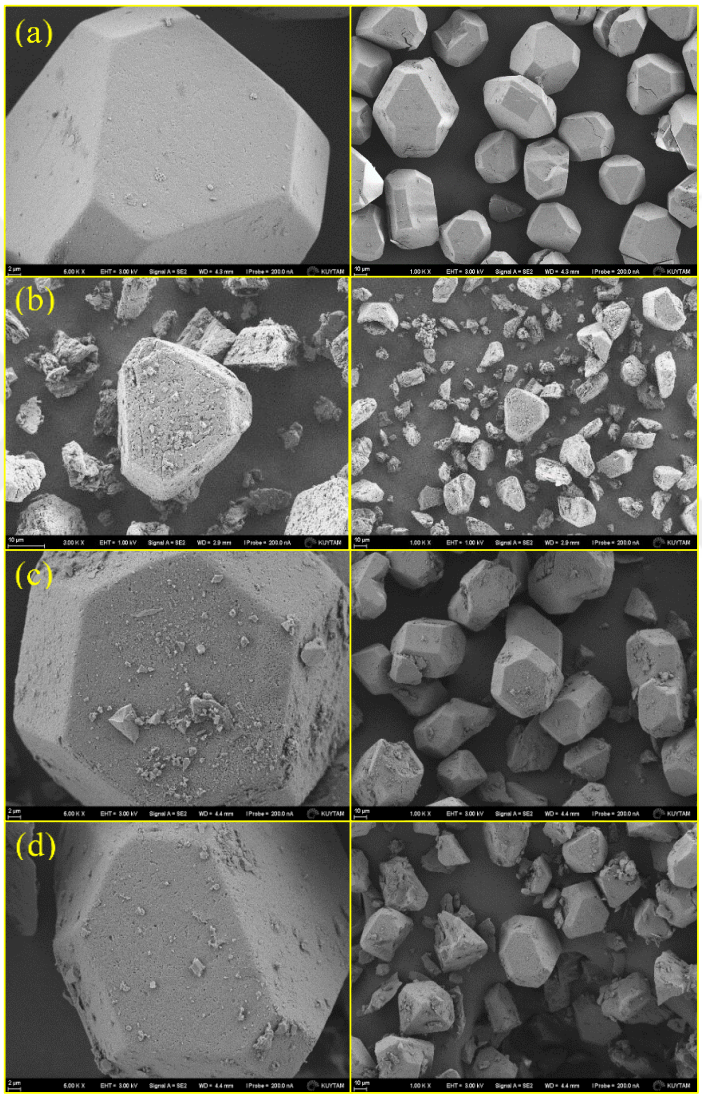

Figure 4.2. SEM images of (a) CuBTC; (b) [BMIM][Br]/CuBTC-SIB; (c) [BMIM][Br]/CuBTC-INW; (d) [BMIM][Br]/CuBTC-WIM.

It can be clearly seen that the morphology and crystal shape of the CuBTC are almost the same in all of the samples expect for slight changes in the morphology of [BMIM][Br]/CuBTC-SIB. These small changes in [BMIM][Br]/CuBTC-SIB can be attributed to relatively harsh synthesis conditions used compared to INW and WIM techniques.[48] Accordingly, small particles remaining on the crystals and it might show the presence of IL deposited on the surface of crystals.[30] Compared to other preparation methods, the sample prepared via INW has more IL deposition on the crystals as confirmed by SEM images and also lower BET surface area and pore volume in INW method which indicates IL molecules might deposit on the external surface of the MOF and block pore openings.[30] It can be attributed to insufficient mixing or time required for IL to enter the MOF cages compared to other techniques. Furthermore, the temperature difference between synthesis methods might be another parameter affecting the diffusion of IL to MOF cages.

4.2.3. FTIR Spectroscopy Results of CuBTC and Composite samples

To confirm the presence of IL in CuBTC, we perform FTIR measurements for bulk [BMIM][Br], CuBTC, and [BMIM][Br]/CuBTC samples. Figure 4.3 shows the FTIR spectra of samples.

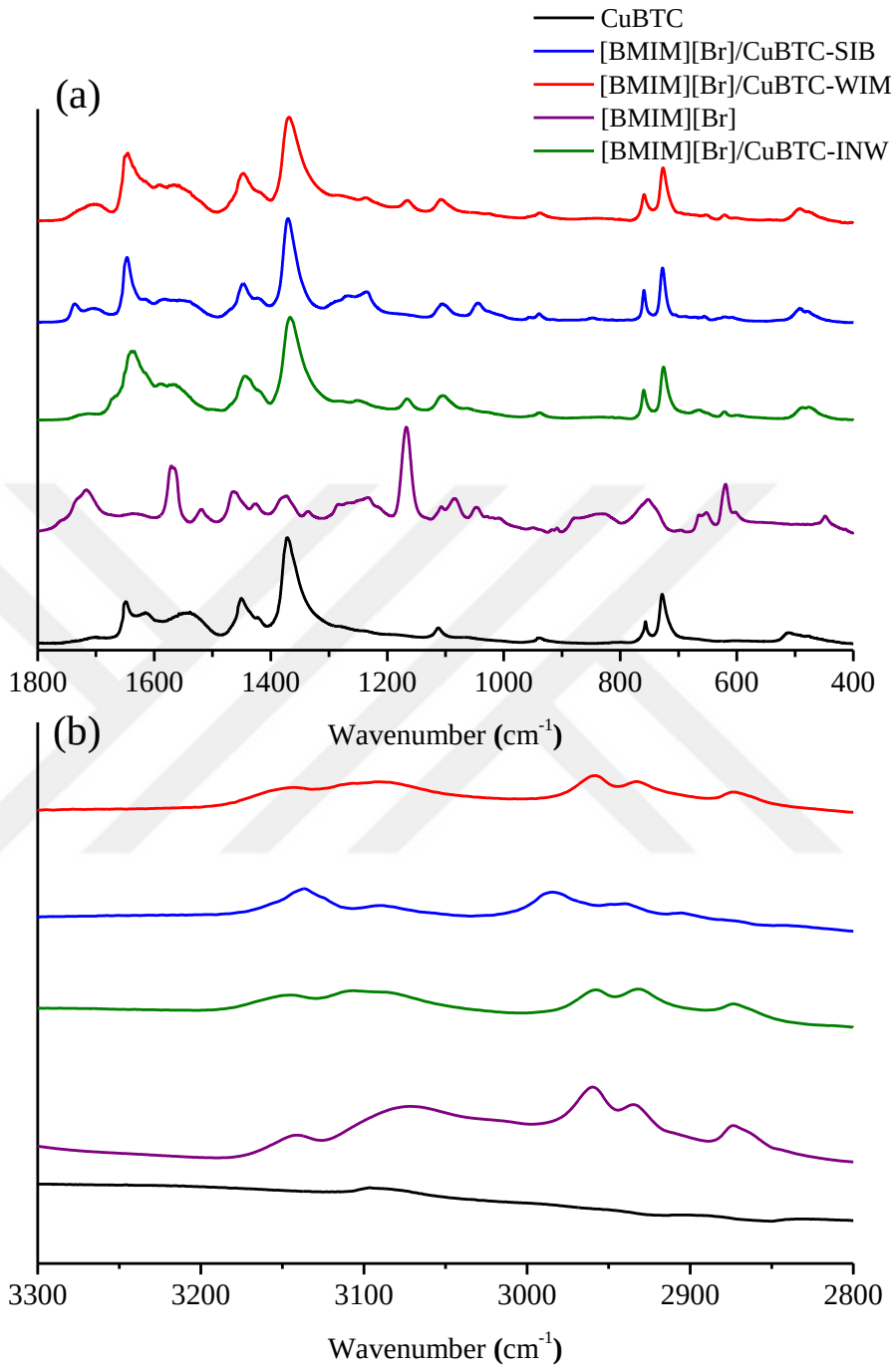

Figure 4.3. FTIR spectra of bulk [BMIM][Br], CuBTC and [BMIM][Br]/CuBTC samples; (a) 1800 and 400 and (b) 3300 and 2800 cm^{-1}.

According to Figure 4.3, it can be seen that [BMIM][Br] features are present in all the composite samples. This result confirms the presence of IL in all of the incorporated samples.[19,30] Moreover, the presence of CuBTC features in composite material's spectra shows the framework integrity of CuBTC in all the samples and this observation is consistent with XRD and SEM measurements. There are slight shifts in some IR features of bulk [BMIM][Br] compared to composite sample (IL/MOF-IL) features as presented in Tab1e 4.1. These shifts are attributed to the interactions between [BMIM][Br] and CuBTC.

Table 4.1. Band shifts in [BMIM][Br] features compared to composite samples. (spectra resolution is 2 cm^{-1})

Band (cm^{-1})	[BMIM][Br]/CuBTC-WIM (cm^{-1})	[BMIM][Br]/CuBTC-INW (cm^{-1})	[BMIM][Br]/CuBTC-SIB (cm^{-1})
619	3	2	1
753	-3	-2	3
1167	-2	-3	7
1460	5	2	12
1571	-5	-2	-15
2871	3	-1	4
2931	1	-1	11
2958	0	2	25
3064	27	22	23
3140	12	10	13

It can be seen from Table 4.1 that in most of the features, band shifts in [BMIM][Br]/CuBTC-SIB sample are higher than that of [BMIM][Br]/CuBTC-WIM and [BMIM][Br]/CuBTC-INW samples. This result indicates that [BMIM][Br] is interacting more with the framework compared to other samples since the IL molecules were

synthesized inside the CuBTC cages. [BMIM][Br]/CuBTC-WIM band shifts are higher in some of the features compared to [BMIM][Br]/CuBTC-INW sample. This result shows that [BMIM][Br] molecules have less interaction with the framework and it is attributed to the presence of some IL molecules on the external surface of CuBTC consistent with the results of BET and SEM analyses.

4.2.4. BET Surface Area and Pore Volume Analysis of CuBTC and Composite Samples

Table 4.1 shows the BET results obtained for CuBTC and IL/CuBTC samples. From BET measurements we observed that both pore volume and BET surface area of parent CuBTC were decreased upon incorporation of [BMIM][Br], consistent with the previous reports.[19,20,30]

Table 4.2. BET surface area and Pore volumes of CuBTC and [BMIM][Br]/CuBTC samples.

Sample	S_{BET} (m^2/g)	Pore volume (cm^3/g)
CuBTC	1324	0.522
[BMIM][Br]/CuBTC-SIB	546	0.243
[BMIM][Br]/CuBTC-WIM	460	0.206
[BMIM][Br]/CuBTC-INW	208	0.093

BET surface area and pore volume in [BMIM][Br]/CuBTC-INW were decreased significantly compared to other samples. This change might be attributed to blockage of some pores while preparing the sample via INW technique. As mentioned before, [BMIM][Br] molecules had less time to diffuse inside the pores and might be occupying some space outside the pores.

4.2.5. Thermogravimetric Analysis of CuBTC and Composite Samples

To investigate the thermal stability limits of IL/MOF samples and assess the effects of synthesis methods, TGA measurements were performed for bulk [BMIM][Br], pristine CuBTC and [BMIM][Br]/CuBTC samples. Figure 4.4 demonstrates the thermogravimetric (TG) and derivative TG curves (DTG) of the samples.

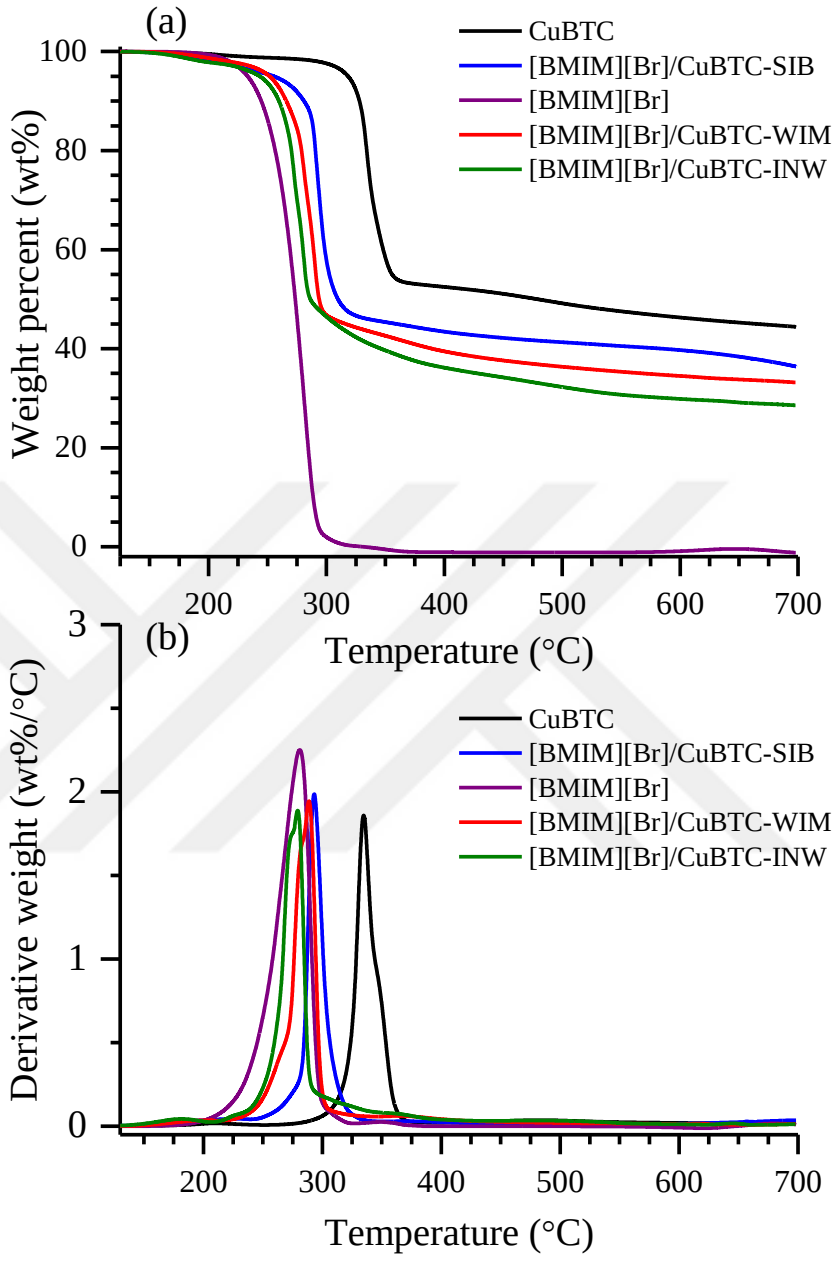

Figure 4.4. Thermal stability of CuBTC, [BMIM][Br], and [BMIM][Br]/CuBTC samples: (a) TG curves and (b) DTG curves.

Figure 4.4 shows that decomposition of [BMIM][Br]/CuBTC samples start at higher temperatures compared to bulk [BMIM][Br]. Moreover, Figure 1(a) illustrates that

some sample left from the TGA measurement of [BMIM][Br]/CuBTC. This result shows direct interactions between IL and MOF, as discussed in previous studies. Table 4.2 summarizes the onset, T_{onset}, and derivative onset, T'_{onset} of CuBTC, [BMIM][Br], and [BMIM][Br]/CuBTC samples.

Table 4.3. Onset, T_{onset}, and derivative onset, T'_{onset} of CuBTC, [BMIM][Br], and [BMIM][Br]/CuBTC samples.

Sample	T_{onset} (°C)	T'_{onset} (°C)
CuBTC	326	314
[BMIM][Br]	248	238
[BMIM][Br]/CuBTC-SIB	286	282
[BMIM][Br]/CuBTC-WIM	265	250
[BMIM][Br]/CuBTC-INW	262	248

According to Table 4.2, [BMIM][Br]/CuBTC-SIB sample is more stable (282 °C) compared to [BMIM][Br]/CuBTC-WIM and [BMIM][Br]/CuBTC-INW samples which decompose at 250 and 248 °C, respectively. This difference in T'_{onset} values might be originating from the presence of more [BMIM][Br] molecules inside CuBTC since [BMIM][Br] was synthesized inside the pores' of CuBTC.[62] This result is consistent with IR band shifts in [BMIM][Br]/CuBTC-SIB sample which was higher than other samples showing that most of the [BMIM][Br] molecules are located inside the cages. We note that T'_{onset} for IL/MOF samples is higher than that of bulk [BMIM][Br] in all three composite samples. This result indicates that thermal stability of [BMIM][Br] is increased while it was confined inside CuBTC. It can be concluded that synthesis method is an important parameter in thermal stability limits of IL/MOF composites.

4.3. Gas Adsorption and Gas Separation Performance of CuBTC and Composite samples

We investigated the effect of different preparation techniques in gas adsorption and separation performance of IL/MOF composites. Figure 4.5 shows CO_2 and CH_4 uptakes obtained from volumetric gas adsorption measurements at room temperature and corresponding CO_2/CH_4 ideal selectivity.

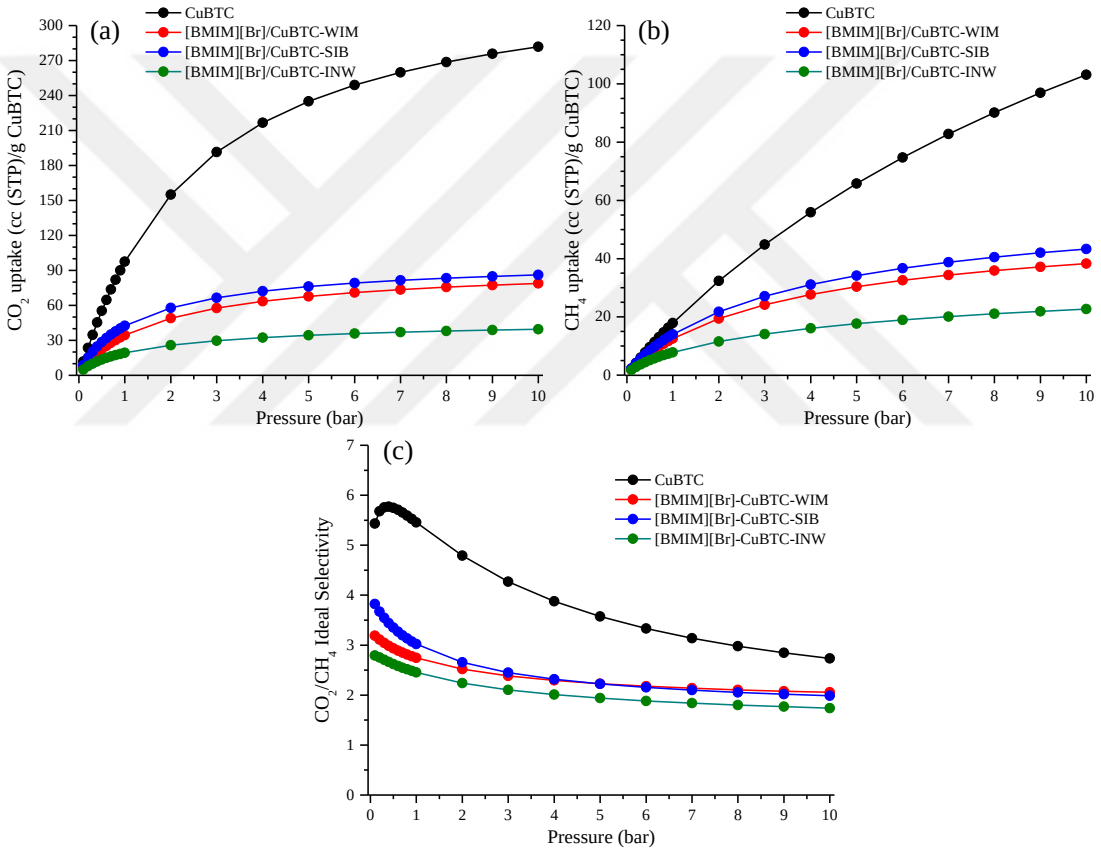

Figure 4.5. Adsorption isotherms for CuBTC, [BMIM][Br]/CuBTC-WIM, [BMIM][Br]/CuBTC-SIB, and [BMIM][Br]/CuBTC-INW; (a) CO_2 isotherms; (b) CH_4 isotherms, and (c) CO_2/CH_4 ideal selectivity at 298 K.

Figure 4.5 (a) and (b) shows that [BMIM][Br]-incorporated CuBTC samples have lower CO_2 and CH_4 uptakes in each pressure compared to pristine CuBTC. This is attributed to the presence of IL inside the MOF and interaction of IL molecules with open metal sites of CuBTC which were previously available for guest molecules.[30,63] Among different [BMIM][Br]/CuBTC prepared using different techniques, [BMIM][Br]/CuBTC-SIB and [BMIM][Br]/CuBTC-WIM composites have better performance in gas uptake compared to [BMIM][Br]/CuBTC-INW composite. Since IL molecules block some of the cage openings in CuBTC; consequently, gas molecules cannot enter the available pore space in CuBTC resulting in a lower gas adsorption. This result is consistent with the BET surface area measurements. Figure 4.5 (c) demonstrates that [BMIM][Br]/CuBTC-SIB sample has a higher CO_2/CH_4 selectivity compared to other samples. It can be concluded that ship-in-bottle technique is a better method for the application of IL/MOF composites in gas adsorption and gas selectivity. However, this method has some shortcomings compared to other techniques. For synthesizing different combination of IL/MOF composites, ship-in-bottle techniques cannot be used as there is a very limited number of IL precursors are commercially available. Moreover, the preparation method is not energy and time efficient compared to other techniques. By taking all above-mentioned results into consideration, we can conclude that wet impregnation technique is a proper way of preparing any combination IL/MOF composites.

Chapter 5: Toward Rational Design of Ionic Liquid/Metal-Organic Framework Composites: Effects of Interionic Interaction Energy[1]

Combining different ILs with different MOFs leads to composite materials with various gas adsorption and separation performances. The research on applications of IL/MOF composites is rapidly growing.[38,64–66] One of the main challenges is that this field is too new and the rationale behind the proper choice of ILs and MOFs has not been fully understood yet. This fundamental level information is crucial for the rational design of such materials. This is why there is a strong need for elucidating the structural factors controlling the interactions in IL/MOF composites and their consequences on the gas storage and gas separation performance. In the way of contributing to overcome this challenge, here, we report a structural factor in ILs, which we identified to have a strong influence not only on the gas storage performances but also on the thermal stability limits of IL/MOF composite. When an IL is incorporated into the pores of MOFs, it interacts with the framework. This interaction can be physical and/or chemical based on the type of the IL and MOF. If the cation of the IL is fixed and the anion is changed, the cohesion energy between the cation and the anion can be systematically varied. As the cohesion energy between the ion moieties changes, the hydrogen bonding strength between ions will be changed. As a result of these changes in the hydrogen bonding strength, the 'inter-ionic interaction energy' between the cation and the anion is modified. According to the previous studies in the literature, the strength of the inter-ionic interaction energy between the cation and anion can be probed by the stretching IR frequency of the most acidic proton site on the imidazolium cation (C2H, where C2 is the carbon between two N sites

[1] The results given in this chapter were published in *ACS Omega* with the following reference: Nozari, V.; Keskin, S.; Uzun, A. Toward Rational Design of Ionic Liquid/Metal–Organic Framework Composites: Effects of Interionic Interaction Energy. *ACS Omega* **2017**, *2* (10), 6613–6618. This chapter is the reformatted version of published paper.

in the ring).[67–75] Motivated from this point, we examined the consequences of the changes in inter-ionic interaction energy in bulk ILs, which can be probed spectroscopically via C2–H stretching frequency, ν(C2H), on the thermal stability limits and gas adsorption performances of IL/MOF composites.

5.1. Preparation of Imidazolium-Based IL/MOF Composites

All the IL/MOF composites were prepared via wet impregnation route with approximately 30 wt% stoichiometric IL loading which was explained in Chapter 3. We started with CuBTC, one of the most widely studied MOFs for IL incorporation as reviewed above. It has open metal sites which directly participate in gas adsorption. Thus, it is expected to observe a direct influence of the IL molecules on these sites when they are inside the pores. The ILs considered here were chosen from a family of ILs with the same cation, 1-butyl-3-methylimidazolium, $[BMIM]^+$, having different anions: bis(trifluoromethylsulfonyl)imide, $[NTf_2]^-$, methylsulfate, $[MeSO_4]^-$, hexafluoroantimonate, $[SbF_6]^-$, thiocyanate, $[SCN]^-$, trifluoromethanesulphonate, $[CF_3SO_3]^-$, methanesulfonate, $[MeSO_3]^-$, and octylsulfate, $[OcSO_4]^-$. Because these ILs have the same cation, their inter-ionic interaction strengths can be probed and quantified by the corresponding ν(C2H) band position.

5.2. Characterization of Imidazolium-Based IL/MOF Composites

The resulting structures were fully characterized by X-ray fluorescence (XRF), X-ray diffraction (XRD), X-ray fluorescence (XRF), scanning electron microscope (SEM), Fourier transform infrared spectroscopy (FTIR), Brunauer-Emmett-Teller (BET) surface area analysis and Barrett-Joyner-Halenda (BJH) pore size and volume analysis, and thermogravimetric analysis (TGA), as reported previously.[18–20]

5.2.1. Brunauer-Emmett-Teller (BET) Surface Area and Pore Volume Analysis

From the BET measurements, we observed that the pore volume and BET surface area decreased in each IL/MOF sample as compared to pristine CuBTC (Table A.1). This decrease indicates the presence of ILs inside the MOF, consistent with our previous reports.[18–20] However, we note that BET measurements are based on the N_2 adsorption which can be directly influenced by the presence of IL inside the MOF cages. Because N_2 might be dissolved in different ILs at different levels, these BET results might be misleading in terms providing quantitative results. For instance, the IL loading calculations based on the change in pore volumes upon IL incorporation fail to estimate the loadings. For instance, the estimated values for some of the samples were even higher than the stoichiometric amounts of individual components used in the synthesis (Table A.1). Thus, the IL loadings in each sample were determined by XRF as listed in Table A.1.

5.2.2. Powder X-Ray Diffraction (XRD) and Scanning Electron Microscopy Results of Imidazolium-Based IL/MOF Composites

The XRD results and SEM analysis, given in Figures A.1-2, confirmed that the crystal structure and morphology of the CuBTC were preserved upon the IL incorporation.

5.2.3. Fourier Transform Infrared Spectroscopy (FTIR) Analysis

The FTIR measurements (Figures A.3-9) also indicate that the IL and MOF structure remain intact with slight changes in the positions and intensities of some of the IR features. These changes were inferred to be related with the interactions between the IL molecules and the CuBTC.[18–20]

5.3. Results and Discussion

Because, the IL is expected to interact directly with the unsaturated Cu sites,[28,76] we focused on a band at 480 cm^{-1} associated with (Cu–O) stretching frequency, ν(Cu–O). This band provides information regarding the electronic environment over the Cu sites, which should be influenced strongly by the presence of interactions between the IL and MOF. Thus, ν(Cu–O) band position was used as a probe to quantify these interactions. For instance, when the IL was [BMIM][SCN], this band presents a red shift of approximately 9 cm^{-1}. This red shift indicates a weakening in Cu–O bond probably because of the electron sharing between the unsaturated Cu atoms and the IL leading to a decrease in electron density on the Cu sites to be shared with the framework oxygen atoms. This result is consistent with Dhumal et al.[63] showing a decrease in Cu–O bonding strength as a result of interactions between IL and CuBTC.

As stated above, the ILs selected for this study have the same cation, $[BMIM]^+$. The proton attached to the C2 position between two nitrogen atoms of the imidazolium ring in $[BMIM]^+$ is the most acidic proton, which is responsible for strong directional and localized hydrogen bonding between the cation and anion of the IL. Therefore, its stretching frequency, ν(C2H) can be used as a measure of inter-ionic interaction energy in ILs.[67,68,70–75] Accordingly, the inter-ionic interaction energy becomes stronger with a red shift in ν(C2H).[70,73,75] Thus, we evaluated the variations in ν(Cu–O) in IL/MOF composites with ν(C2H) band position of the corresponding IL to elucidate the dependency of the electronic and bonding environment of the open metal sites in CuBTC on the inter-ionic interaction energy in ILs.

Figure 5.1 illustrates that there is a correlation (R^2 = 0.73) between the amount of red shift observed on ν(Cu–O) band position and ν(C2H) of ILs. Accordingly, the red shift amount on ν(Cu–O) increases as the inter-ionic interaction energy in ILs increases (with a decrease in ν(C2H)). Thus, we infer that the Cu–O bonding in IL/MOF samples becomes weaker in the presence of IL. Based on the results presented in Figure 5.1, we

infer that the degree of this weakening in Cu–O bonding is the highest when the inter-ionic interaction is the strongest. This behaviour originates from the fact that the increase in inter-ionic interactions in ILs is associated with an increase in the ionic character of the ions. This stronger ionic character enables ILs to interact more strongly with the unsaturated Cu sites, leading to a weakening in Cu–O bonding (as evidenced by a red shift in ν(Cu–O)). Thus, we infer that the inter-ionic interaction energy in ILs is an important structural parameter controlling the electronic environment over the gas adsorption sites in CuBTC. We note that among all the ILs considered here only [BMIM][$OcSO_4$] does not represent a good fit in Figure 1 (with red shift in ν(Cu–O) and ν(C2H) values of 4.6 cm^{-1} and 3107 cm^{-1}, respectively). This IL has a significantly large anion compared to others we considered in this work.[77] Thus, the size of the anion should be another structural parameter which is playing a role in sterically constraining the interactions between the IL and the open metal sites of the MOF. When excluding this specific IL from the fit presented in Figure 5.1, the correlation coefficient increases from 0.73 to 0.95 presenting a very strong correlation.

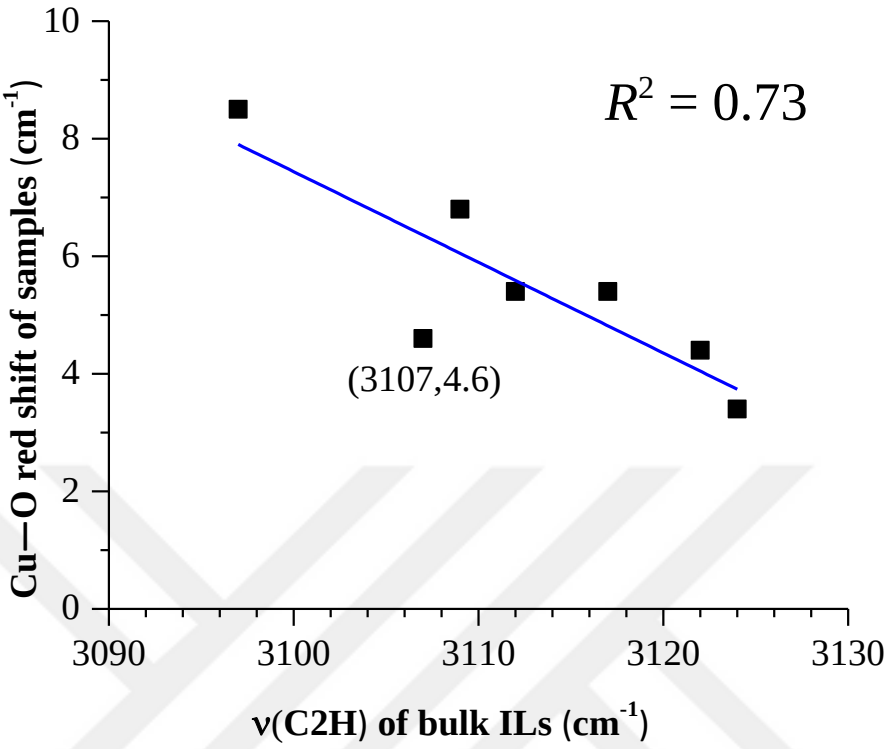

Figure 5.1. Correlation between ν(C2H) of bulk ILs and Cu–O red shifts in IL/MOF samples.

These results suggest that one can tune the electronic environment over the open metal sites by changing the IL structure. Moreover, as illustrated previously,[4019] it is also possible to adjust the available pore size and shape of the MOFs by the type and loading of IL. This ability offers a broad potential to control the performance of IL/MOF composites for various applications, such as gas adsorption,[39] membrane-based gas separation,[78] catalysis,[53,79] and ionic conductivity.[80] Because, for these applications the open metal sites are the sites for adsorption, thus, their electronic environment directly determines the performance in the related application. In any of these applications, one of the key points is that the structure of the composite should remain intact under application conditions. Thus, we investigated the consequences of changes in inter-ionic interaction energy in ILs on the thermal stability limits of these composites. Figure 5.2

illustrates the variation of T'_{onset} of IL/MOF composites, indicating the temperature at which the thermal decomposition starts, with ν(C2H) band position of the corresponding IL.

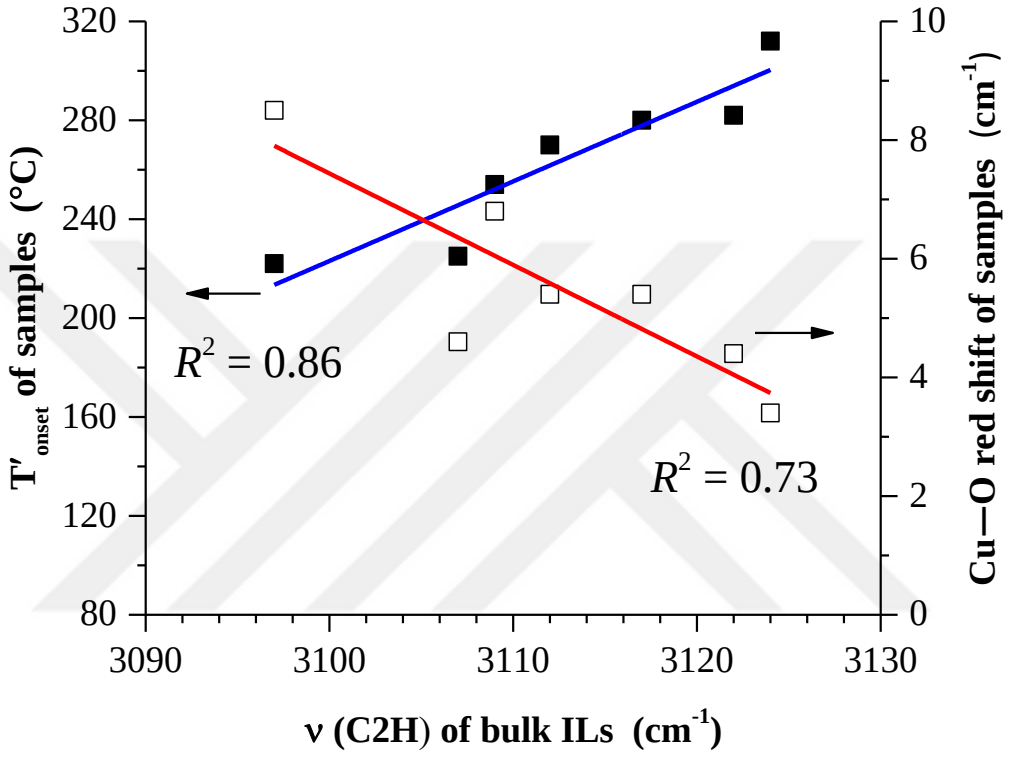

Figure 5.2. Correlation between T'_{onset} of IL/MOF composites (left y-axis) and ν(C2H) of bulk ILs. The vertical axis on the right shows the correlation between the corresponding red shift in ν(Cu–O) and ν(C2H) of bulk ILs.

Accordingly, the thermal stability limits of IL/MOF composites decrease linearly with an increase in the inter-ionic interaction energy (probed by a decrease in ν(C2H)) associated with an increase in the degree of red shift in ν(Cu–O). This strong correlation indicates that the interactions between the IL and open Cu sites are the dominant factors in determining the decomposition mechanism of the composite. Moreover, the correlation

presented in Figure 5.2 can perfectly predict the decomposition temperature of an analogous [BMIM][BF_4]/CuBTC composite (with a corresponding ν(C2H) value of 3124 cm^{-1} for [BMIM][BF_4][20]) within a few degrees, confirming the validity of this correlation.[18] Thus, we infer that the inter-ionic interaction energy of the ILs has a strong influence on the characteristics of the IL/MOF composites. When it is higher, the IL interacts with Cu sites more strongly. This change lowers the stability limit suggesting that interactions between IL–MOF play a major role in thermal decomposition.

Aiming at elucidating the corresponding influence on gas storage performance of the composites, we performed high pressure volumetric uptake measurements for CO_2 and CH_4. Here we note that the gas uptake values normalized per gram of CuBTC because our ultimate aim is to show how the presence of ILs influences the gas uptake performance of the MOF materials. In other words, IL-incorporated MOFs can be considered as functionalized MOFs and we aimed to directly compare the amount of gas being adsorbed by the functionalized material containing the same amount of MOF. Figure 5.3 (a) illustrates the variation of CO_2 uptake in IL/CuBTC samples with an increase in ν(C2H) of the IL at 1 bar. Data show that the CO_2 uptake decreases with an increase in inter-ionic interaction energy in ILs (with a decrease in ν(C2H)). As the open metal sites in CuBTC interact more strongly with the anion of the IL, they become less available for gas adsorption (as evidenced from a weakening in Cu–O bond). Confirming this inference, Figure 5.3 (b) illustrates a similar trend for CH_4 uptake with even a higher degree of correlation. This result also suggests that these correlations strongly depend on the pressure.

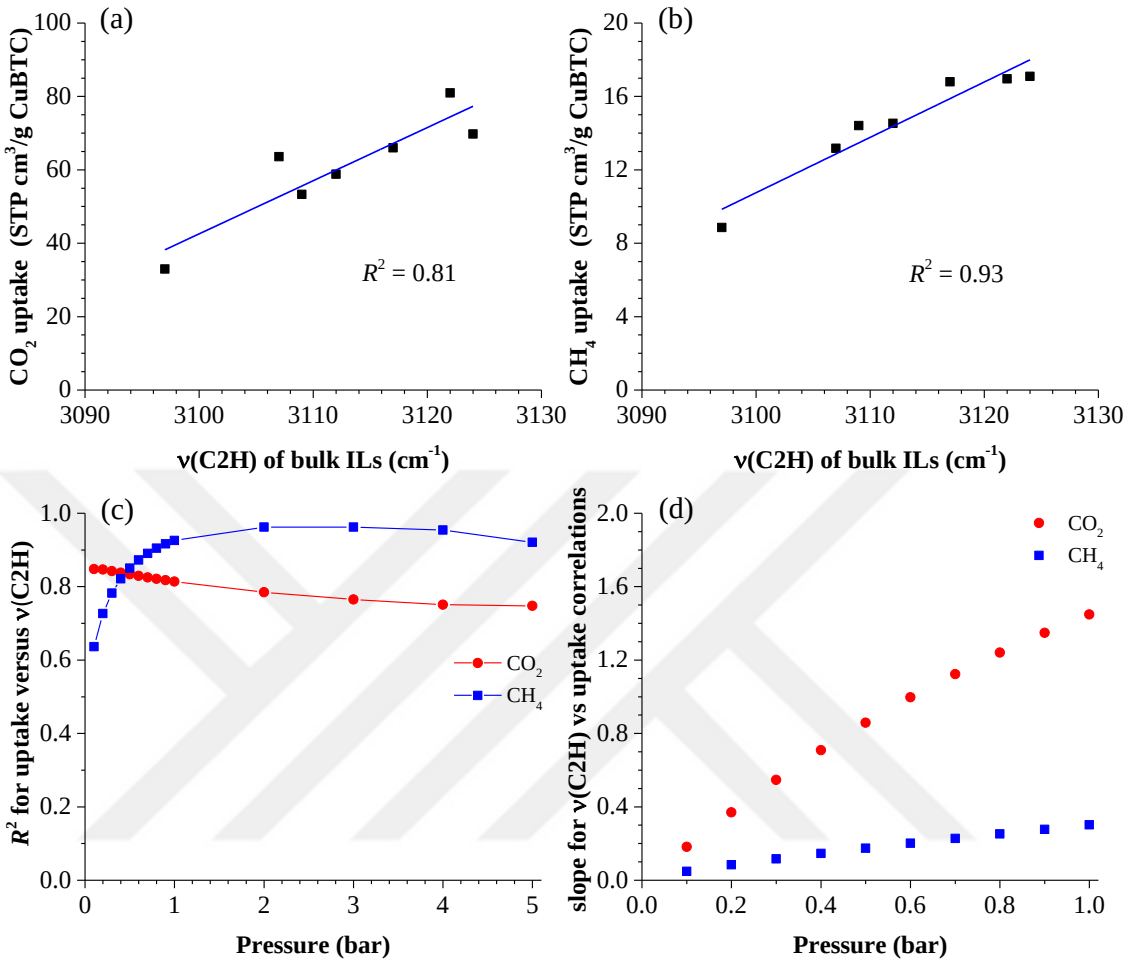

Figure 5.3. Correlation between CH_4 and CO_2 uptakes versus ν(C2H) of bulk ILs: (a) CO_2 uptake at 1 bar; (b) CH_4 uptake at 1 bar; (c) Correlation coefficients for CO_2 uptake and CH_4 uptake at different pressures (a line was added between the points to guide the eye); (d) Slope for correlations between ν(C2H) and gas uptakes.

Figure 5.3 (c) shows the R^2 values of these correlations as a function of pressure. Accordingly, the R^2 value for CH_4 is as low as 0.63 at very low pressure region because of the weak interactions of CH_4 molecules with the open metal sites at very low pressures. However, it quickly increases to values higher than 0.9 with increasing pressure. CO_2, on the other hand, has quadrupole moments facilitating efficient interactions with the MOF

at the very low pressure region.[81] Thus, its R^2 starts from a value above 0.8 at very low pressures and gradually decreases with increasing pressure. We note that at high pressures, the available pore space is the dominant factor for gas adsorption evidenced by the decrease in R^2 with increasing pressure. Moreover, Figure 5.3 (d) represents the change in slope of correlations between the corresponding gas uptakes in IL/MOF composites and ν(C2H) of the ILs. Data show that the slope for the correlation of CO_2 uptake with ν(C2H) is always higher than that of CH_4 uptake. Thus, we infer that the inter-ionic interaction energy in ILs plays a dominant role in controlling the CO_2 uptake, however, it is not that effective for controlling CH_4 uptake especially at low pressures. Similar to the case with the decomposition temperature, CH_4 and CO_2 uptakes for a previously reported analogous [BMIM][BF_4]/CuBTC composite[18] can be estimated within less than ±5% error from the correlations presented in Figure 5.3 confirming their validity.

Chapter 6: Towards Rational Design of Ionic Liquid/Metal Organic Framework Composites: Effect of Methylation in Ionic Liquid

In this chapter, we investigated the effect of methylation in a commercially available and widely studied IL (1-*n*-butyl-3-methylimidazolium hexafluorophosphate, [BMIM][PF_6]), on the interactions between the IL molecules and a MOF with open metal sites (CuBTC, $Cu_3(BTC)_2$, BTC is benzene-1,3,5-tricarboxylate). Moreover, the effects of methylation in IL on the thermal stability limit and the gas adsorption/separation performance of IL/MOF composite are demonstrated. Results showed that thermal stability limits of the IL/MOF composites change with the methylation on the IL. Moreover, methylation in the IL resulted in a decrease in N_2 adsorption compared to that in CH4 and CO2 uptakes, offering an increase in CO_2/N_2 and CH_4/N_2 selectivities.

6.1. Preparation of [BMIM][PF_6]/CuBTC and [BMMIM][PF_6]/CuBTC Composites

We selected [BMIM][PF_6] (1-*n*-butyl-3-methylimidazolium hexafluorophosphate) and its' methylated type, [BMMIM][PF_6] (1-*n*-butyl-2,3-dimethylimidazolium hexafluorophosphate) and incorporated into CuBTC using wet impregnation method discussed in chapter 3.

6.2. Characterization of Composite Samples

After sample preparation, the composites were characterized in detail by XRD, XRF, SEM, FTIR, BET, and TGA.

6.2.1. X-ray Fluorescence (XRF) of composite samples

To determine the IL loadings, XRF analysis was performed. Results showed that [BMIM][PF_6] and [BMMIM][PF_6] loadings in [BMIM][PF_6]/CuBTC and [BMMIM][PF_6]/CuBTC sample were approximately 20 ± 1 wt% .

6.2.2. BET Surface Area and Pore Volume Analysis of CuBTC and Composite Samples

Table 1 shows the BET results obtained for CuBTC and IL/CuBTC composites.

Table 6.1. BET surface area and pore volumes of CuBTC, [BMIM][PF_6]/CuBTC and [BMMIM][PF_6]/CuBTC samples.

sample	S_{BET} (m^2/g)	Pore volume (cm^3/g)
CuBTC	1324	0.522
[BMIM][PF_6]/CuBTC	364	0.186
[BMMIM][PF_6]/CuBTC	306	0.143

Accordingly, both pore volume and BET surface area of parent CuBTC were decreased upon incorporation of [BMIM][PF_6] and [BMMIM][PF_6]. The decrease in BET surface area and pore volume is higher in [BMMIM][PF_6]/CuBTC compared to the one in the composite with non-methylated IL. This difference is attributed to slightly higher specific volume of [BMMIM][PF_6] to that of [BMIM][PF_6].

6.2.3. X-ray Diffraction (XRD) patterns of CuBTC and composite samples

To examine the crystal structure of the composites, XRD analysis was performed. Figure 6.1 shows that XRD features of CuBTC are preserved in the composites.

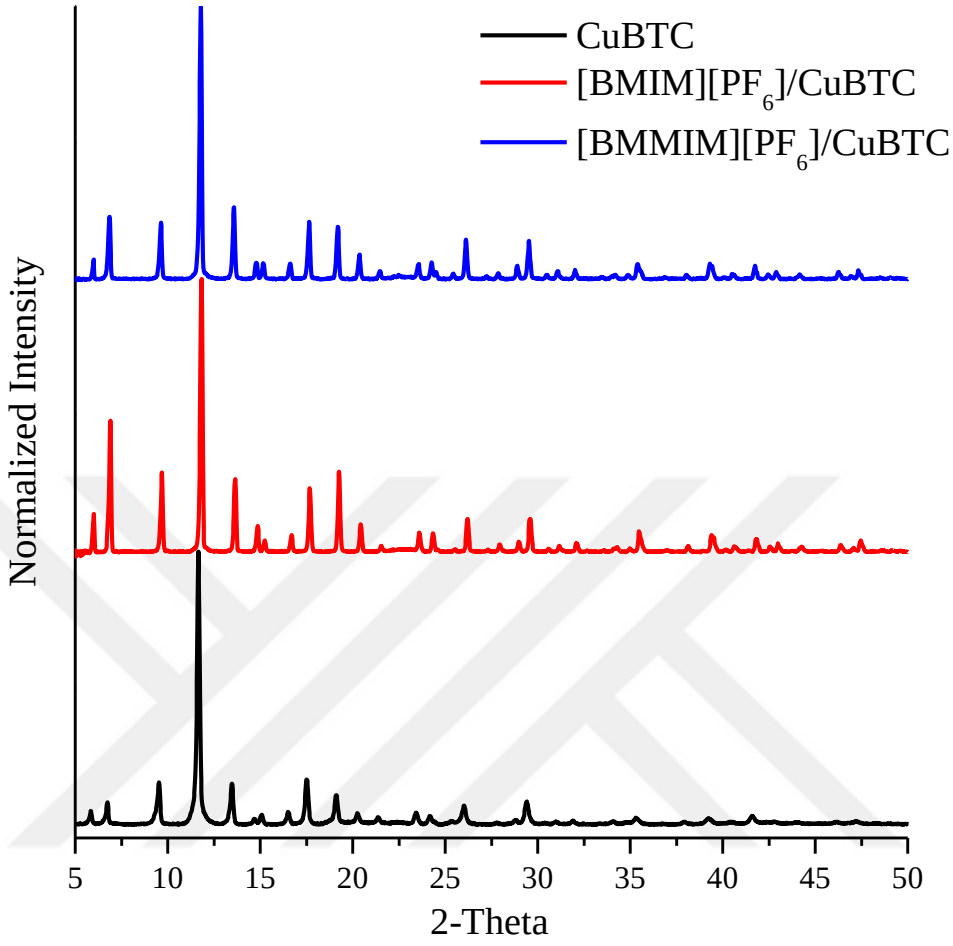

Figure 6.1. XRD patterns of CuBTC, [BMIM][PF_6]/CuBTC and [BMMIM][PF_6]/CuBTC samples.

Figure 6.1 shows that there are slight changes in the intensity of some of the features in [BMIM][PF_6]/CuBTC and [BMMIM][PF_6]/CuBTC samples compared to pristine CuBTC. This can be originated from a change in electronic environment over some planes after IL incorporation. We note that the degree of this change depends on how the IL molecules are interacting with the framework. Based on these XRD results, we infer that methylation in [BMIM][PF_6] does not damage the crystal structure of the MOF.

6.2.4. Scanning Electron Microscopy (SEM) of CuBTC and IL/CuBTC Composites

To confirm the crystal structure of IL/MOF samples, the morphology of the samples was investigated using SEM. Figure 6.2 illustrates the SEM images of CuBTC, [BMIM][PF_6]/CuBTC, and [BMMIM][PF_6]/CuBTC samples. It can be clearly seen that the morphology and crystal shape of the CuBTC are almost the same in the composite samples.

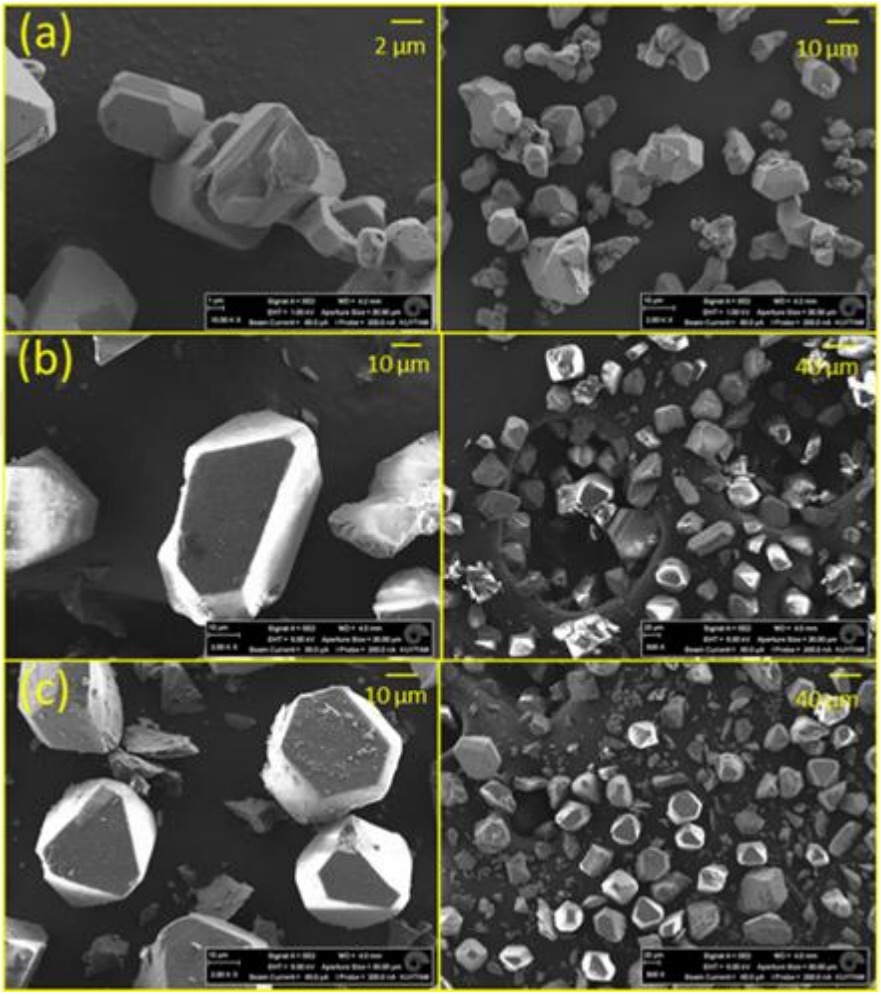

Figure 6.2. SEM images of (a) CuBTC; (b) [BMIM][PF_6]/CuBTC and (c) [BMMIM][PF_6]/CuBTC.

This result is consistent with the XRD results. We infer that crystal structure of CuBTC remained intact upon incorporation of both ILs and the methylation does not affect the crystallinity of the CuBTC.[18,19,30]

6.2.5. Confirmation of Internally Incorporated IL Molecules

To confirm the incorporation of [BMIM][PF_6] and [BMMIM][PF_6] inside the CuBTC, composites were washed with toluene, a hydrophobic solvent[82] that can dissolve [BMIM][PF_6] and [BMMIM][PF_6][83] and large enough (7.5 Å)[84] that cannot enter the CuBTC pore openings (3.4 Å).[85] Results in Figure C3-C4 show that this washing process could not remove [BMIM][PF_6] and [BMMIM][PF_6] from the composites, confirming that [BMIM][PF_6] and [BMMIM][PF_6] were internally incorporated inside the CuBTC, consistent with previous reports.[18–20,30]

6.2.5. FTIR Spectroscopy Results of CuBTC, Bulk ILs and Composite samples

Our previous studies proved that there are some interactions between the IL molecules and the MOF.[18–20,30] To elucidate the interactions, we performed FTIR analysis and the results are shown in Figure 6.3. According to Figure 6.3, spectra of composites show that both ILs and MOF features are still present, showing that IL and MOF structures are intact in the composites, consistent with XRD results. It can be seen from Figure 6.3 that some of the IL bands are shifted in the spectra of composites. These shifts are attributed to interactions between the IL molecules and CuBTC.[18–20,30,63]

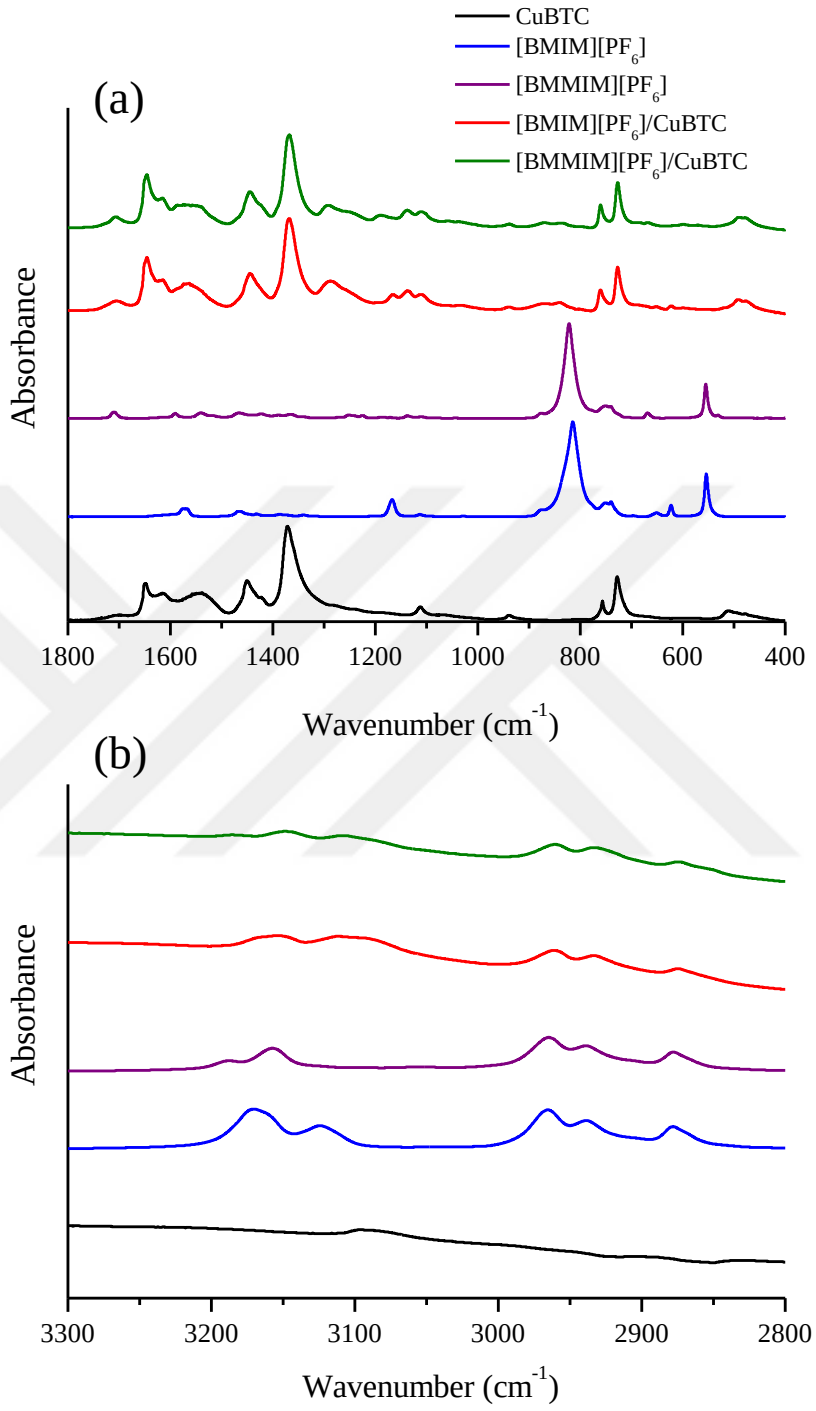

Figure 6.3. FTIR spectra of bulk [BMIM][PF_6], CuBTC, [BMIM][PF_6]/CuBTC and [BMIM][PF_6]/CuBTC samples; (a) 1800 and 400 ;(b) 3300 and 2800 cm^{-1}.

Previous studies showed that IL molecules are interacting directly with the open metal sites in CuBTC.[28,30,76] To understand the extent of interactions between [BMIM][PF_6] and its methylated counterpart ([BMMIM][PF_6]), we probed the Cu−O stretching frequency of the composites. Data showed that the band at 480 cm^{-1} (ν(Cu−O)) in CuBTC spectra was shifted to 475 cm^{-1} in [BMIM][PF_6]/CuBTC. However, in the methylated sample, [BMMIM][PF_6]/CuBTC, the corresponding peak shifts to 477 cm^{-1}. These red shifts indicate that the Cu−O bonding becomes weaker in the presence of IL consistent with previous studies.[30,63] However, the degree of this weakening in Cu−O bonding is different when the ILs are different. [BMIM][PF_6] is more strongly interacting with the open metal site and this results in a higher degree of red shift (5 cm^{-1}) in the Cu−O stretching frequency. On the other hand, the methylated IL ([BMMIM][PF_6]) has less interaction with Cu−O site compared to non-methylated IL (red shift of 3 cm^{-1}). This might be because of hydrogen bonding between the C2H in cation and framework oxygen atoms bonded to metal sites (Cu atoms). Moreover, it might be attributed to more dynamic behaviour of the cations and anions in non-methylated IL ([BMIM][PF_6]) compared to methylated counterpart ([BMMIM][PF_6]).[74] These differences in interactions between the IL molecules and the framework are expected to lead to changes in performance parameters.

6.2.6. Thermogravimetric Analysis of CuBTC and Composite Samples

TGA results are given in Figure 6.4 and Table 6.2 show that the bulk [BMMIM][PF_6] is more stable than its non-methylated counterpart. This result is consistent with previous studies.[69,72,86]

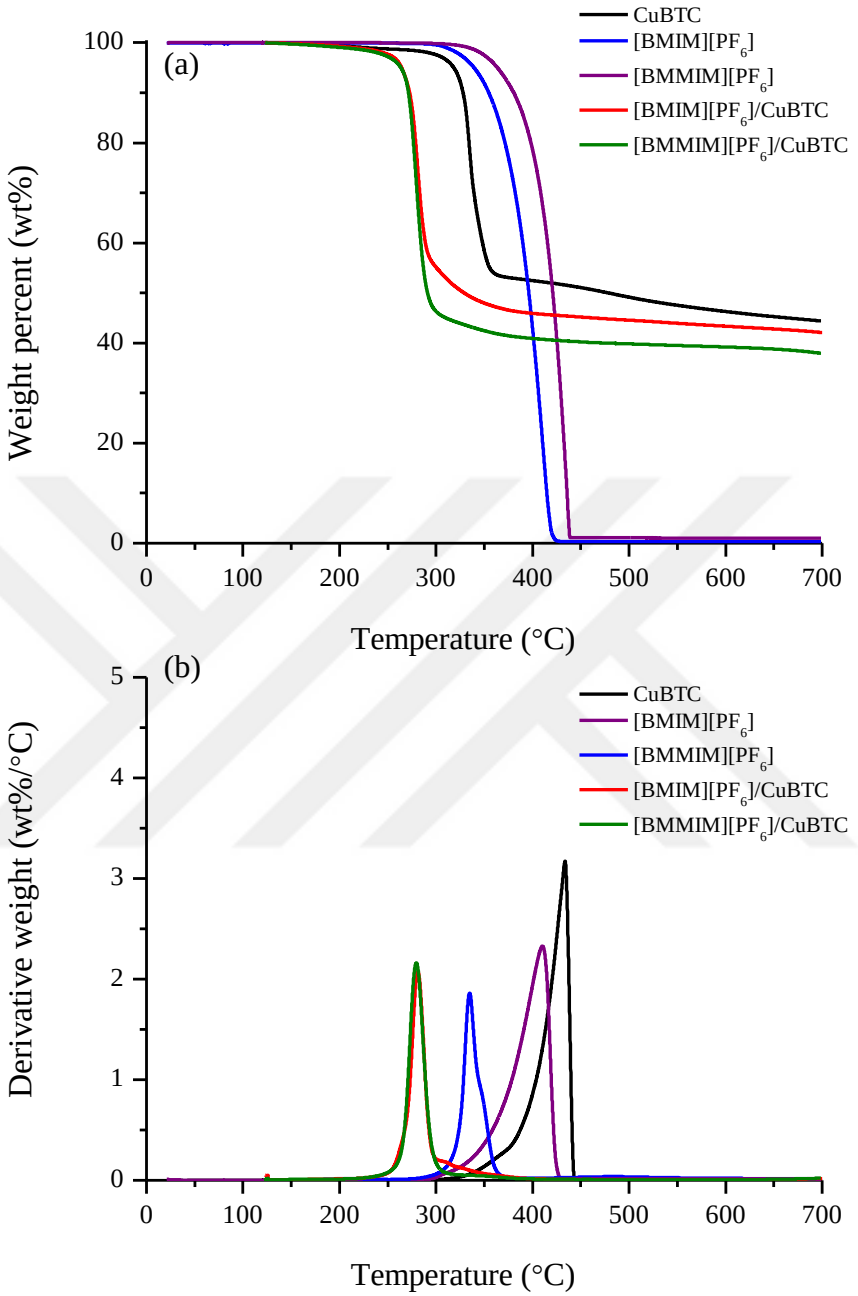

Figure 6.4. TGA results of CuBTC, [BMIM][PF_6], [BMMIM][PF_6], [BMIM][PF_6]/CuBTC and [BMMIM][PF_6]/CuBTC samples: (a) TG curves and (b) derivative TG curves.

Table 6.2. *T'onset* values of CuBTC, bulk ILs and IL incorporated CuBTC samples.

sample	T'_{onset} (°C)
CuBTC	324
[BMIM][PF_6]	298
[BMMIM][PF_6]	342
[BMIM][PF_6]/CuBTC	255
[BMMIM][PF_6]/CuBTC	262

For the incorporated samples, T'_{onset} values were 255 and 262 °C for [BMIM][PF_6]/CuBTC and [BMMIM][PF_6]/CuBTC, respectively. Recently, we showed that the interaction of ILs with open metal sites is a major parameter in determining the decomposition temperature. Accordingly, T'_{onset} presents an inverse relation with Cu−O band shift. Higher degree of red shifts in Cu−O band resulted in lower decomposition temperatures.[30] Here, we observed a very similar trend, [BMIM][PF_6]/CuBTC sample has a Cu−O red shift of 5 cm^{-1} and its T'_{onset} is 255 °C, while [BMMIM][PF_6]/CuBTC has a red shift of 3 cm^{-1} and it decomposes at 262 °C.

6.3. Gas Adsorption and Gas Separation Performance of [BMIM][PF_6]/CuBTC and [BMMIM][PF_6]/CuBTC samples

We investigated the consequences of these differences in interactions between the ILs and MOF on the gas adsorption and separation performance of IL/MOF composites as well. Accordingly, CO_2, CH_4, and N_2 gas adsorption experiments were performed on the pristine CuBTC and on [BMIM][PF_6]/CuBTC and [BMMIM][PF_6]/CuBTC composites. Figure 6.5 illustrates the isotherms obtained using Dual-Site-Langmuir model by fitting the experimental data.

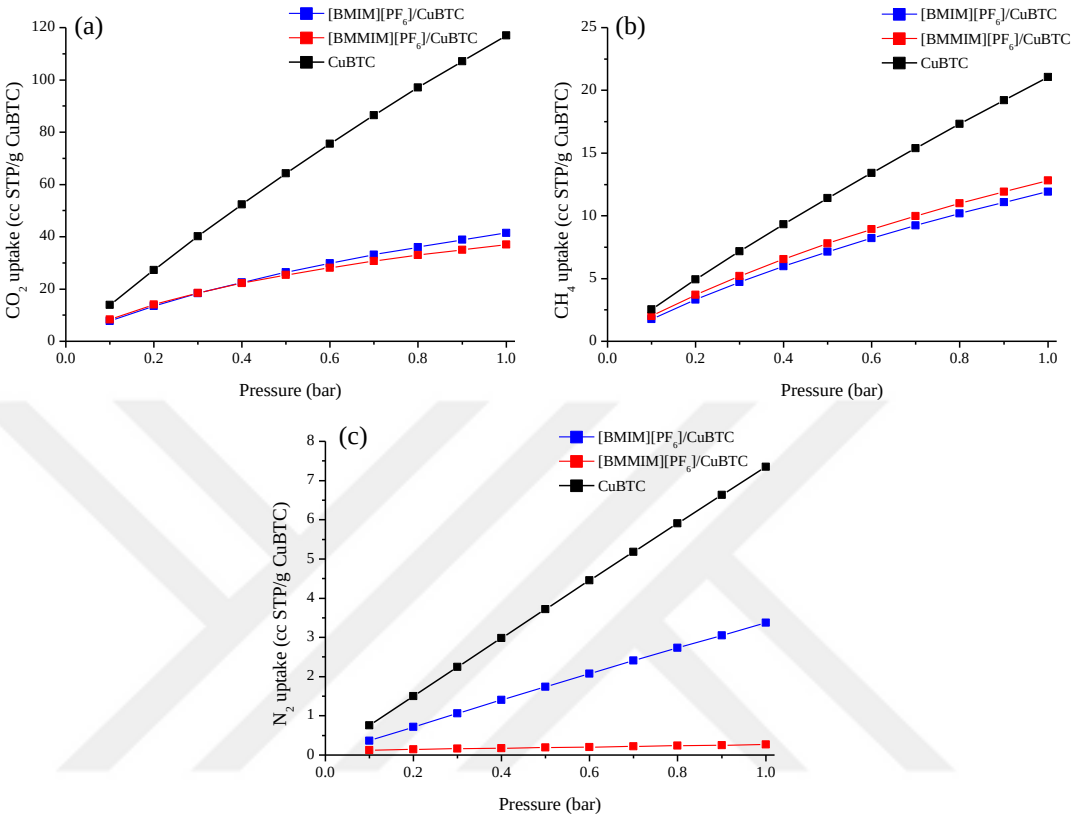

Figure 6.5. Isotherms for CuBTC, [BMIM][PF_6]/CuBTC and [BMMIM][PF_6]/CuBTC samples at 298 K; (a) CO_2, (b) CH_4 and (c) N_2.

Figure 6.5 shows that CO_2, CH_4, and N_2 uptakes in composite samples decreased compared to their corresponding values in parent CuBTC. However, the degree of this decrease in uptakes was not the same for CO_2, CH_4, and N_2. For an instance, the difference between CH_4 uptake of pristine CuBTC and composites are very low till 400 mbar, however, the difference in the N_2 uptakes of CuBTC and IL/MOF composites were higher. In composite uptakes [BMMIM][PF_6]/CuBTC has higher CO_2 (till 500 mbar), CH_4 and N_2 uptake compared to [BMIM][PF_6]/CuBTC. This difference is originating from the difference in interactions between [BMIM][PF_6] and [BMMIM][PF_6] with open

metal sites. Since [BMMIM][PF_6] has less interaction with the open metal site of CuBTC (probed by a lower degree of red shift in ν(Cu−O)), the electron density over open metal sites are more available for gas molecules. This result is consistent with our previous study in which we showed that strong interactions of ILs with open metal sites in CuBTC resulted in lower uptake values. [30] Furthermore, our Conductor-like Screening Model for Realistic Solvents (COSMO-RS)[87,88] calculations (Figure C.1) showed that CO_2, CH_4, and N_2 had higher solubilities in [BMMIM][PF_6] compared to non-methylated [BMIM][PF_6]. This difference in solubilities can be another reason for the differences in the degree of decrease in uptakes. We then investigated the separation performance of the composites. Figure 6.6(a) illustrates that at 1 mbar, [BMIM][PF_6]/CuBTC and [BMMIM][PF_6]/CuBTC composites showed approximately 39 and 13% improvements for CO_2/N_2 and CH_4/N_2 selectivities, respectively, compared to pristine CuBTC.

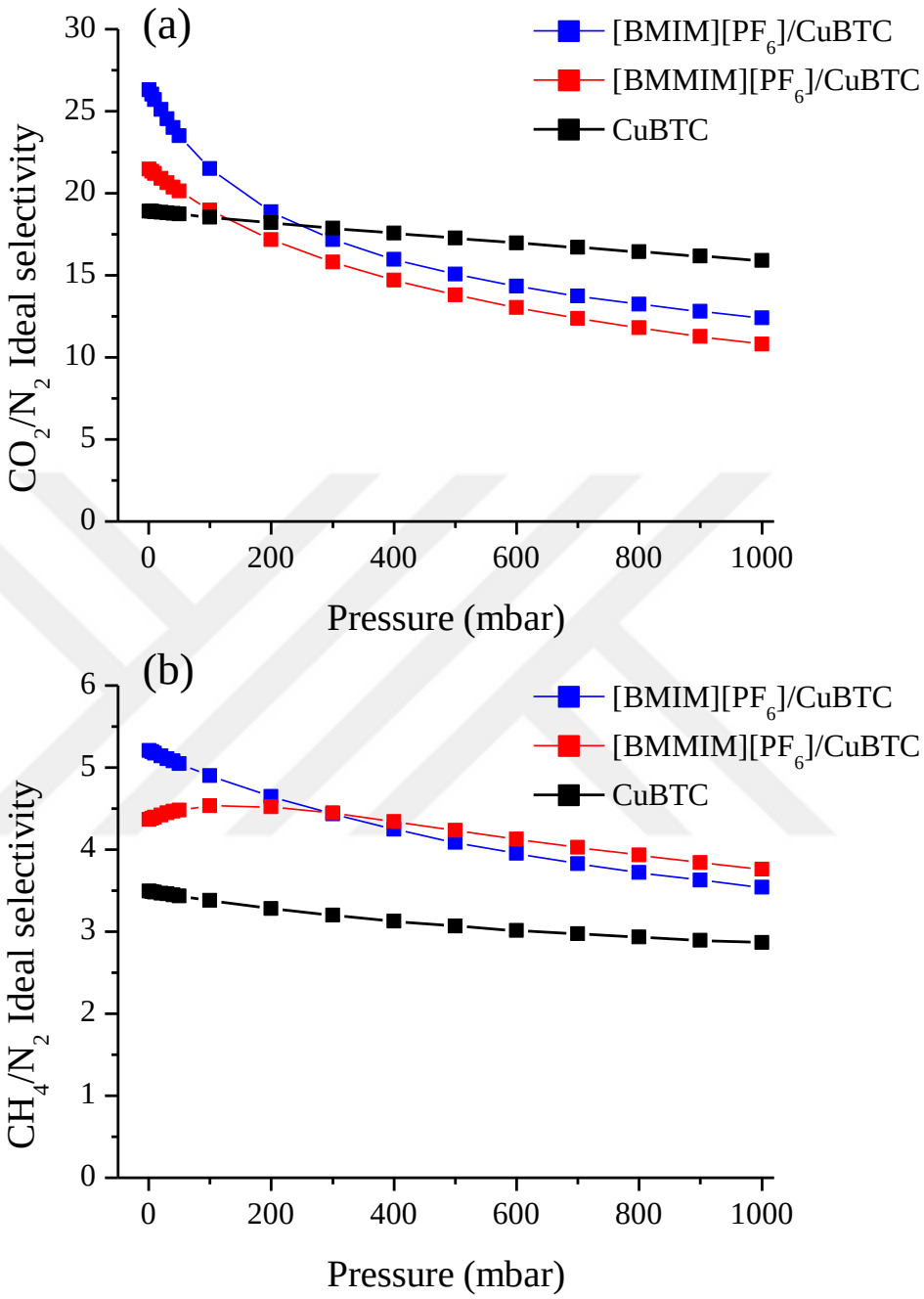

Figure 6.6. Ideal adsorption selectivities of CuBTC, [BMIM][PF_6]/CuBTC and [BMMIM][PF_6]/CuBTC at room temperature up to 1 bar; (a) CO_2/N_2 and (b) CH_4/N_2.

As the pressure increases, the free space becomes the dominant factor in adsorption and separation behaviour of an adsorbent. As a result, we observed that the selectivity is

decreasing at higher pressures. Higher CO_2/N_2 selectivity in [BMIM][PF_6]/CuBTC composite is mainly attributed to a higher CO_2/N_2 solubility ratio in [BMIM][PF_6] (Figure C2). For CH_4/N_2 selectivity, we observed improved selectivity performance for both composites in the whole pressure region. Accordingly, [BMIM][PF_6]/CuBTC showed 49% increment and [BMMIM][PF_6]/CuBTC sample showed 25% improvement compared to parent CuBTC at 1 mbar. In order to asses the gas separation performance of these composites in real gas mixtures, we used IAST to estimate the mixture selectivity of CuBTC, [BMIM][PF_6]/CuBTC and [BMMIM][PF_6]/CuBTC samples with CO_2/N_2:15/85 and CH_4/N_2:50/50 compositions.

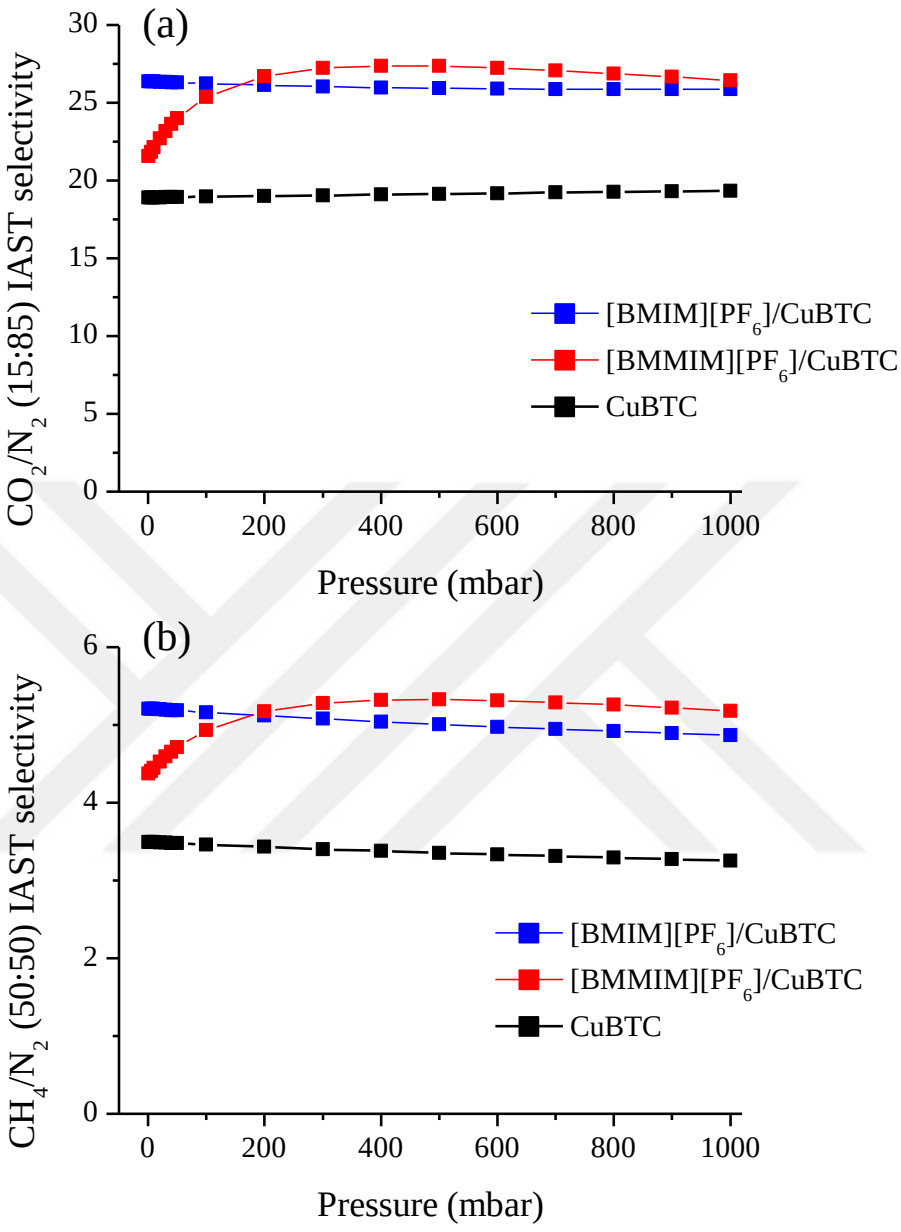

Figure 6.7. IAST mixture selectivity of CuBTC, [BMIM][PF_6]/CuBTC and [BMMIM][PF_6]/CuBTC samples for (a) CO_2/N_2 (15:85 mixture) and (b) CH_4/N_2 (50:50 mixture).

Figure 6.7 indicates that both composites show superior gas separation performance compared to pristine CuBTC in the whole pressure range. At very low pressures, for both CO_2/N_2 and CH_4/N_2, [BMIM][PF_6]/CuBTC sample showed higher selectivity values compared to corresponding values in [BMMIM][PF_6]/CuBTC. However, after 100 mbar, [BMMIM][PF_6]/CuBTC exhibits a better performance. This result might be because of weak interactions of gas molecules with the methylated IL molecules at low pressures as a result of more packed cations and anions.

Chapter 7: Conclusions and Outlook

In this study, some of the structural parameters affecting the interactions between ILs and MOFs were elucidated. In the first part, possible techniques (wet impregnation, ship-in-bottle, and incipient wetness) for the preparation of IL/MOF composites were investigated. Detailed characterization of the samples showed that wet impregnation method was efficient among other methods in terms of time and energy consumption and it enables the synthesis of any IL-MOF combinations.

In the second part of this thesis, one of the structural factors controlling the interactions between the ILs and MOF was investigated. CuBTC was selected as the MOF and a family of ILs with the same cation (imidazolium-based) and different anions were used. Synthesized composites were characterized using different techniques such as XRD, SEM, XRF, TGA, FTIR and BET surface area. Results showed that interionic interaction energy in bulk ILs (which can be probed spectroscopically via C2H infrared stretching frequency) is a major parameter in determining the interactions of ILs with MOFs. FTIR spectroscopy measurements revealed that the ILs are directly controlling the electronic environment over the unsaturated metal sites in MOF. Since the open metal sites in MOF act as the main adsorption sites for guest molecules (gases), by controlling the interaction of ILs with open metal sites, the adsorption performance, as well as the thermal stability limit of IL/MOF hybrids, can be tuned respectively.

In the last part, consequences of methylation in an imidazolium IL ([BMIM][PF_6]) on the interactions between IL and MOF (CuBTC) and their consequent effects on the gas separation performance are investigated. Results showed that modification of interionic interaction energy of an IL resulted in altering of the IL-MOF interactions. Spectroscopic analysis revealed that methylated IL interacts weakly with open metal sites of the MOF compared to non-methylated IL. Gas adsorption measurements showed that methylation changed the decrease in degree of uptakes in composite sample. This effect

resulted in a remarkable increase in CO_2/N_2 and CH_4/N_2 selectivity of methylated IL incorporated sample compared to pristine MOF and non-methylated IL/MOF composite.

In conclusion, tunability of structures in ILs and MOFs offers a very broad potential in different areas, especially in adsorption-based gas separation. In this field, ILs introduce further adsorption sites for guest molecules and at the same time hinders the adsorption of other molecules. Therefore, large-scale screening of the ILs for different gas mixtures would be helpful for improving the separation performance of parent MOFs. Computational screening of IL/MOF composites can help to design a better composite in terms of performance for different separation applications. Incorporation of metal-containing ILs in different MOFs might be one way to enhance the storage capacities of pristine MOFs since some gases have an affinity toward specific metal atoms. Application of IL/MOF composites in large-scale applications needs to be investigated. In this case, water stability of IL/MOF composites can be addressed by using the composite samples in the presence of water molecules. Dynamic adsorption experiments can be performed to evaluate the breakthrough analysis and dynamic separation performance of the IL/MOF composites. One of the very recent application of MOFs is water harvesting from the atmosphere. To improve the yield of this process, different hydrophilic ILs can be used to improve the water capture of parent MOFs. Cryogenic energy storage is one of the recent approaches in addressing the storage of energy for future applications. For an instance, storage of hydrogen in very low temperatures. IL/MOF composites can be examined in the storage of hydrogen or other gases in very low temperatures. Same approach in this thesis can be applied to other MOFs to further understand the structure-interaction-performance relationship in IL/MOF composites.

BIBLIOGRAPHY

(1) Mason, J. A.; Veenstra, M.; Long, J. R. Evaluating Metal–organic Frameworks for Natural Gas Storage. *Chem. Sci.* **2014**, *5* (1), 32–51.

(2) Kampa, M.; Castanas, E. Human Health Effects of Air Pollution. *Environ. Pollut.* **2008**, *151* (2), 362–367.

(3) Ralph T. Yang. *Gas Separation by Adsorption Processes*; 1987.

(4) Lu, C.; Bai, H.; Wu, B.; Su, F.; Hwang, J. F. Comparative Study of CO_2 Capture by Carbon Nanotubes, Activated Carbons, and Zeolites. *Energy & Fuels* **2008**, *22* (5), 3050–3056.

(5) Drage, T. C.; Blackman, J. M.; Pevida, C.; Snape, C. E. Evaluation of Activated Carbon Adsorbents for CO_2 Capture in Gasification. *Energy & Fuels* **2009**, *23* (5), 2790–2796.

(6) Samanta, A.; Zhao, A.; Shimizu, G. K. H.; Sarkar, P.; Gupta, R. Post-Combustion CO_2 Capture Using Solid Sorbents: A Review. *Ind. Eng. Chem. Res.* **2012**, *51* (4), 1438–1463.

(7) Krishna, R.; Van Baten, J. M. A Comparison of the CO_2 capture Characteristics of Zeolites and Metal-Organic Frameworks. *Sep. Purif. Technol.* **2012**, *87*, 120–126.

(8) Li, J. R.; Ma, Y.; McCarthy, M. C.; Sculley, J.; Yu, J.; Jeong, H. K.; Balbuena, P. B.; Zhou, H. C. Carbon Dioxide Capture-Related Gas Adsorption and Separation in Metal-Organic Frameworks. *Coord. Chem. Rev.* **2011**, *255* (15–16), 1791–1823.

(9) Sumida, K.; Rogow, D. L.; Mason, J. A.; McDonald, T. M.; Bloch, E. D.; Herm, Z. R.; Bae, T. H.; Long, J. R. Carbon Dioxide Capture in Metal-Organic Frameworks. *Chem. Rev.* **2012**, *112* (2), 724–781.

(10) Zhou, H. C.; Long, J. R.; Yaghi, O. M. Introduction to Metal-Organic Frameworks. *Chem. Rev.* **2012**, *112* (2), 673–674.

(11) Lee, J.; Farha, O. K.; Roberts, J.; Scheidt, K. A.; Nguyen, S. T.; Hupp, J. T. Metal–organic Framework Materials as Catalysts. *Chem. Soc. Rev.* **2009**, *38* (5), 1450.

(12) Horcajada, P.; Serre, C.; Vallet-regí, M.; Sebban, M.; Taulelle, F.; Førey, G. Metal–Organic Frameworks as Efficient Materials for Drug Delivery. *Angew. Chemie - Int. Ed.* **2006**, 6120–6124.

(13) Hendon, C. H.; Tiana, D.; Walsh, A. Conductive Metal–organic Frameworks and Networks: Fact or Fantasy? *Phys. Chem. Chem. Phys.* **2012**, *14* (38), 13120.

(14) Kreno, L. E.; Leong, K.; Farha, O. K.; Allendorf, M.; Van Duyne, R. P.; Hupp, J. T. Metal-Organic Framework Materials as Chemical Sensors. *Chem. Rev.* **2012**, *112* (2), 1105–1125.

(15) Wang, Z.; Cohen, S. M. Postsynthetic Modification of Metal–organic Frameworks.

Chem. Soc. Rev. **2009**, *38* (5), 1315.

(16) Wang, Z.; Cohen, S. M. Postsynthetic Covalent Modification of a Neutral Metal-Organic Framework. *J. Am. Chem. Soc.* **2007**, *129* (41), 12368–12369.

(17) Kim, M.; Cahill, J. F.; Fei, H.; Prather, K. A.; Cohen, S. M. Postsynthetic Ligand and Cation Exchange in Robust Metal-Organic Frameworks. *J. Am. Chem. Soc.* **2012**, *134* (43), 18082–18088.

(18) Sezginel, K. B.; Keskin, S.; Uzun, A. Tuning the Gas Separation Performance of CuBTC by Ionic Liquid Incorporation. *Langmuir* **2016**, *32* (4), 1139–1147.

(19) Kinik, F. P.; Altintas, C.; Balci, V.; Koyuturk, B.; Uzun, A.; Keskin, S. [BMIM][PF_6] Incorporation Doubles CO_2 Selectivity of ZIF-8: Elucidation of Interactions and Their Consequences on Performance. *ACS Appl. Mater. Interfaces* **2016**, *8* (45), 30992–31005.

(20) Koyuturk, B.; Altintas, C.; Kinik, F. P.; Keskin, S.; Uzun, A. Improving Gas Separation Performance of ZIF-8 by [BMIM][BF_4] Incorporation: Interactions and Their Consequences on Performance. *J. Phys. Chem. C* **2017**, acs.jpcc.7b00848.

(21) Welton, T. Room-Temperature Ionic Liquids. Solvents for Synthesis and Catalysis. *Chem. Rev.* **1999**, *99* (8), 2071–2084.

(22) Rogers, R. D.; Seddon, K. R. 2003_Seddon_Ionic_Liquids_Solvents_of_the_future. *Science (80).* **2003**, *302*.

(23) Zhang, S.; Sun, N.; He, X.; Lu, X.; Zhang, X. Physical Properties of Ionic Liquids: Database and Evaluation. *J. Phys. Chem. Ref. Data* **2006**, *35* (4), 1475–1517.

(24) Huddleston, J. G. J. G.; Willauer, H. D.; Swatloski, R. P.; Visser, A. E.; Rogers, R. D. R. D. Room Temperature Ionic Liquids as Novel Media for " Clean " Liquid – Liquid Extraction. *Chem. Commun.* **1998**, No. 16, 1765–1766.

(25) Olivier-Bourbigou, H.; Magna, L.; Morvan, D. Ionic Liquids and Catalysis: Recent Progress from Knowledge to Applications. *Appl. Catal. A Gen.* **2010**, *373* (1–2), 1–56.

(26) TangVisiting Ph.D. student to the U, J.; Tang, H.; Sun, W.; Plancher, H.; Radosz, M.; Shen, Y. Poly(ionic Liquid)s: A New Material with Enhanced and Fast CO_2 Absorption. *Chem. Commun.* **2005**, No. 26, 3325.

(27) Chui, S. S. Y.; Lo, S. M. F.; Charmant, J. P. H.; Orpen, a G.; Williams, I. D. A Chemically Functionalizable Nanoporous Material $[Cu_3(TMA)_2(H_2O)_3]_n$. *Science (80-.).* **1999**, *283* (February), 1148–1150.

(28) Karra, J. R.; Walton, K. S. Effect of Open Metal Sites on Adsorption of Polar and Nonpolar Molecules in Metal-Organic Framework Cu-BTC. *Langmuir* **2008**, *24* (16), 8620–8626.

(29) Chowdhury, P.; Mekala, S.; Dreisbach, F.; Gumma, S. Adsorption of CO, CO_2 and CH_4 on Cu-BTC and MIL-101 Metal Organic Frameworks: Effect of Open Metal Sites and Adsorbate Polarity. *Microporous Mesoporous Mater.* **2012**, *152*, 246–252.

(30) Nozari, V.; Keskin, S.; Uzun, A. Toward Rational Design of Ionic Liquid/Metal–Organic Framework Composites: Effects of Interionic Interaction Energy. *ACS Omega* **2017**, *2* (10), 6613–6618.

(31) Zhang, Z.; Zhao, Y.; Gong, Q.; Li, Z.; Li, J. MOFs for CO_2 Capture and Separation from Flue Gas Mixtures: The Effect of Multifunctional Sites on Their Adsorption Capacity and Selectivity. *Chem. Commun.* **2013**, *49* (7), 653–661.

(32) Cohen, S. M. Postsynthetic Methods for the Functionalization of Metal-Organic Frameworks. *Chem. Rev.* **2012**, *112* (2), 970–1000.

(33) Meilikhov, M.; Yusenko, K.; Esken, D.; Turner, S.; Van Tendeloo, G.; Fischer, R. A. Metals@MOFs - Loading MOFs with Metal Nanoparticles for Hybrid Functions. *Eur. J. Inorg. Chem.* **2010**, No. 24, 3701–3714.

(34) Calleja, G.; Botas, J. A.; Sánchez-Sánchez, M.; Orcajo, M. G. Hydrogen Adsorption over Zeolite-like MOF Materials Modified by Ion Exchange. *Int. J. Hydrogen Energy* **2010**, *35* (18), 9916–9923.

(35) Kinik, F. P.; Uzun, A.; Keskin, S. Ionic Liquid/Metal–Organic Framework Composites: From Synthesis to Applications. *ChemSusChem* **2017**, *10* (14), 2842–2863.

(36) Cota, I.; Fernandez Martinez, F. Recent Advances in the Synthesis and Applications of Metal Organic Frameworks Doped with Ionic Liquids for CO_2 adsorption. *Coord. Chem. Rev.* **2017**, *351*, 189–204.

(37) Aijaz, A.; Akita, T.; Yang, H.; Xu, Q. From Ionic-Liquid@metal–organic Framework Composites to Heteroatom-Decorated Large-Surface Area Carbons: Superior CO_2 and H_2 Uptake. *Chem. Commun.* **2014**, *50* (49), 6498.

(38) Khan, N. A.; Hasan, Z.; Jhung, S. H. Ionic Liquids Supported on Metal-Organic Frameworks: Remarkable Adsorbents for Adsorptive Desulfurization. *Chem. - A Eur. J.* **2014**, *20* (2), 376–380.

(39) Silva, F. W. M. da; Magalhães, G. M.; Jardim, E. O.; Silvestre-Albero, J.; Sepúlveda-Escribano, A.; de Azevedo, D. C. S.; de Lucena, S. M. P. CO_2 Adsorption on Ionic Liquid—Modified Cu-BTC: Experimental and Simulation Study. *Adsorpt. Sci. Technol.* **2015**, *33* (2), 223–242.

(40) Ban, Y.; Li, Z.; Li, Y.; Peng, Y.; Jin, H.; Jiao, W.; Guo, A.; Wang, P.; Yang, Q.; Zhong, C.; et al. Confinement of Ionic Liquids in Nanocages: Tailoring the Molecular Sieving Properties of ZIF-8 for Membrane-Based CO_2 Capture. *Angew. Chemie - Int. Ed.* **2015**, *54* (51), 15483–15487.

(41) Ma, J.; Ying, Y.; Guo, X.; Huang, H.; Liu, D.; Zhong, C. Fabrication of Mixed-Matrix Membrane Containing Metal–organic Framework Composite with Task-Specific Ionic Liquid for Efficient CO_2 Separation. *J. Mater. Chem. A* **2016**, *4* (19), 7281–7288.

(42) Mohamedali, M.; Ibrahim, H.; Henni, A. Incorporation of Acetate-Based Ionic Liquids into a Zeolitic Imidazolate Framework (ZIF-8) as Efficient Sorbents for Carbon Dioxide Capture. *Chem. Eng. J.* **2018**, *334* (August 2017), 817–828.

(43) Jiawei Wang, Danyan Xie, Zhiguo Zhang, Qiwei Yang, Huabin Xing, Yiwen Yang,Qilong Ren, and Z. B. Efficient Adsorption Separation of Acetylene and Ethylen E viaSupported Ionic Liquid on Metal-Organic Framework. *AIChe J* **2017**, *63* (504), 2165–2175.

(44) Lin, Z.; Wragg, D. S.; Morris, R. E. Microwave-Assisted Synthesis of Anionic Metal–organic Frameworks under Ionothermal Conditions. *Chem. Commun.* **2006**, *4* (19), 2021–2023.

(45) Ma, Z.; Yu, J.; Dai, S. Preparation of Inorganic Materials Using Ionic Liquids. *Adv. Mater.* **2010**, *22* (2), 261–285.

(46) Fujie, K.; Otsubo, K.; Ikeda, R.; Yamada, T.; Kitagawa, H. Low Temperature Ionic Conductor: Ionic Liquid Incorporated within a Metal–organic Framework. *Chem. Sci.* **2015**, *6* (7), 4306–4310.

(47) Sun, X. L.; Deng, W. H.; Chen, H.; Han, H. L.; Taylor, J. M.; Wan, C. Q.; Xu, G. A Metal–Organic Framework Impregnated with a Binary Ionic Liquid for Safe Proton Conduction above 100 C. *Chem. - A Eur. J.* **2017**, *23* (6), 1248–1252.

(48) Khan, N. A.; Hasan, Z.; Jhung, S. H. Ionic liquid@MIL-101 Prepared via the Ship-in-Bottle Technique: Remarkable Adsorbents for the Removal of Benzothiophene from Liquid Fuel. *Chem. Commun.* **2016**, *52* (12), 2561–2564.

(49) Tharun, J.; Bhin, K.-M.; Roshan, R.; Kim, D. W.; Kathalikkattil, A. C.; Babu, R.; Ahn, H. Y.; Won, Y. S.; Park, D.-W. Ionic Liquid Tethered Post Functionalized ZIF-90 Framework for the Cycloaddition of Propylene Oxide and CO_2. *Green Chem.* **2016**, *18* (8), 2479–2487.

(50) Luo, Q. X.; Song, X. D.; Ji, M.; Park, S. E.; Hao, C.; Li, Y. Q. Molecular Size- and Shape-Selective Knoevenagel Condensation over Microporous $Cu_3(BTC)_2$ Immobilized Amino-Functionalized Basic Ionic Liquid Catalyst. *Appl. Catal. A Gen.* **2014**, *478*, 81–90.

(51) Wu, J.; Gao, Y.; Zhang, W.; Tan, Y.; Tang, A.; Men, Y.; Tang, B. Deep Desulfurization by Oxidation Using an Active Ionic Liquid-Supported Zr Metal-Organic Framework as Catalyst. *Appl. Organomet. Chem.* **2015**, *29* (2), 96–100.

(52) Abednatanzi, S.; Abbasi, A.; Masteri-Farahani, M. Immobilization of Catalytically Active Polyoxotungstate into Ionic Liquid-Modified MIL-100(Fe): A Recyclable Catalyst for Selective Oxidation of Benzyl Alcohol. *Catal. Commun.* **2017**, *96*, 6–10.

(53) Han, M.; Gu, Z.; Chen, C.; Wu, Z.; Que, Y.; Wang, Q.; Wan, H.; Guan, G. Efficient Confinement of Ionic Liquids in MIL-100(Fe) Frameworks by the "impregnation-Reaction-Encapsulation" Strategy for Biodiesel Production. *RSC Adv.* **2016**, *6* (43), 37110–37117.

(54) Gupta, K. M.; Chen, Y.; Jiang, J. Ionic Liquid Membranes Supported by Hydrophobic and Hydrophilic Metal-Organic Frameworks for CO_2 Capture. *J. Phys. Chem. C* **2013**, *117* (11), 5792–5799.

(55) Tshibangu, P. N.; Ndwandwe, S. N.; Dikio, E. D. Density , Viscosity and Conductivity Study of 1-Butyl-3- Methylimidazolium Bromide. *Int. J. Electrochem. Sci* **2011**, *6* (June 2011), 2201–2213.

(56) Dharaskar, S. A.; Wasewar, K. L.; Varma, M. N.; Shende, D. Z.; Yoo, C. K. Synthesis, Characterization and Application of 1-Butyl-3-Methylimidazolium Tetrafluoroborate for Extractive Desulfurization of Liquid Fuel. *Arab. J. Chem.* **2016**, *9* (4), 578–587.

(57) Khan, N. A.; Bhadra, B. N.; Jhung, S. H. Heteropoly Acid-Loaded Ionic Liquid@metal-Organic Frameworks: Effective and Reusable Adsorbents for the Desulfurization of a Liquid Model Fuel. *Chem. Eng. J.* **2018**, *334* (November 2017), 2215–2221.

(58) Yu, Y.; Mai, J.; Wang, L.; Li, X.; Jiang, Z.; Wang, F. Ship-in-a-Bottle Synthesis of Amine-Functionalized Ionic Liquids in NaY Zeolite for CO_2 Capture. *Sci. Rep.* **2014**, *4*, 1–8.

(59) Wojdyr, M. Fityk: A General-Purpose Peak Fitting Program. *J. Appl. Crystallogr.* **2010**, *43* (5 PART 1), 1126–1128.

(60) HPVA-II-High-Pressure-Volumetric-Analyzer. HPVA-II-High-Pressure-Volumetric-Analyzer @ Particulatesystems.com. 2016.

(61) Lee, S.; Lee, J. H.; Kim, J. User-Friendly Graphical User Interface Software for Ideal Adsorbed Solution Theory Calculations. *Korean J. Chem. Eng.* **2018**, *35* (1), 214–221.

(62) Yu, Y.; Mai, J.; Huang, L.; Wang, L.; Li, X. Ship in a Bottle Synthesis of Ionic Liquids in NaY Supercages for CO_2 Capture. *RSC Adv.* **2014**, *4* (25), 12756.

(63) Dhumal, N. R.; Singh, M. P.; Anderson, J. A.; Johannes, K.; Kim, H. J. Molecular Interactions of a Cu-Based Metal Organic Framework with a Confined Imidazolium-Based Ionic Liquid: A Combined Density-Functional Theory and Experimental Vibrational Spectroscopy Study. *J Phys Chem C* **2016**, *120*, 3295–3304.

(64) Ma, J.; Ying, Y.; Guo, X.; Huang, H.; Liu, D.; Zhong, C. Fabrication of Mixed-Matrix Membrane Containing Selective and Facilitated CO_2 Transport Metal-Organic Framework Composite with Task-Specific Ionic Liquid for Efficient CO_2 Separation. *J. Mater. Chem. A* **2016**, *0*, 1–8.

(65) Xue, W.; Li, Z.; Huang, H.; Yang, Q.; Liu, D.; Xu, Q.; Zhong, C. Effects of Ionic Liquid Dispersion in Metal-Organic Frameworks and Covalent Organic Frameworks on CO_2 Capture: A Computational Study. *Chem. Eng. Sci.* **2016**, *140*, 1–9.

(66) Chen, Y.; Hu, Z.; Gupta, K. M.; Jiang, J. Ionic Liquid/metal-Organic Framework Composite for CO_2 Capture: A Computational Investigation. *J. Phys. Chem. C* **2011**, *115* (44), 21736–21742.

(67) Babucci, M.; Uzun, A. Effects of Interionic Interactions in 1,3-Dialkylimidazolium Ionic Liquids on the Electronic Structure of Metal Sites in Solid Catalysts with Ionic Liquid Layer (SCILL). *J. Mol. Liq.* **2016**, *216*, 293–297.

(68) Babucci, M.; Fang, C.-Y.; Hoffman, A. S.; Bare, S. R.; Gates, B. C.; Uzun, A. Tuning

the Selectivity of Single-Site Supported Metal Catalysts with Ionic Liquids. **2017**, 21–24.

(69) Babucci, M.; Akçay, A.; Balci, V.; Uzun, A. Thermal Stability Limits of Imidazolium Ionic Liquids Immobilized on Metal-Oxides. *Langmuir* **2015**, *31* (33), 9163–9176.

(70) Akçay, A.; Babucci, M.; Balci, V.; Uzun, A. A Model to Predict Maximum Tolerable Temperatures of Metal-Oxide-Supported 1-N-Butyl-3-Methylimidazolium Based Ionic Liquids. *Chem. Eng. Sci.* **2015**, *123*, 588–595.

(71) Akçay, A.; Balci, V.; Uzun, A. Structural Factors Controlling Thermal Stability of Imidazolium Ionic Liquids with 1-N-Butyl-3-Methylimidazolium Cation on -Al_2O_3. *Thermochim. Acta* **2014**, *589*, 131–136.

(72) Noack, K.; Schulz, P. S.; Paape, N.; Kiefer, J. The Role of the C2 Position in Interionic Interactions of Imidazolium Based Ionic Liquids : A Vibrational and NMR Spectroscopic Study. *Phys. Chem. Chem. Phys* **2010**, 14153–14161.

(73) Fumino, K.; Wulf, A.; Ludwig, R. The Cation-Anion Interaction in Ionic Liquids Probed by Far-Infrared Spectroscopy. *Angew. Chemie - Int. Ed.* **2008**, *47* (20), 3830–3834.

(74) Fumino, K.; Wulf, A.; Ludwig, R. Strong , Localized , and Directional Hydrogen Bonds Fluidize Ionic Liquids. **2008**, *2* (2), 8731–8734.

(75) Wulf, A.; Fumino, K.; Ludwig, R. Spectroscopic Evidence for an Enhanced Anion-Cation Interaction from Hydrogen Bonding in Pure Imidazolium Ionic Liquids. *Angew. Chemie - Int. Ed.* **2010**, *49* (2), 449–453.

(76) Dietzel, P. D. C.; Besikiotis, V.; Blom, R. Application of Metal–organic Frameworks with Coordinatively Unsaturated Metal Sites in Storage and Separation of Methane and Carbon Dioxide. *J. Mater. Chem.* **2009**, *19* (39), 7362.

(77) Materials Studio v8.0; Biovia Software Inc. Materials Studio Manual. Biovia Software Inc 2007.

(78) Gupta, K. M.; Chen, Y.; Hu, Z.; Jiang, J. Metal-Organic Framework Supported Ionic Liquid Membranes for CO_2 Capture: Anion Effects. *Phys. Chem. Chem. Phys.* **2012**, *14* (16), 5785–5794.

(79) Luo, Q. X.; Ji, M.; Lu, M. H.; Hao, C.; Qiu, J. S.; Li, Y. Q. Organic Electron-Rich N-Heterocyclic Compound as a Chemical Bridge: Building a Bronsted Acidic Ionic Liquid Confined in MIL-101 Nanocages. *J. Mater. Chem. A* **2013**, *1* (207890), 6530–6534.

(80) Chen, L.-H.; Wu, B.-B.; Zhao, H.-X.; Long, L.-S.; Zheng, L.-S. High Temperature Ionic Conduction Mediated by Ionic Liquid Incorporated within the Metal-Organic Framework UiO-67(Zr). *Inorg. Chem. Commun.* **2017**, *81*, 1–4.

(81) Uzun, A.; Keskin, S. Site Characteristics in Metal Organic Frameworks for Gas Adsorption. *Prog. Surf. Sci.* **2014**, *89* (1), 56–79.

(82) Hulteen, J. C.; Jirage, K. B.; Martin, C. R. Introducing Chemical Transport Selectivity into Gold Nanotubule Membranes. *J. Am. Chem. Soc.* **1998**, *120* (26), 6603–6604.

(83) Huddleston, J. G.; Visser, A. E.; Reichert, W. M.; Willauer, H. D.; Broker, G. a.; Rogers, R. D. Characterization and Comparison of Hydrophilic and Hydrophobic Room Temperature Ionic Liquids Incorporating the Imidazolium Cation. *Green Chem.* **2001**, *3* (4), 156–164.

(84) Van Der Bruggen, B.; Schaep, J.; Wilms, D.; Vandecasteele, C. Influence of Molecular Size, Polarity and Charge on the Retention of Organic Molecules by Nanofiltration. *J. Memb. Sci.* **1999**, *156* (1), 29–41.

(85) Torkkeli, A. Droplet Microfluidics on a Planar Surface. *VTT Publ.* **2003**, *54* (504), 3–194.

(86) Babucci, M.; Balci, V.; Akçay, A.; Uzun, A. Interactions of [BMIM][BF_4] with Metal Oxides and Their Consequences on Stability Limits. *J. Phys. Chem. C* **2016**, *120* (36), 20089–20102.

(87) Palomar, J.; Ferro, V. R.; Torrecilla, J. S.; Rodriguez, F. Density and Molar Volume Predictions Using COSMO-RS for Ionic Liquids. An Approach to Solvent Design. *Ind. Eng. Chem. Res.* **2007**, *46* (18), 6041–6048.

(88) Anantharaj, R.; Banerjee, T. COSMO-RS-Based Screening of Ionic Liquids as Green Solvents in Denitrification Studies. *Ind. Eng. Chem. Res.* **2010**, *49* (18), 8705–8725.

(89) Bae, Y. S.; Snurr, R. Q. Development and Evaluation of Porous Materials for Carbon Dioxide Separation and Capture. *Angew. Chemie - Int. Ed.* **2011**, *50* (49), 11586–11596.

(90) Chung, Y. G.; Camp, J.; Haranczyk, M.; Sikora, B. J.; Bury, W.; Krungleviciute, V.; Yildirim, T.; Farha, O. K.; Sholl, D. S.; Snurr, R. Q. Computation-Ready, Experimental Metal-Organic Frameworks: A Tool to Enable High-Throughput Screening of Nanoporous Crystals. *Chem. Mater.* **2014**, *26* (21), 6185–6192.

APPENDIX A: Supporting Information on Characterization of Chapter 5[1]

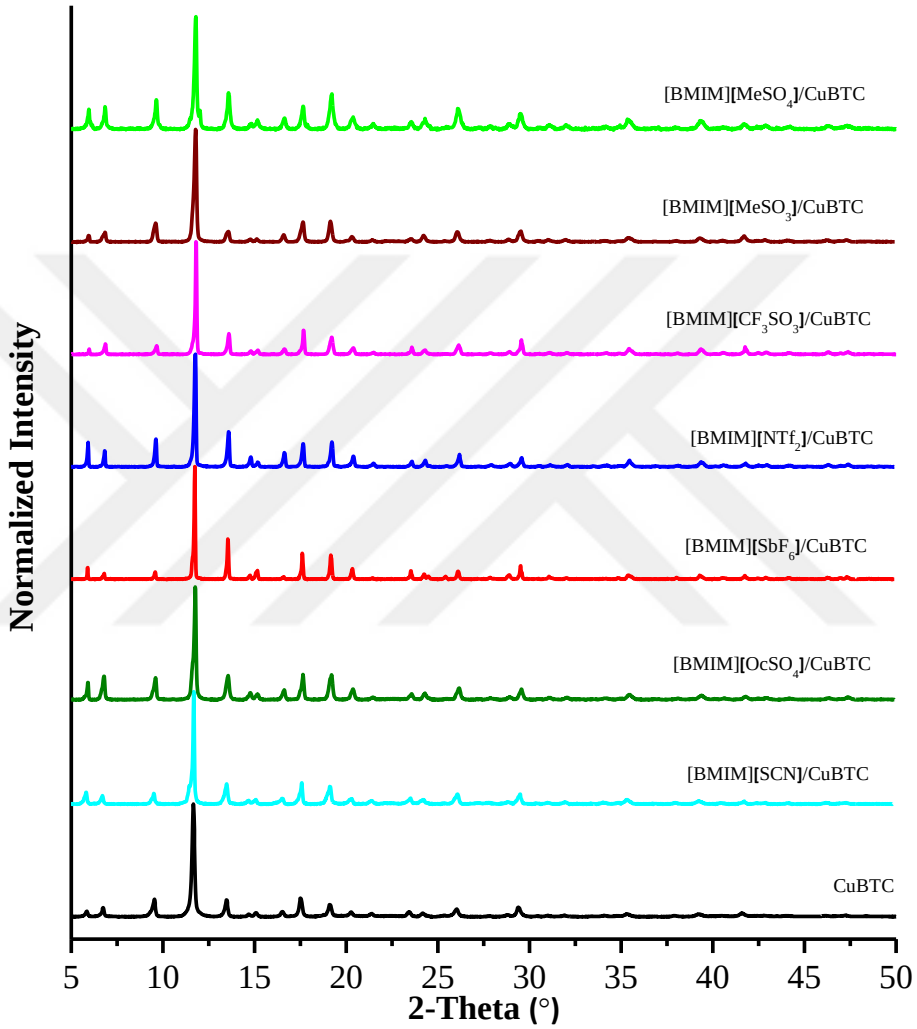

[1] The information in this appendix were published in *ACS Omega* as the Supporting Information with the following reference: Nozari, V.; Keskin, S.; Uzun, A. Toward Rational Design of Ionic Liquid/Metal–Organic Framework Composites: Effects of Interionic Interaction Energy. *ACS Omega* **2017**, *2* (10), 6613–6618.

Figure A.1. XRD patterns of CuBTC and IL/CuBTC samples.

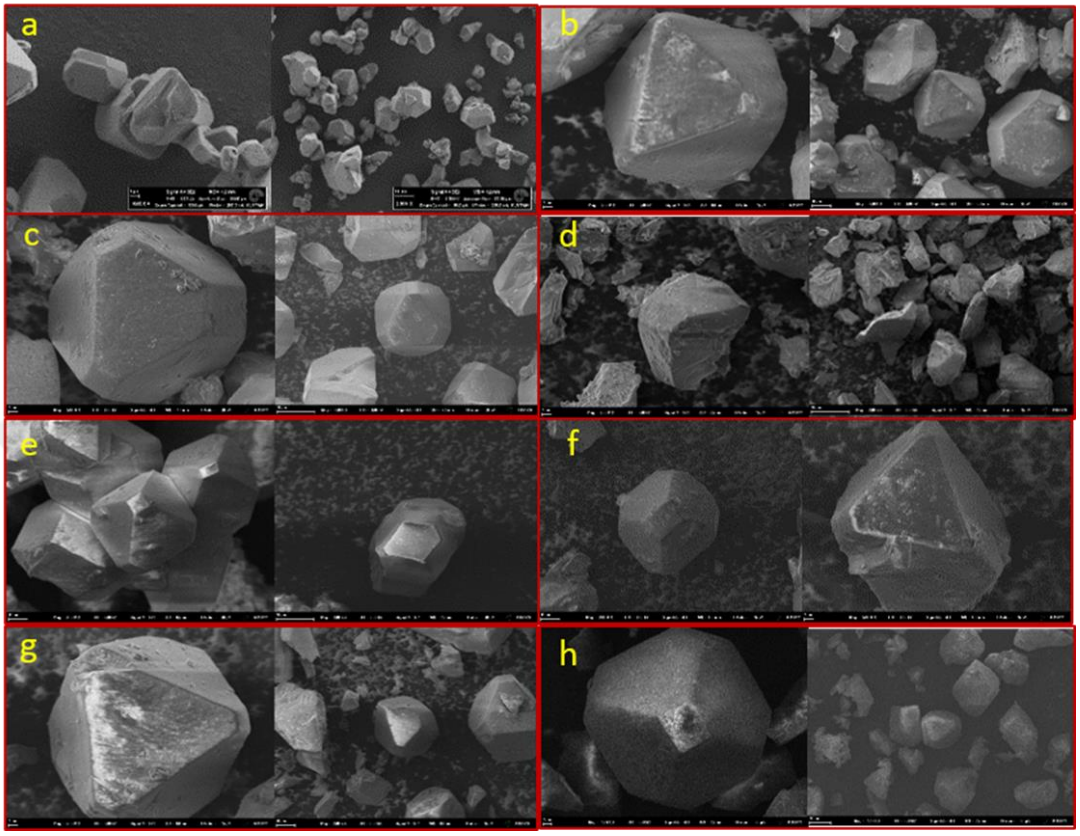

Figure A.2. SEM images: (a) CuBTC (b) [BMIM][$MeSO_3$]/CuBTC; (c) [BMIM][$MeSO_4$]/CuBTC; (d) [BMIM][CF_3SO_3]/CuBTC; (e) [BMIM][NTf_2]/CuBTC; (f) [BMIM][$OcSO_4$]/CuBTC; (g) [BMIM][SbF_6]/CuBTC; (h) [BMIM][SCN]/CuBTC.

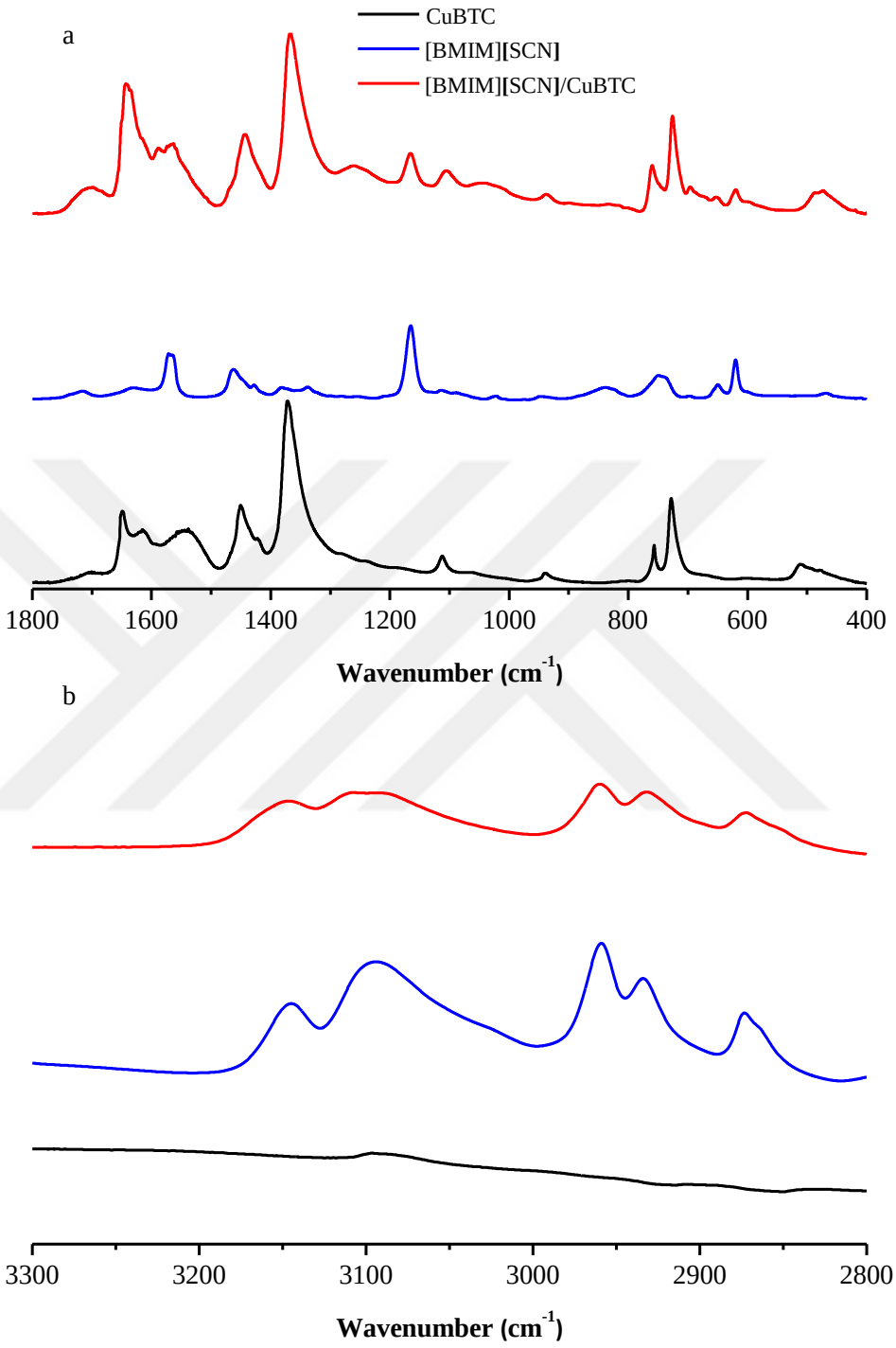

Figure A.3. FTIR spectra of [BMIM][SCN], CuBTC and [BMIM][SCN]/CuBTC in the region of (a) 400-1800 cm^{-1} and (b) 2800-3300 cm^{-1}.

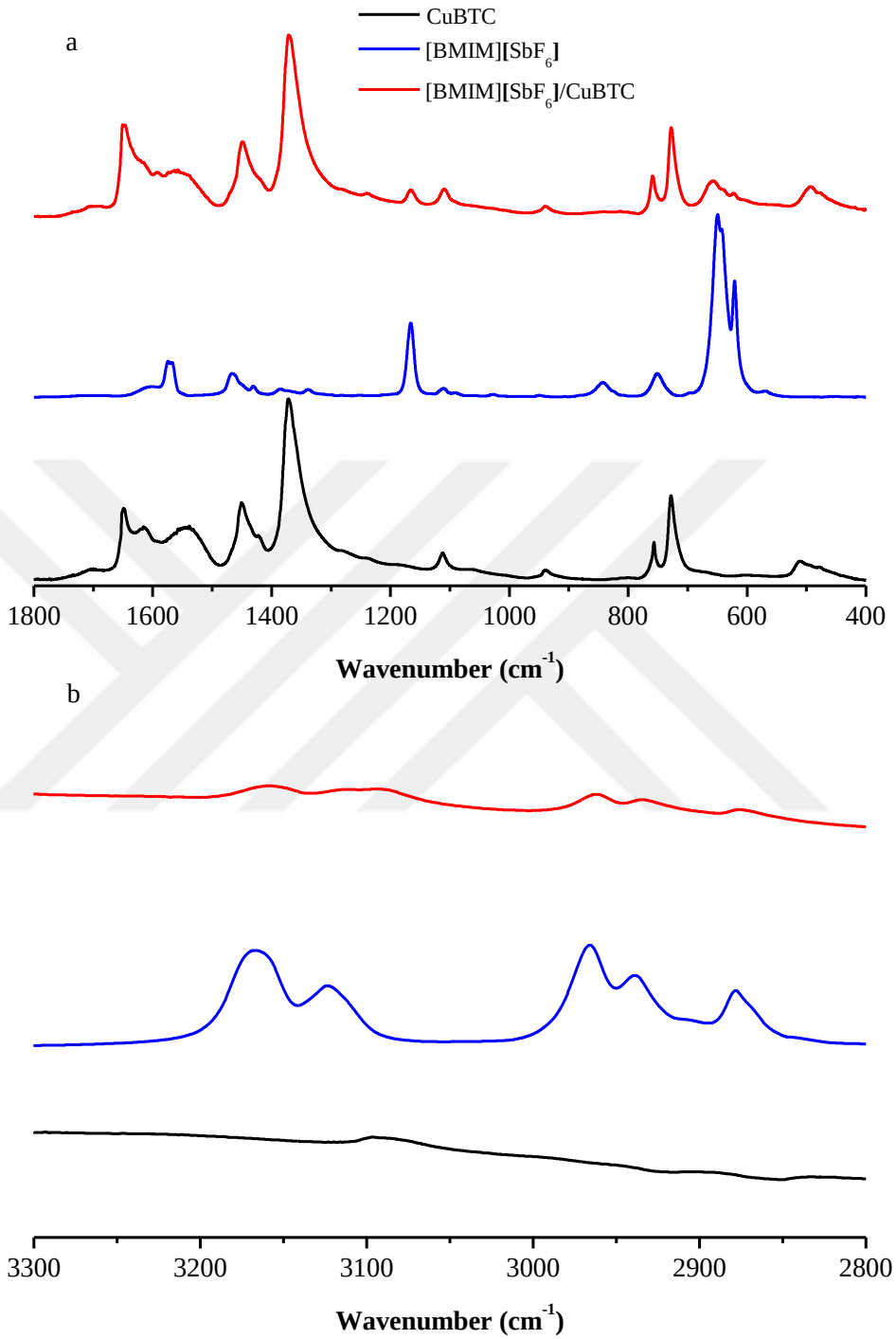

Figure A.4. FTIR spectra of [BMIM][SbF_6], CuBTC and [BMIM][SbF_6]/CuBTC in the region of (a) 400-1800 cm^{-1} and (b) 2800-3300 cm^{-1}.

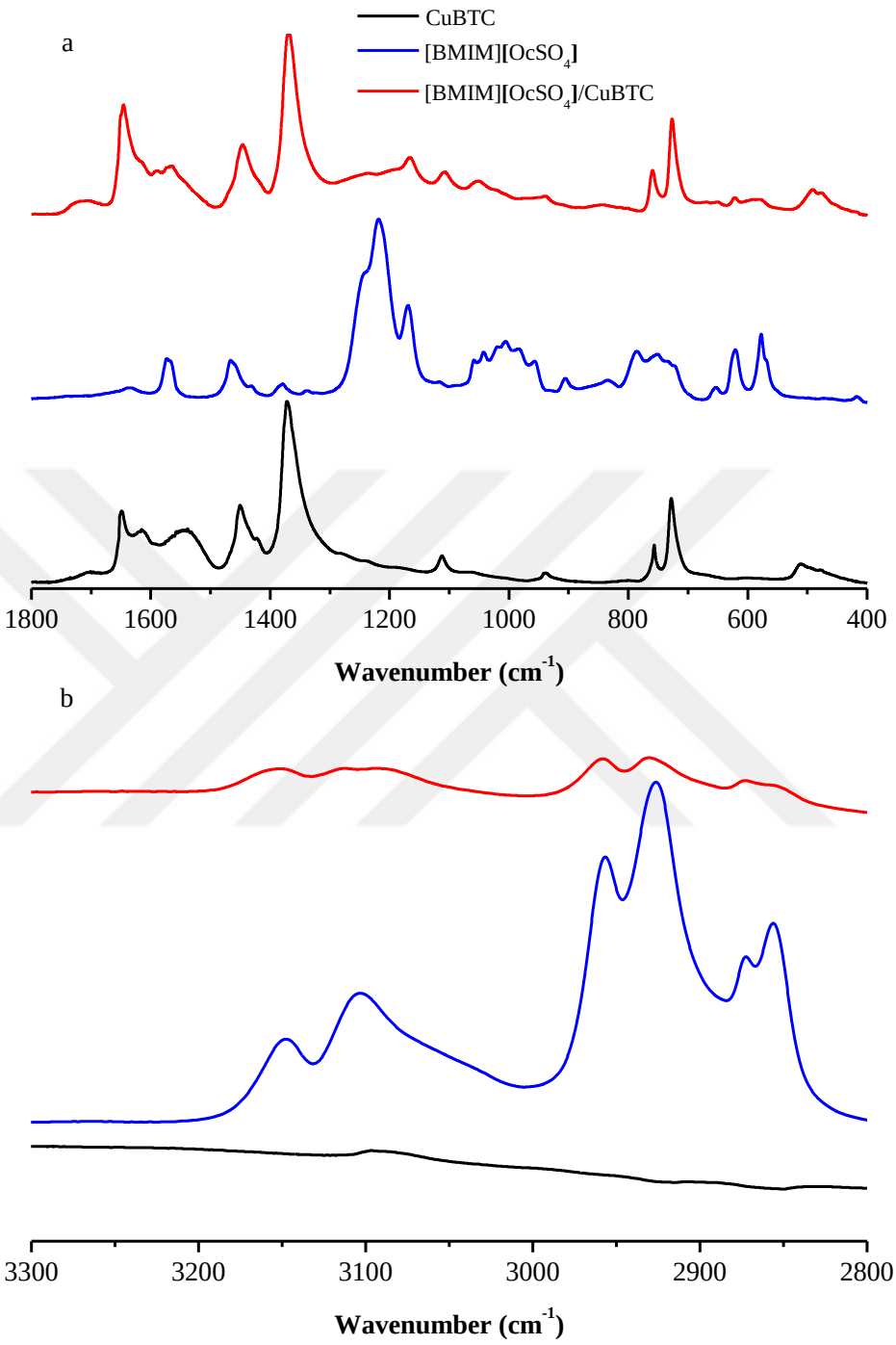

Figure A.5. FTIR spectra of [BMIM][$OcSO_4$], CuBTC and [BMIM][$OcSO_4$]/CuBTC in the region of (a) 400-1800 cm^{-1} and (b) 2800-3300 cm^{-1}

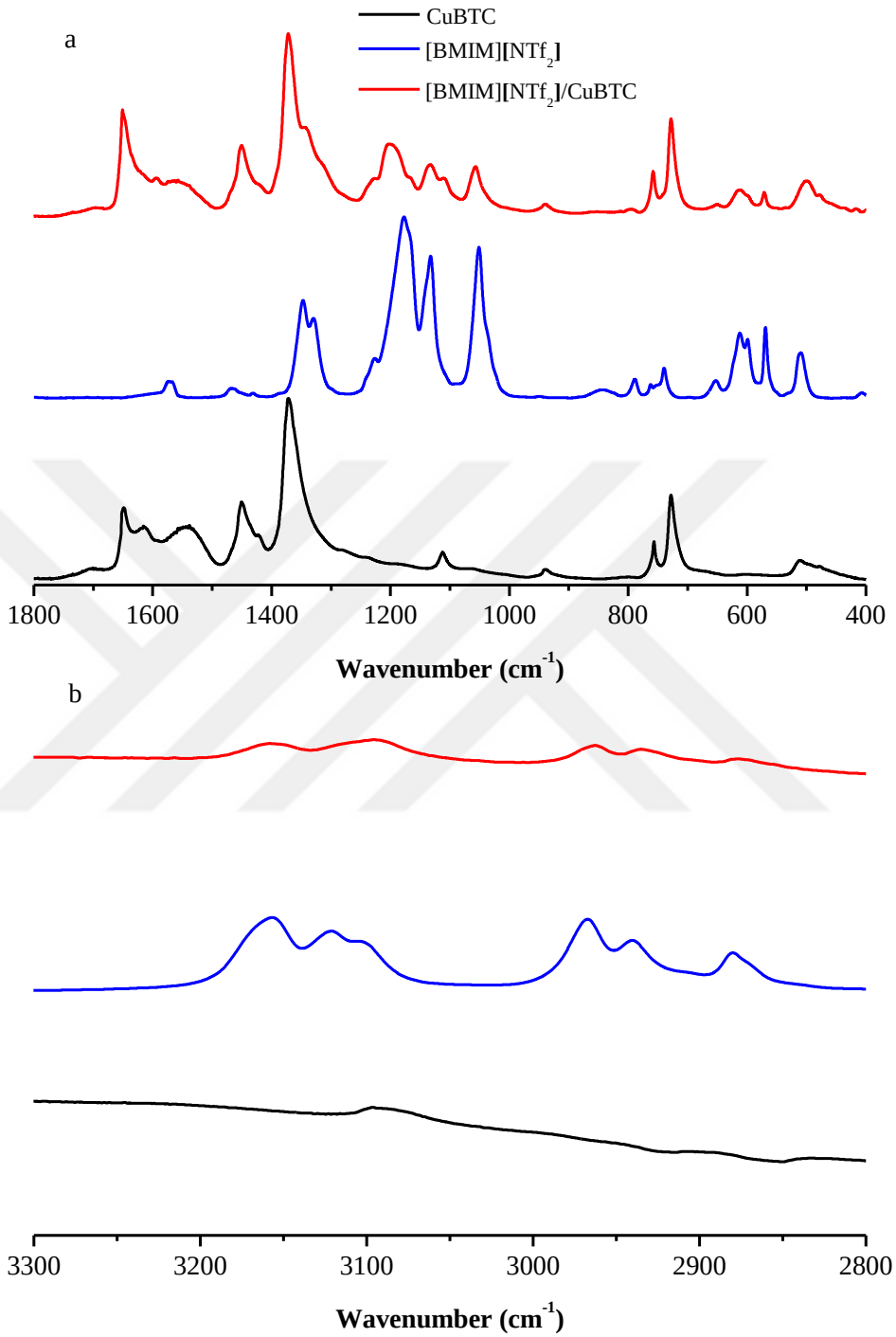

Figure A.6. FTIR spectra of [BMIM][NTf_2], CuBTC and [BMIM][NTf_2]/CuBTC in the region of (a) 400-1800 cm^{-1} and (b) 2800-3300 cm^{-1}.

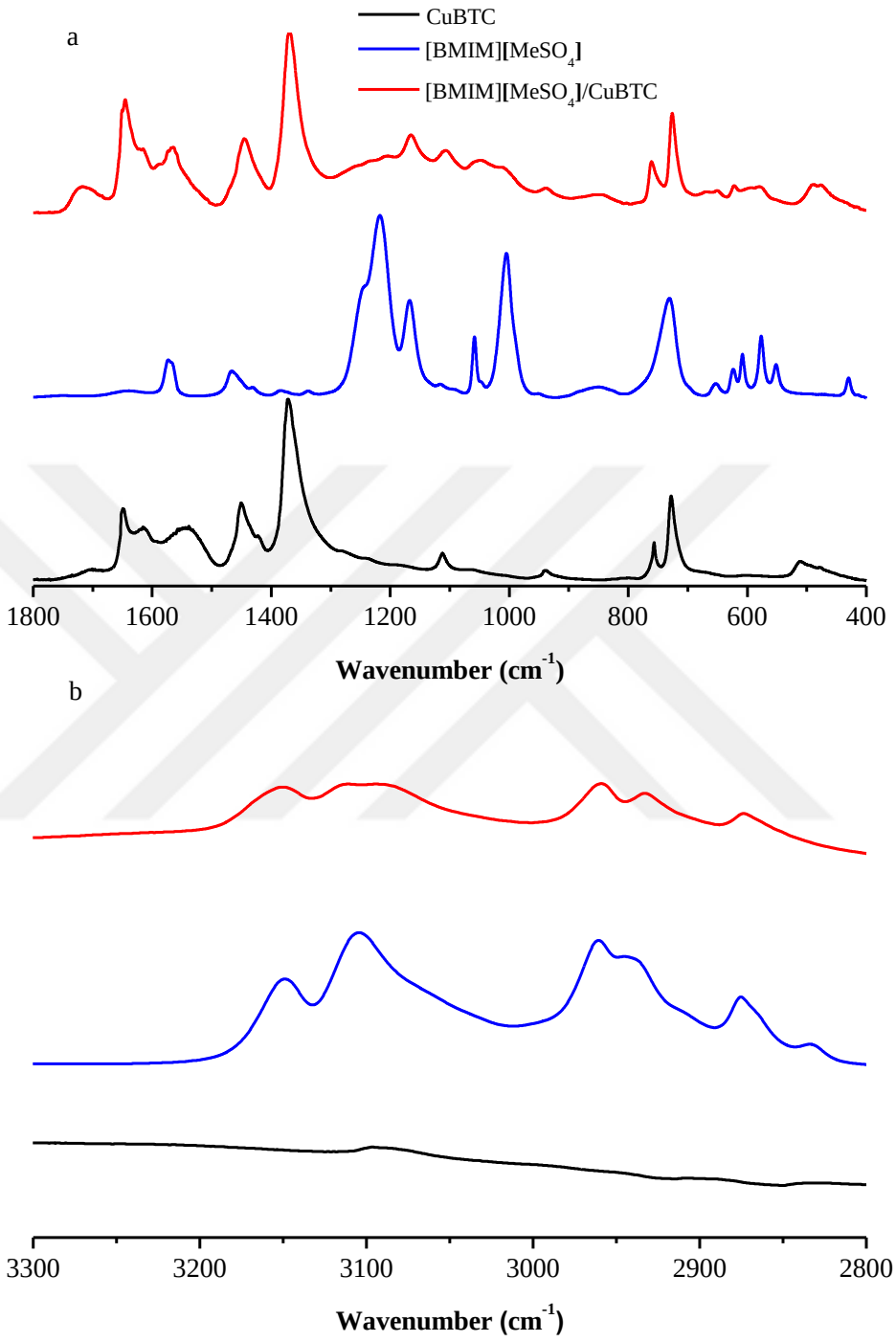

Figure A.7. FTIR spectra of [BMIM][MeSO4], CuBTC and [BMIM][MeSO4]/CuBTC in the region of (a) 400-1800 cm^{-1} and (b) 2800-3300 cm^{-1}.

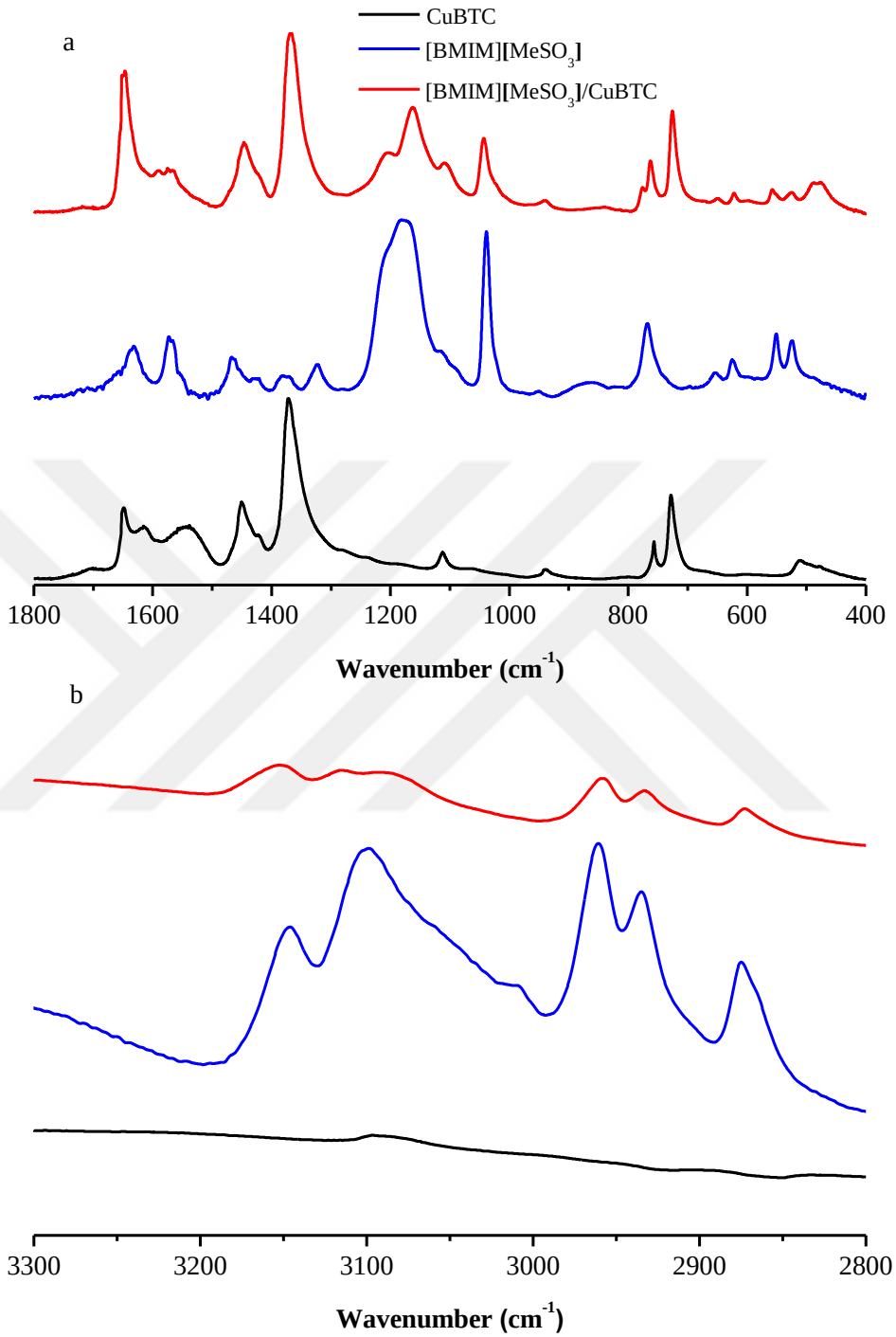

Figure A.8. FTIR spectra of [BMIM][$MeSO_3$], CuBTC and [BMIM][$MeSO_3$]/CuBTC in the region of (a) 400-1800 cm^{-1} and (b) 2800-3300 cm^{-1}.

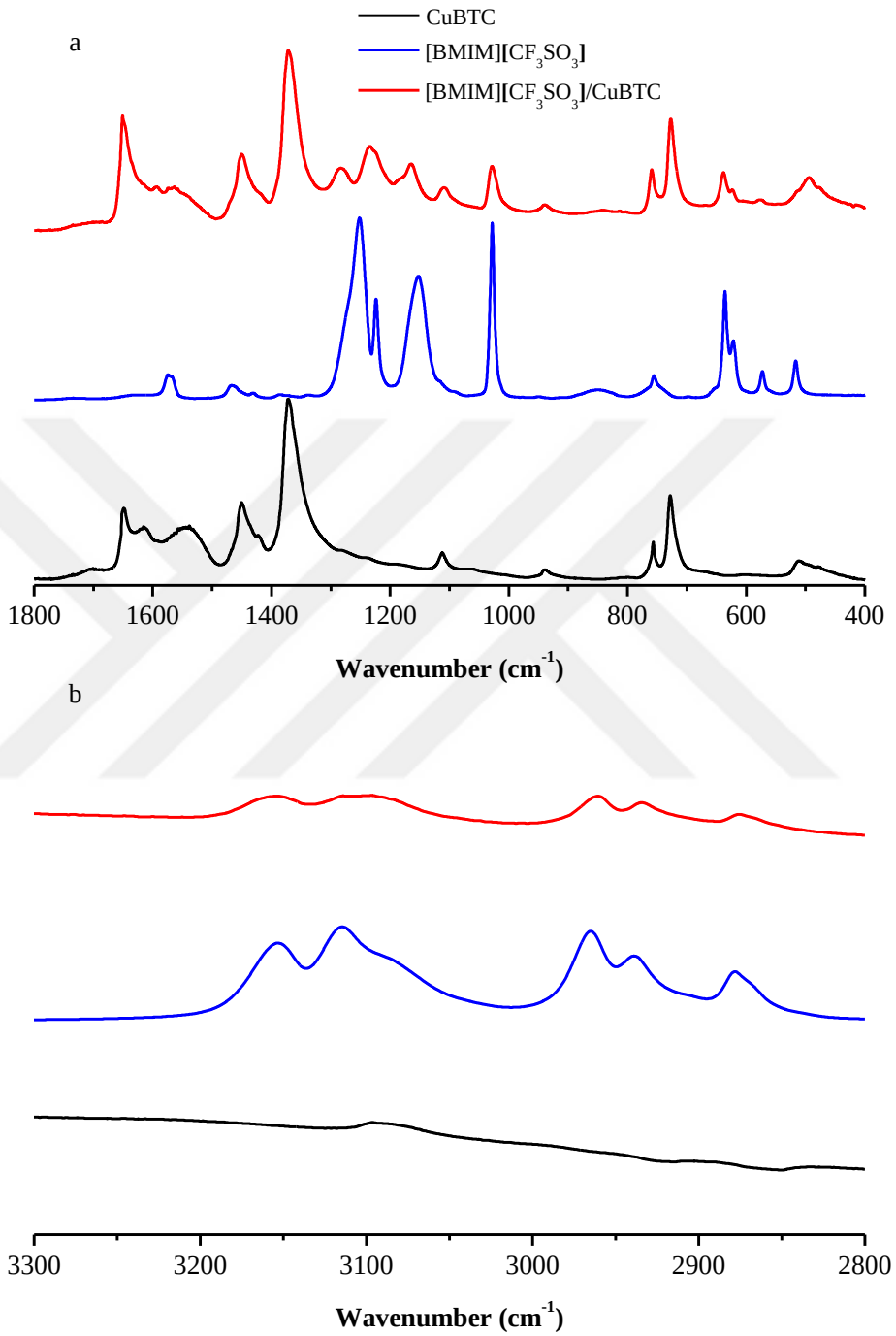

Figure A.9. FTIR spectra of [BMIM][CF_3SO_3], CuBTC and [BMIM][CF_3SO_3]/CuBTC in the region of (a) 400-1800 cm^{-1} and (b) 2800-3300 cm^{-1}.

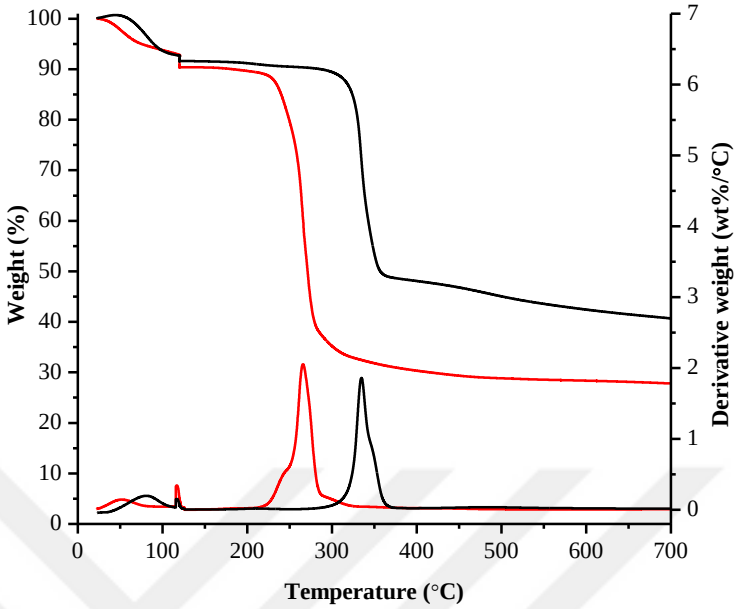

Figure A.10. TGA results of CuBTC and [BMIM][SCN]/CuBTC. Black curve: CuBTC and red curve: [BMIM][SCN]/CuBTC.

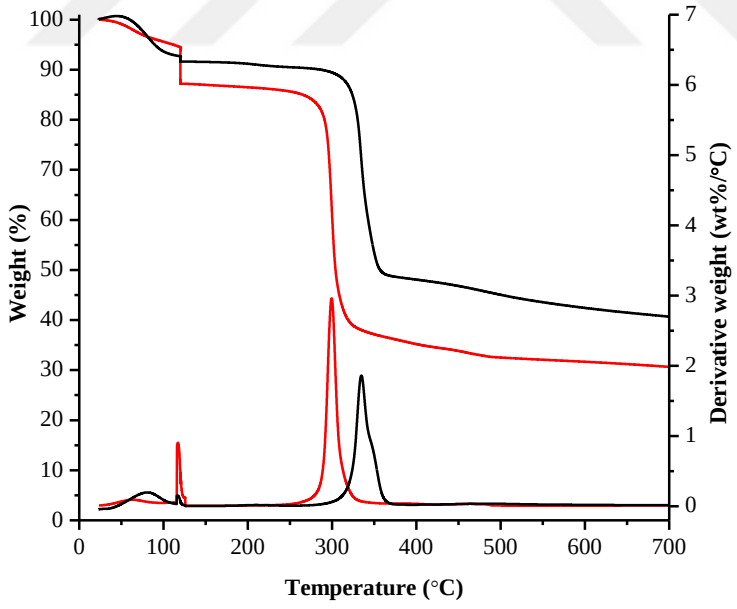

Figure A.11. TGA results of CuBTC and [BMIM][SbF_6]/CuBTC. Black curve: CuBTC and red curve: [BMIM][SbF_6]/CuBTC.

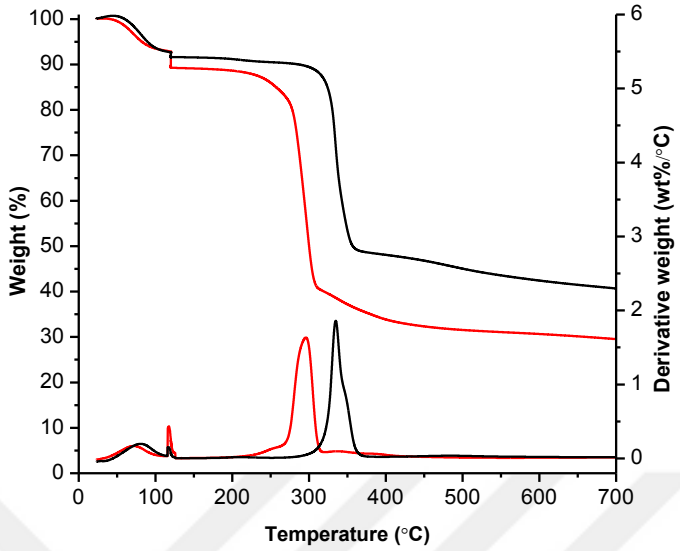

Figure A.12. TGA results of CuBTC and [BMIM][$OcSO_4$]/CuBTC. Black curve: CuBTC and red curve: [BMIM][$OcSO_4$]/CuBTC.

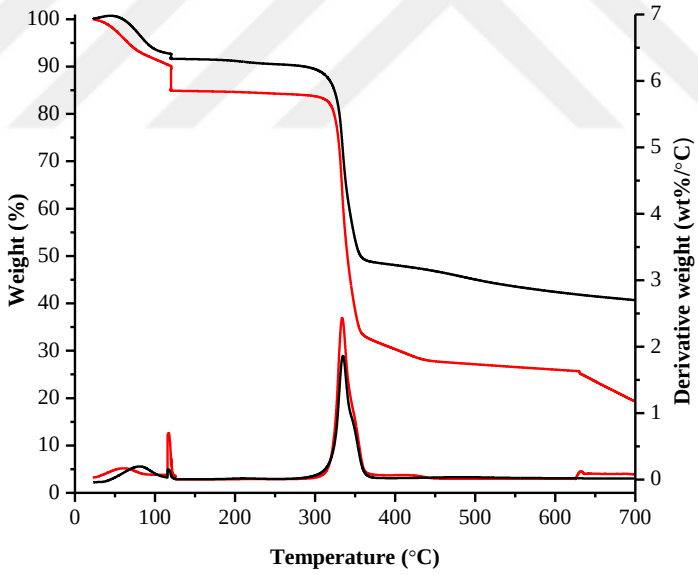

Figure A.13. TGA results of CuBTC and [BMIM][NTf_2]/CuBTC. Black curve: CuBTC and red curve: [BMIM][NTf_2]/CuBTC.

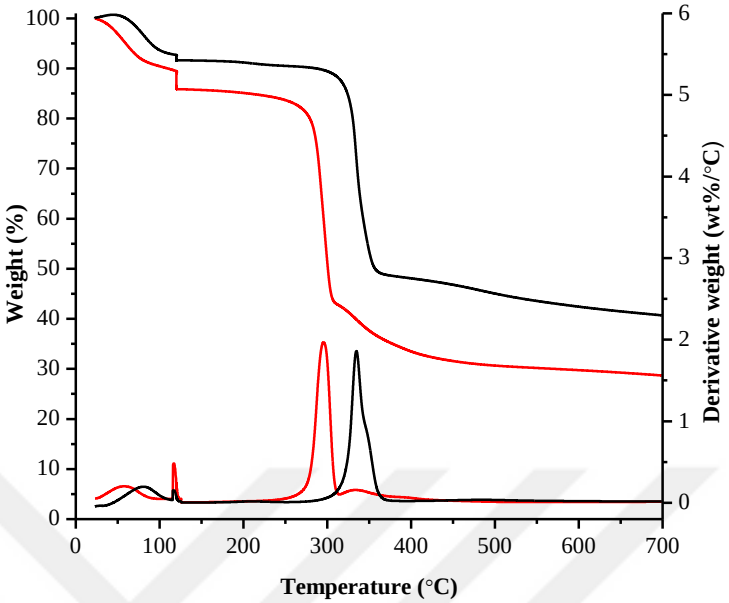

Figure A.14. TGA results of CuBTC and [BMIM][$MeSO_4$]/CuBTC. Black curve: CuBTC and red curve: [BMIM][$MeSO_4$]/CuBTC.

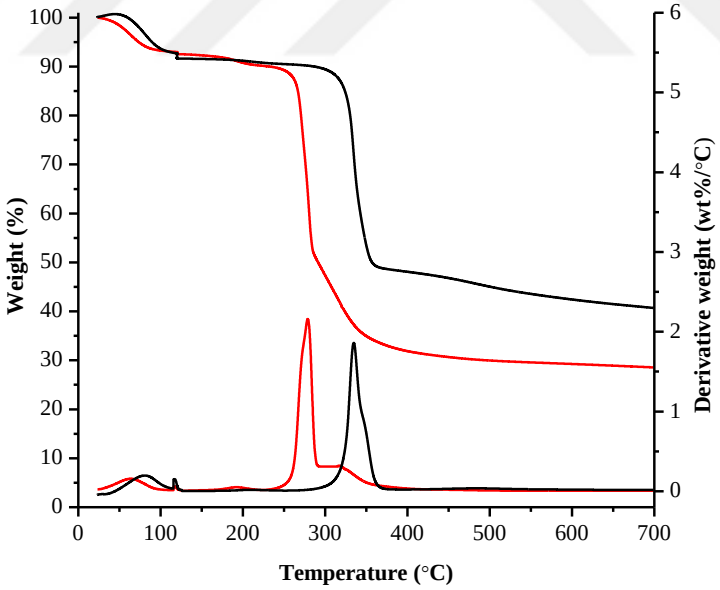

Figure A.15. TGA results of CuBTC and [BMIM][$MeSO_3$]/CuBTC. Black curve: CuBTC and red curve: [BMIM][$MeSO_3$]/CuBTC.

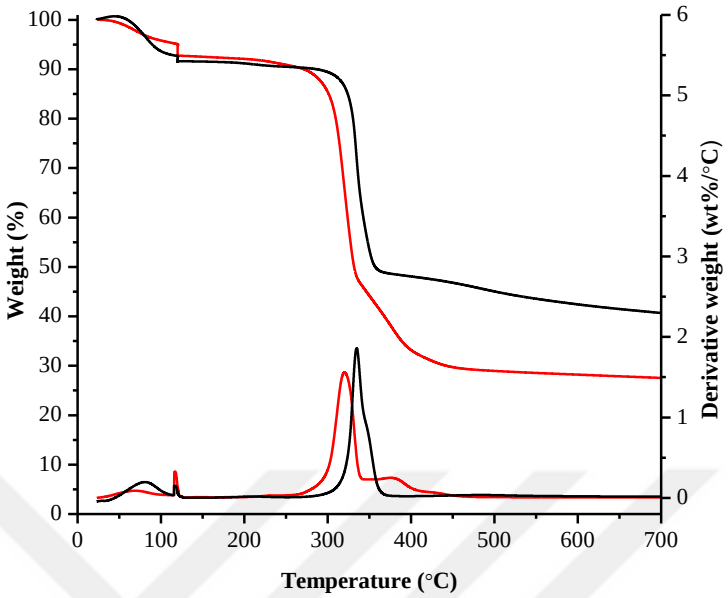

Figure A.16. TGA results of CuBTC and [BMIM][CF_3SO_3]/CuBTC. Black curve: CuBTC and red curve: [BMIM][CF_3SO_3]/CuBTC.,

Table A.1. BET surface areas, pore volumes, and corresponding IL loading in each sample (calculated from XRF measurements).

Sample	BET surface area (m^2 g^{-1})	Pore volume (cm^3 g^{-1})	XRF IL Loading (wt %)
CuBTC	1324	0.522	—
[BMIM][SbF_6]/CuBTC	601.1	0.324	24.8
[BMIM][$MeSO_4$]/CuBTC	339.7	0.154	21.5
[BMIM][CF_3SO_3]/CuBTC	356.5	0.164	26.8
[BMIM][NTf_2]/CuBTC	324.8	0.143	25.9
[BMIM][$MeSO_3$]/CuBTC	129.1	0.062	27.6
[BMIM][SCN]/CuBTC	88.6	0.075	23.8
[BMIM][$OcSO_4$]/CuBTC	150.8	0.068	23.1

Table A.2. C2−H vibration frequency of bulk ILs and corresponding (Cu−O) red shifts for each IL/MOF sample. (shift values are obtained from Fityk software).[59]

Sample	ν(C2H) vibration of IL (cm^{-1})	(Cu−O) red shift (cm^{-1})
[BMIM][SbF_6]/CuBTC	3122	4.4
[BMIM][$MeSO_4$]/CuBTC	3112	5.4
[BMIM][CF_3SO_3]/CuBTC	3117	5.3
[BMIM][NTf_2]/CuBTC	3124	3.4
[BMIM][$MeSO_3$]/CuBTC	3109	6.8
[BMIM][SCN]/CuBTC	3097	8.5
[BMIM][$OcSO_4$]/CuBTC	3107	4.6

APPENDIX B: Full Names of Ionic Liquids

Table B.1. Abbreviations and full names of ionic liquids referred in this thesis.

IL Abbreviations	IL Full Name
[BMIM][$MeSO_4$]	1-*n*-butyl-3-methylimidazolium methylsulfate
[BMIM][$MeSO_3$]	1-*n*-butyl-3-methylimidazolium methanesulfonate
[BMIM][$OcSO_4$]	1-*n*-butyl-3-methylimidazolium octylsulfate
[BMIM][SbF_6]	1-*n*-butyl-3-methylimidazolium hexafluoroantimonat
[BMIM][CF_3SO_3]	1-*n*-butyl-3-methylimidazolium trifluoromethanesulfonate
[BMIM][BF_4]	1-*n*-butyl-3-methylimidazolium tetrafluoroborate
[BMIM][Tf_2N]	1-*n*-butyl-3-methylimidazolium bis (trifluoromethylsulfonyl) imide
[BMIM][PF_6]	1-*n*-butyl-3- methylimidazolium hexafluorophosphate
[BMIM][Br]	1-*n*-butyl-3-methylimidazolium bromide
[BMIM][SCN]	1-*n*-ethyl-3-methylimidazolium thiocyanate
EMI-TFSA	1-*n*-ethyl-3-methylimidazolium bis (trifluoromethylsulfonyl) imide
[BMIM][Ac]	1-*n*-butyl-3-methylimidazolium acetate
EIMS-HTFSA	1-(1-ethyl-3-imidazolium) propane-3-sulfate N, N-bis (trifluoromethanesulfonyl)amide
ABIL-OH	amino-functionalized basic ionic liquid
[PSMIM][HSO_4]	1-methyimidazolium-3-propylsulfonate hydrosulfate
DAILs	1,4-bis[3-(propyl-3-sulfonate) imidazolium] butane hydrogen sulfate

APPENDIX C: Cosmo-RS solubility results for [BMIM][PF_6] and [BMMIM][PF_6]

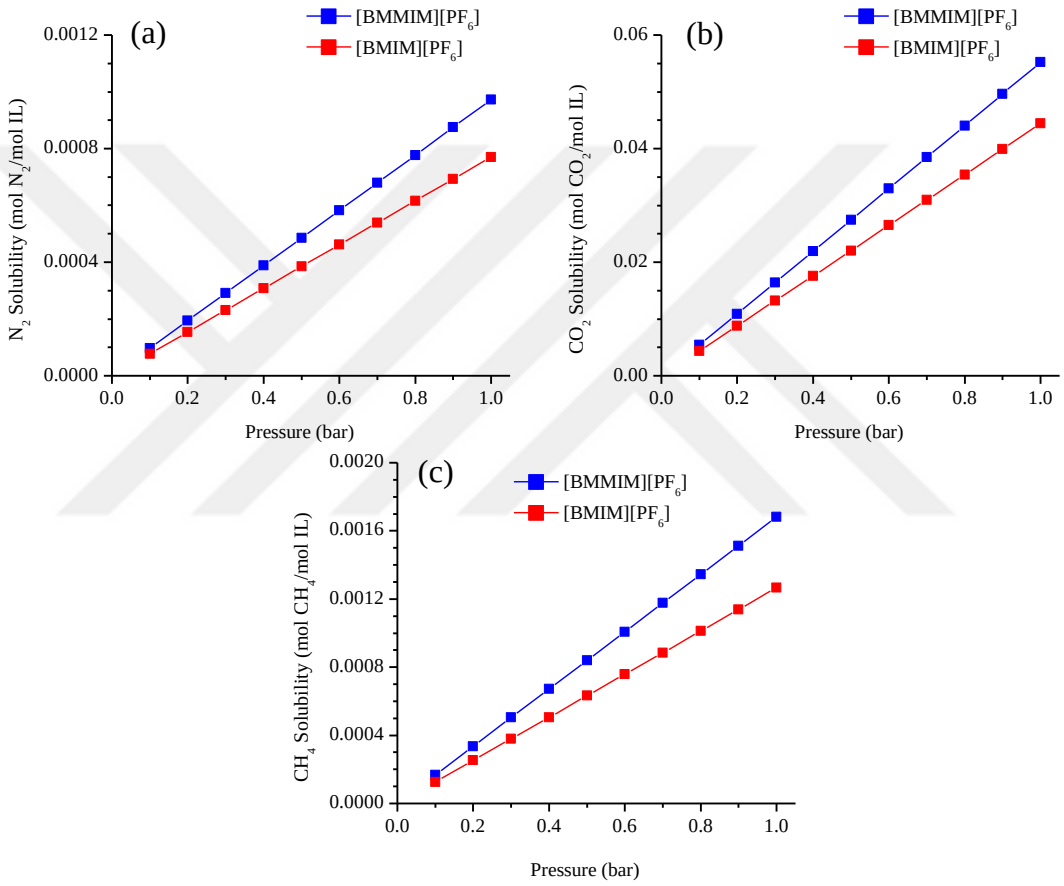

Figure C.1 Cosmo-RS solubility results for [BMIM][PF_6] and [BMMIM][PF_6] at 298 K; (a) N_2, (b) CO_2 and (c) CH_4.

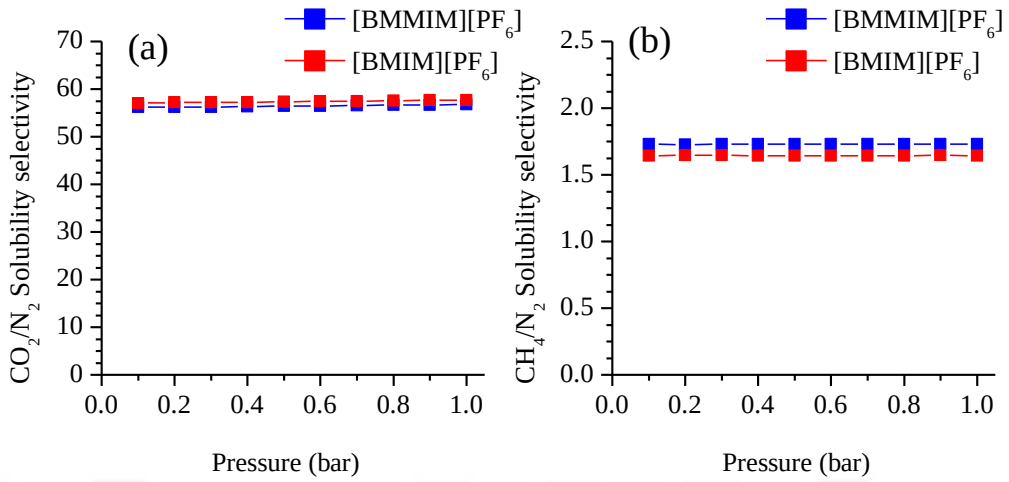

Figure C.2. Solubility selectivities for [BMIM][PF_6] and [BMMIM][PF_6] at 298 K; (a) CO_2/N_2 and (b) CH_4/N_2.

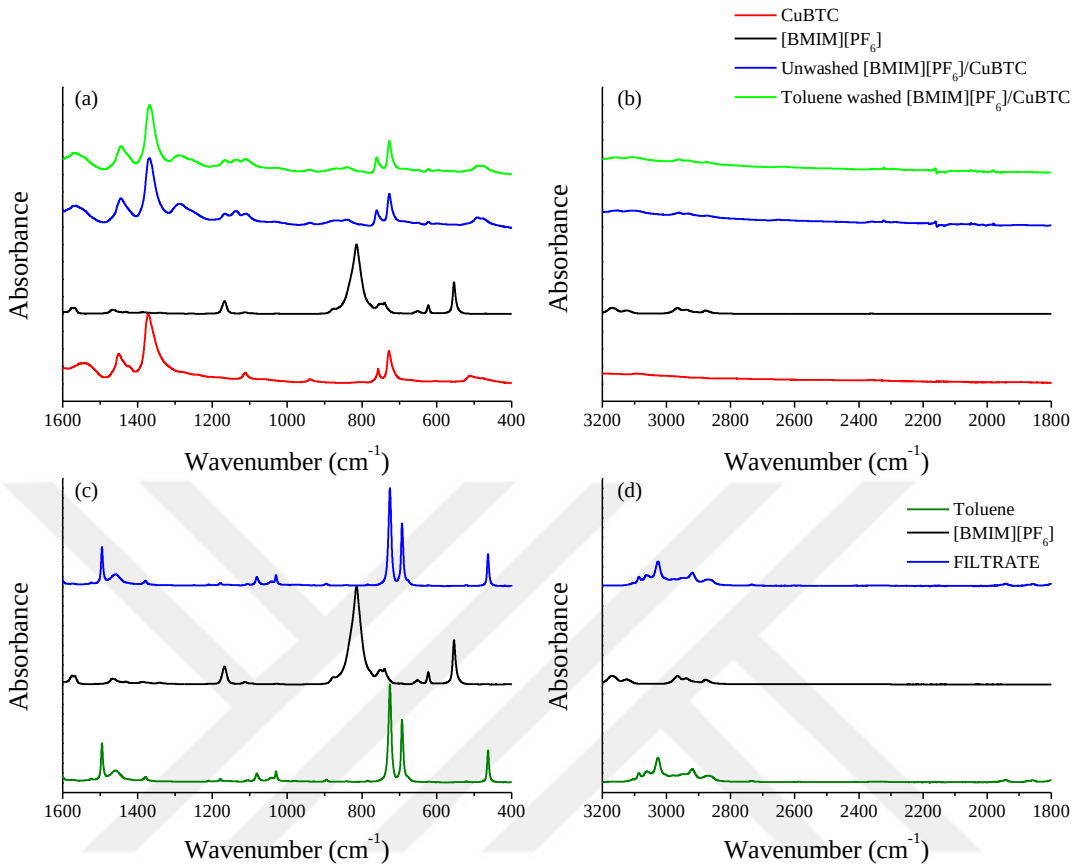

Figure C.3. FTIR spectra of CuBTC, bulk [BMIM][PF_6], and [BMIM][PF_6]/CuBTC prior and after washing with toluene in two different regions, 400-1600 cm^{-1} and 1800-3200 cm^{-1}; (a) and (b) Powder samples before and after washing with toluene; (c) and (d) The filtrate (liquid samples).

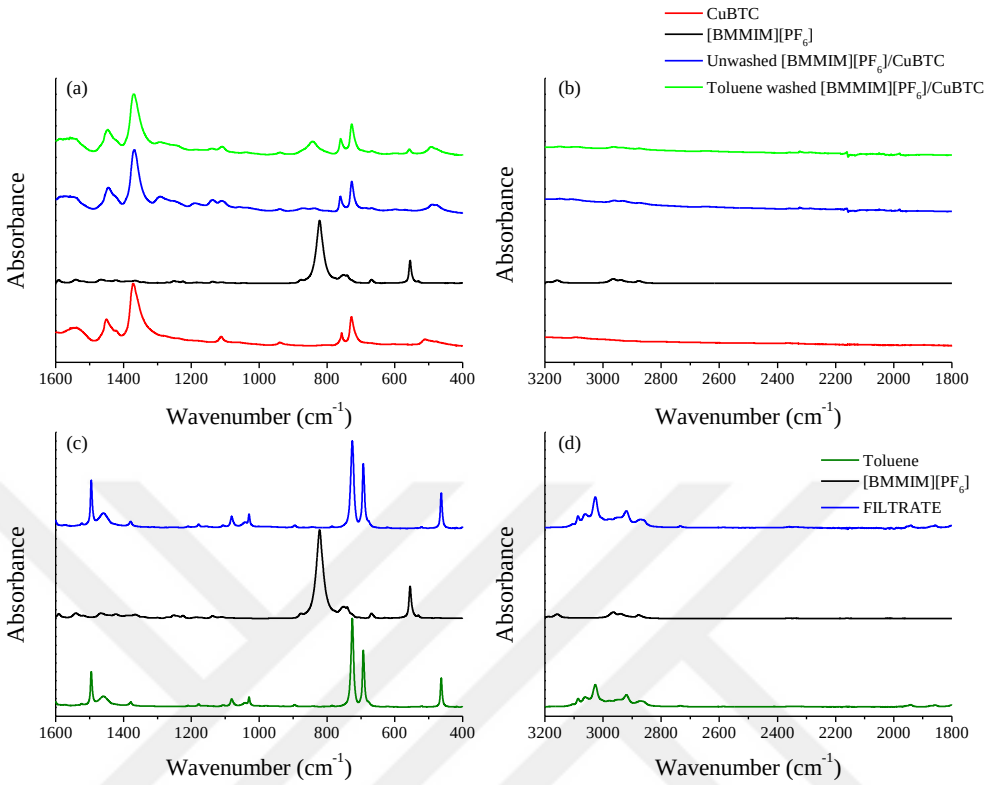

Figure C.4. FTIR spectra of CuBTC, bulk [BMIM][PF_6], and [BMIM][PF_6]/CuBTC prior and after washing with toluene in two different regions, 400-1600 cm^{-1} and 1800-3200 cm^{-1}; (a) and (b) Powder samples before and after washing with toluene; (c) and (d) The filtrate (liquid samples).